GLANDULAR TISSUE PATTERN ANALYSIS THROUGH MULTIMODAL MRI-MAMMOGRAPHY REGISTRATION

Eloy García Marcos

DOCTORAL THESIS

GLANDULAR TISSUE PATTERN ANALYSIS THROUGH MULTIMODAL MRI-MAMMOGRAPHY REGISTRATION

Eloy García Marcos

2018

DOCTORAL THESIS

GLANDULAR TISSUE PATTERN ANALYSIS THROUGH MULTIMODAL MRI-MAMMOGRAPHY REGISTRATION

Eloy García Marcos

2018

DOCTORAL PROGRAM in TECHNOLOGY

Supervised by:
Dr. Joan Martí Bonmatí
Dr. Arnau Oliver Malagelada

Work submitted to the University of Girona in partial fulfilment of the requirements for the degree of Doctor of Philosophy

List of publications

This thesis is written as a compendium of a selection of the following research articles:

Papers in international journals

Eloy García, Yago Diez, Oliver Diaz, Xavier Lladó, Robert Martí, Joan Martí, and Arnau Oliver. *A step-by-step review on patient-specific biomechanical finite element models for breast MRI to X-ray mammography registration.* Medical Physics, vol. 45, issue 1, pp. e6-e31, January 2018. **DOI:** 10.1002/MP.12673 (JCR RNMMI IF: 2.617, Q2(37/127))

Eloy García, Oliver Diaz, Robert Martí, Yago Diez, Albert Gubern-Mérida, Melcior Sentís, Joan Martí, and Arnau Oliver. *Local breast density assessment using reacquired mammographic images.* European Journal of Radiology, vol. 93, pp 121-127, August 2017. **DOI:** 10.1016/J.EJRAD.2017.05.033 (JCR RNMMI IF: 2.462, Q2(44/127))

Eloy García, Yago Diez, Oliver Diaz, Xavier Lladó, Albert Gubern-Mérida, Robert Martí, Joan Martí, and Arnau Oliver. *Multimodal breast parenchymal patterns correlation using a patient-specific biomechanical model.* IEEE Transactions on Medical Imaging, **DOI:** 10.1109/TMI.2017.2749685. (JCR RNMMI IF: 3.942, Q1(17/127))

Eloy García, Yago Diez, Oliver Diaz, Xavier Lladó, Albert Gubern-Mérida, Robert Martí, Joan Martí, and Arnau Oliver. *Breast MRI and X-ray mammography registration using gradient values.* Medical Image Analysis. Under Review.

Papers in conference proceedings

Eloy García, Arnau Oliver, Yago Diez, Oliver Diaz, Joachim Georgii, Albert Gubern-Mérida, Robert Martí, and Joan Martí. *Comparing regional breast density using full-field digital mammograms and magnetic resonance imaging: a preliminary study.* MICCAI Work-

shop on Breast Image Analysis, pp 33-40. Munich, Germany. October 2015.

Oliver Diaz, Arnau Oliver, Sergi Ganau, **Eloy García**, Joan Martí, Melcior Sentís, Robert Martí, *Feasibility of depth sensors to study breast deformation during mammography procedures*, International Workshop on Breast Imaging (IWDM), LNCS 9699, pp 446-453. Malmö, Sweden. June 2016. **DOI:** 10.1007/978-3-319-41546-8-56

Eloy García, Arnau Oliver, Yago Diez, Oliver Diaz, Albert Gubern-Mérida, Xavier Lladó, Joan Martí, *Comparison of four breast tissue segmentation algorithms for multi-modal MRI to X-ray mammography registration*, International Workshop on Breast Imaging (IWDM), LNCS 9699, pp 493-500. Malmö, Sweden. June 2016. **DOI:** 10.1007/978-3-319-41546-8-62

Oliver Diaz, **Eloy García**, Arnau Oliver, Joan Martí, Robert Martí, *Scattered radiation in DBT geometries with flexible breast compression paddles: a Monte Carlo simulation study*, SPIE Conference on Medical Imaging, Proc. SPIE 10132, pp 101324G1-101324G7. Orlando, Florida. February 2017. **DOI:** 10.1117/12.2255722

Eloy García, Arnau Oliver, Oliver Diaz, Yago Diez, Albert Gubern-Mérida, Robert Martí, Joan Martí, *Mapping 3D breast lesions from full-field digital mammograms using subject-specific finite element models*, SPIE Conference on Medical Imaging, Proc. SPIE 10135, pp 1013504O1-1013504O8. Orlando, Florida. February 2017. **DOI:** 10.1117/12.2255957

Eloy García, Arnau Oliver, Yago Diez, Oliver Diaz, Xavier Lladó, Robert Martí, and Joan Martí, *Similarity metrics for intensity-based registration using breast density maps*, Iberian Conference on Pattern Recognition and Image Analysis (IbPria), pp 217-225. Faro, Portugal. June 2017. **DOI:** 10.1007/978-3-319-58838-4-24

Acronyms

ABUS: Automatic Breast Ultrasound

BI-RADS: Breast Imaging Reporting and Data System

BV: Breast Volume

CC: Cranio-Caudal (mammographic projection)

CT: Computer Tomography

DBT: Digital Breast Tomosynthesis

DCE-MRI: Dynamic Contrast Enhancement Magnetic Resonance Imaging

DRR: Digitally Reconstructed Radiography

FDA: Food and Drug Administration (USA)

FE: Finite Element

FFDM: Full-Field Digital Mammogram

GC: Gradient Correlation

GPU: Graphics Processing Unit

ITK: The Insight Toolkit

KLD: Kullback-Leibler Divergence

MG: Mammography

MI: Mutual Information

MIP: Maximum Intensity Projection

MLO: MedioLateral Oblique (mammographic projection)

MRI: Magnetic Resonance Imaging

NCC: Normalized Cross-Correlation

RF: Radiofrequency

ROI: Region Of Interest

SSIM: Structural Similarity index

TRE: Target Registration Error

US: Ultrasound

VBD: Volumetric Breast Density

VGT: Volume of Glandular Tissue

VTK: The Visualization Toolkit

List of Figures

Contents

Abstract

Breast cancer is the most common cancer in women worldwide. Current statistics show that one in eight women will develop this disease over the course of her lifetime. Early detection increases the likelihood of overcoming the disease, motivating the implementation of screening programs. While X-ray mammography is the gold standard image modality for screening and diagnosis of breast cancer, it presents decreased sensitivity in dense breasts. Thus, other medical image modalities, such as magnetic resonance imaging (MRI) and ultrasounds, are used to overcome the limitations of the mammography. Several studies have shown that the combination of the different medical image modalities leads to a more accurate diagnosis and, therefore, a more effective medical treatment of patient diseases. However, the fusion of information among several image modalities is a challenging task, due to the differences not only in the physics underlying each modality but, also, the different patient positioning during the image acquisition. On the one hand, inner structures of the breast, such as nerves, blood vessels and ligaments, can be clearly visible in one modality but undetected in the others. On the other hand, movement restrictions, applied during the image acquisition, are completely different.

The main purpose of this thesis is to evaluate the similarity among the information provided by two medical image modalities, such as the X-ray mammography and MRI, and, at the same time, to propose new algorithms to register the images in order to correlate the position of lesion and susceptible areas. To achieve this goal, we use registration algorithms and image analysis techniques. A deep review of the state-of-the-art, focusing our attention in the multimodal registration problems using patient-specific biomechanical finite-element (FE) models, is performed, from the biomechanical model construction (including the preprocessing and segmentation of MRI images, a suitable FE mesh construction as well as the methodology to quantify the accuracy and quality of the methods) to the physics underlying the mechanical deformation (elastic and hyperelastic parameters exposed in the literature, and loading forces and boundary condition) to solve the problem. Similarly, the registration algorithm and technical and medical aspects to validate the registration are exposed with the aim to bridge the gap between the engineering and the clinical performance. Finally, we include a brief state-of-the-art of software options as well as the requirements and advantages of each tool, in order to obtain a suitable simulation and an accurate solution of the problem.

Our analysis begins evaluating the similarity of the glandular tissue between two mammograms from the same patient, acquired in the same day and in a short time frame. This fact allows us to evaluate the effect of the breast compression in the parenchymal pattern

distribution. We use the commercial software Volpara^{TM} in order to extract the glandular tissue distribution directly from full-field digital mammograms (FFDM). Afterwards, we analyze the breast volume, volume of glandular tissue and breast density values provided by the software. Regarding the density maps -i.e. the image of the glandular tissue distribution- we evaluate the information as well as the structural similarity by means of the image registration algorithms. Our results show that the information provided by Volpara^{TM} is stable, independently of several acquisition factors, such as the X-ray energy spectrum or small variations in the angle of projection. However, changes in the compression -i.e. breast thickness- clearly affect the glandular tissue distribution in the image.

The monomodal analysis provides us a baseline result to perform the multimodal comparison between MRI and mammography. To achieve this goal, a fully automatic framework to register Volpara^{TM} Density Maps and MRI images was developed. This software uses a patient-specific biomechanical model of the breast, which mimics the mammographic compression performed during the mammographic acquisition. In this work, we propose a new methodology to project the glandular tissue directly from the MRI, avoiding the loss of information that can be yielded when the image is deformed.

The evaluation of the similarity, between the real and synthetic density maps, also requires to propose a new methodology, which takes into consideration the multimodal nature of the problem. Measures and techniques from other fields such as information theory, visual perception and statistics are used in our work. Our analysis shows a high similarity between the information contained in the two modalities as well as a high structural similarity in the distribution of the glandular tissue. A visual analysis, using a checkerboard pattern, shows continuity in the longest structures of the glandular tissue. However, an aliasing effect is yielded when the glandular tissue is projected from the MRI

During the registration framework evaluation we computed the target registration error (TRE) between landmarks -i.e. lesions- in both MRI and mammography. The 2D problem consists of directly projecting the landmark position from the MRI to the mammogram, computing the Euclidean distance between the computed and the real landmark position. However, locating the 3D position, within the MRI from the corresponding lesions in the mammograms, used to require complex and computational expensive methods to undo the breast compression. To solve this issue, we propose a new, fast and efficient algorithm to locate the landmark position within the MRI. Locating several rays from different mammographic projections (mainly, cranio caudal (CC) and mediolateral oblique (MLO)), the 3D landmark position can be computed as the intersection (or the center of mass of the two closest points) among the rays.

Using a similar methodology to that proposed during the glandular tissue projection, a back-projection ray-tracing can be performed, allowing to locate the ray path in the uncompressed biomechanical model, avoiding to undo the breast compression. To accelerate the computation of the intersection between two rays, we propose an easy algorithm which sub-divide the rays, reducing the search space. Our model reduces the search space until 600 times with respect to a traditional point-by-point search. Thus, the computational time to locate the intersection is about 8 ms, allowing real-time applications in the clinical practice. Furthermore, the TRE, in average, are about 1 cm, better than those exposed in previous works.

To conclude, we evaluate the capability of using other information, not only the glandular tissue (i.e. intensity), to perform the registration between the images. We focus our attention in the glandular tissue gradient. While the optimization algorithm (biomechanical model extraction and parameter optimization) is similar to our previous work, in this case the glandular tissue gradient is extracted from the mammograms and MRI images by

means of image processing techniques. The MRI gradient is projected to the mammogram using two different approaches. The first one uses the accumulated directional derivative, obtaining a scalar value which is comparable to the norm of the gradients obtained from the mammograms. The second one accumulates the gradient considering each direction independently, yielding a vector which is comparable to the directional derivative obtained from the mammograms by means of a gradient correlation metric. In order to provide a fair comparison, we compare the results obtained using our methodology with a traditional intensity-based registration approach where we transform the MRI in a pseudo-Computer Tomography (pseudo-CT) image by means of a polyenergetic model instead of a traditional monoenergetic approach.

Our results show an improvement in the TRE using scalar gradient values, with respect to the traditional intensity-based approach. Furthermore, we evaluate the different behavior using isotropic and anisotropic material models of the breast and we look for the correlation between the TRE and several factor of interest such as the breast glandularity and the inner landmark position. Anisotropic models shows an improvement with respect to the isotropic models, while the glandularity and the inner landmark position show a moderate correlation with respect to the TRE. Moreover, the computational time during the registration was reduced to half the time regarding our previous works.

In summary, this thesis will help radiologists and physicists to better understand the variations of the glandular tissue that can be clearly visible in one modality but not in the other. Furthermore, the evaluation of the information can guide researchers to obtain more accurate segmentation algorithms, considering the partial volume effect presented in the MRI, as well as to improve the multimodal image registration between the two modalities, not only by means of intensity-based methods but also considering additional information such as gradients. Finally, our methodology includes several proposals to develop real time applications or with acceptable time values in the clinical practice.

Resumen

El cancer de mama es el tipo de cancer más común entre las mujeres de todo el mundo. Las estadísticas muestran que una de cada ocho mujeres desarrollará esta enfermedad a lo largo de su vida. La detección precoz incrementa las posibilidades de superar dicha enfermedad, motivando la implementación de programas de cribado. La mamografía es la principal modalidad de imagen utilizada en el cribado y diagnóstico de cancer de mama, aunque en pechos densos muestra una sensitividad decreciente en la detección de enfermedades. Así, otras modalidades de imagen médica, tales como la resonancia magnética y los ultrasonidos, son utilizadas para superar las limitaciones de la mamografía de rayos X. Diversos estudios han demostrado que la combinación de las múltiples modalidades de imagen médica conlleva un diagnóstico más preciso y, por lo tanto, un tratamiento más efectivo en la enfermedad del paciente. Sin embargo, la fusión de la infomación entre las diversas modalidades sigue siendo un reto debido a las diferencias tanto en la física subyacente a cada modalidad, así como a la diferente posición del paciente durante la adquisition de la imagen. Por un lado, estructuras internas del pecho, tal y como nervios, vasos sanguíneos y ligamentos, pueden ser visibles en una modalidad pero no apreciables en las otras. Por otro lado, las restricciones del movimiento del paciente durante la adquisición de las imágenes son completamente distintas.

El objetivo principal de esta tesis es evaluar la similitud de la información entre dos de las modalidades de imagen médica expuestas anteriormente, como son la mamografía de rayos X y la resonancia magnética (MRI), y, a su vez, proponer nuevos algoritmos de registro que sirvan para correlacionar la posición espacial de lesiones entre ellas. Para llevarlo a cabo, utilizamos técnicas de registro y análisis de imagen. Un análisis detallado del estado del arte de los métodos de registro propuestos, centrándonos en aquellas técnicas basadas en modelos biomecánicos paciente-específico de elementos finitos, es llevado a cabo, partiendo de la construcción del modelo biomecánico (incluyendo el tratamiento y la segmentación de las imágenes de resonancia magnética, la construcción de una malla de elementos finitos adecuada así como los métodos para cuantificar la precisión y calidad de los métodos) hasta la física subyacente a la deformación mecánica (los parámetros elásticos e hiperelásticos del pecho, expuestos en la literatura, y las cargas, fuerzas y condiciones de contorno) para resolver el problema mecánico. Igualmente, los métodos de registro y aspectos técnicos y médicos para validar el registro son expuestos con la intención de llenar el espacio entre ingeniería y la práctica clínica. Finalmente, incluímos un breve estado del arte del software necesario así como requerimientos y ventajas de cada herramienta, con el fin de obtener una simulación adecuada y una solución precisa del problema.

Nuestro análisis comienza evaluando la similaridad del tejido glandular mamario entre mamografías de una paciente adquiridas el mismo día pero con un breve intervalo de tiempo. Esto nos permite evaluar qué efecto tiene la compresión del pecho sobre el patrón parenquimal primario. Utilizamos el software comercial Volpara^{TM} con el fin de extraer la distribución del tejido glandular directamente de las mamografías digitales. Después, analizamos los valores del volumen del pecho, volumen de tejido glanduar y densidad mamaria que nos proporciona el software. Con respecto a los mapas de densidad -imagen de la distribución del tejido glandular en la mamografía-, evaluamos la información así como la similitud espacial mediante el registro de las imágenes. Nuestros resultados muestran que la información dada por dicho software es estable, independientemente de ciertos factores en la acquisición, como son el espectro energético de los rayos X o pequeñas variaciones en el ángulo de proyección. Sin embargo las variaciones en la compresión del pecho afectan claramente a la distribución del tejido glandular en la imagen.

El análisis monomodal previamente descrito, nos sirve de base para a un análisis multimodal entre la imagen de resonancia magnética y la mamografía. Para ello, se desarrolló un *framework* completamente automático que registra los mapas de densidad de Volpara^{TM} con las imágenes de resonancia magnética. Dicho software utiliza un modelo biomecánico paciente-específico del pecho que es utilizado para simular la compresión producida durante la mamografía. Durante este trabajo se propone una nueva metodología para proyectar el tejido denso directamente desde la MRI, evitando la pérdida de información que se puede producir al deformar la imagen.

La evaluación de la similitud entre el mapa de densidad de Volpara^{TM} y la imagen sintética generada por nuestro framework también requirió la propuesta de una metodología que considerara la naturaleza multimodal del problema. Técnicas y estadísticas provenientes de otros campos de estudios como la teoría de la información, el campo de la percepción visual o la estadística son planteadas en nuestro trabajo con el fin de evaluar la similitud de la cantidad y distribución del tejido denso entre las imágenes real y sintética. Nuestro estudio demuestra una gran similitud entre la información contenida en la mamografía y la MRI así como en la distribución espacial del tejido glandular de ambas modalidades. Un análisis visual de las imágenes, utilizando un *checkerboard*, aprecia continuidad en las estructuras del tejido denso, con la particularidad de que se produce un efecto de *aliasing* al proyectar el tejido de la MRI.

Durante la evaluación del framework de registro se evaluó el error de localización (TRE) entre landmarks -i.e. lesiones- correspondientes, localizadas en la mamografía y en la MRI, producida por el registro. El problema en 2D consiste en proyectar directamente la posición de dicha lesión sobre la mamografía y calcular su distancia Euclídea con respecto al landmark original. Sin embargo, para localizar la posición en 3D, dentro de la MRI del pecho, desde las posiciones correspondientes en las mamografías, requería de metodos complejos y costosos para deshacer la compresión del modelo biomecánico. Este hecho, nos llevó a proponer una nueva metodología rápida y eficiente para localizar la posición de una lesión en la MRI a partir de las posición previamente localizada en las mamografías. Al localizar multiples rayos provenientes de distintas proyecciones del pecho (cranio caudal (CC) y mediolateral oblicua (MLO), principalmente) la posición 3D del landmark puede calcularse como la intersección (o el centro de masas de los puntos más cercanos) entre los rayos.

Utilizando una metodología similar a la propuesta para proyectar el tejido denso desde la MRI, se puede realizar un *back-projection* directamente desde las mamografía que permite localizar la trayectoria del rayo en nuestro modelo original, evitando simular la descompresion del pecho. Para acelerar el proceso de localizar el punto de intersección, proponemos un sencillo algoritmo que subdivide los rayos, reduciento el espacio de búsqueda. Nuestro modelo reduce este espacio de búsqueda hasta seiscientas veces, con respecto a una búsqueda

tradicional punto por punto. Gracias a esto, el tiempo empleado en calcular la intersección ronda los 8 ms pudiendo ser aplicable en la práctica clínica como una aplicación en *real time*. Además, los errores de registro medido son cercanos a 1 cm, mejores que los anteriormente propuestos.

Para finalizar la tesis, evaluamos la posibilidad de utilizar otra información, a parte de la cantidad del tejido denso, para realizar el registro entre las imágenes. De este modo, centramos nuestra atención en el gradiente del tejido denso. Mientras que la metodología (extracción del modelo biomecánico y optimización de los parámetros) es similar a los trabajos realizados anteriormente, en este caso, el gradiente del tejido denso de las imágenes de resonancia magnética y la mamografía se extrae mediante técnicas de procesamiento de imágenes. El gradiente de MRI es proyectado hacia la mamografía mediante dos técnicas. La primera utiliza la acumulación de la derivada direccional obteniendo una valor escalar, comparable con el módulo de los gradientes obtenidos de la mamografía. La segunda acumula el gradiente considerando cada dirección independientemente, produciendo un vector que puede ser comparado con las derivadas direccionales obtenidas de la mamografía mediante una métrica de correlación de gradiente. Para proveer de una comparativa justa con los métodos propuestos en el estado del arte, se realiza un tradicional registro basado en intensidades donde utilizamos un modelo polienergético, en lugar de los modelos monoenergéticos previamente propuestos, convirtiendo la MRI en una imagen pseudo-CT.

Nuestros resultados muestran una mejora en el registro utilizando los valores escalares del gradiente, con respecto al tradicional método basado en intensidades. Además se evaluó el diferente comportamiento utilizando materiales isotrópicos y anisotrópicos para el modelo biomécanico y se buscó correlaciones con diversos factores de interés como la glandularidad del pecho y la posición internal de la lesión. Los modelos anisotrópicos mostraron una mejora con respecto los modelos isotrópicos mientras que la glandularidad y la posición interna de las landmarks mostraron una correlación media con respecto al error del registro. Por otra parte, el tiempo de registro consiguió reducirse a la mitad en relación a los registros anteriormente realizados.

Esta tesis ayudará a radiologos y médicos a comprender las pequeñas variaciones del tejido glandular que pueden ser claramente visibles en una modalidad pero no en la otra. Además, la evaluación de la información puede orientar a los investigadores hacia segmentaciones más precisas que tengan en cuenta el efecto parcial en los voxeles de MRI, así como la mejora del registro entre las dos modalidades de imagen, no sólo por métodos basados en intensidades sino considerando información adicional como el gradiente. Por último, nuestros métodos incluyen propuestas para desarrollar aplicaciones en *real time* o con valores de tiempo aceptables en la práctica clínica.

Resum

El càncer de mama és el tipus de càncer més comú entre les dones de tot el món. Les estadístiques mostren que una de cada vuit dones desenvoluparà aquesta malaltia al llarg de la seva vida. La detecció precoç incrementa les possibilitats de superar aquesta malaltia, motivant la implementació del programes de cribratge. Tot i que la mamografia és la principal modalitat d'imatge utilitzada en el cribratge i el diagnòstic de càncer de mama, els seus resultats en pits densos mostren una sensitivitat decreixent en la detecció de malalties. Així, altres modalitats d'imatge mèdica, tal com la ressonància magnètica (MRI) i els ultrasons, són utilitzades per millorar les prestacions de la mamografia de raigs X. Diversos estudis han demostrat que la combinació de diferents modalitats d'imatge mèdica comporta un diagnòstic més precís i, per tant, un tractament més efectiu de la malaltia del pacient. No obstant això, i degut a les diferències tant en la fisica subjacent a cada modalitat com en la diferent posició del pacient durant l'adquisició, la fusió de la infomació entre les diverses modalitats segueix sent un repte. D'una banda, estructures internes del pit, tal com els nervis, vasos sanguinis i lligaments, poden ser visibles a una modalitat però no apreciables en les altres. D'altra banda, les restriccions del moviment del pacient durant l'adquisició de les imatges són completament diferents.

L'objectiu principal d'aquesta tesi és avaluar la similitud de la informació entre dues de les modalitats d'imatge mèdica exposades anteriorment, la mamografia de raigs X i la ressonància magnètica, i, al seu torn, proposar nous algoritmes de registre que serveixin per a correlacionar la posició espacial de lesions en les dues modalitats d'imatge. Per fer-ho, fem servir tècniques de registre i anàlisi d'imatge. La tesi comena amb l'exploració detallada de l'estat de l'art dels mètodes de registre proposats, centrant-nos en aquelles tècniques basades en models biomecànics pacient-específic d'elements finits, abarcant des de la construcció del model biomecànic (incloent el tractament i la segmentació de les imatges de ressonància magnètica, la construcció d'una malla d'elements finits adequada, així com els métodes per quantificar la precisició i qualitat dels resultats obtinguts) fins a la física subjacent a la deformació mecànica (els paràmetres elàstics i hiperelàstics del pit, exposats en la literatura, i les càrregues, forces i condicions de contorn) per resoldre el problema mecànic. Igualment, els mètodes de registre i aspectes tècnics i mèdics per validar el registre són exposats amb la intenció d'aproximar les tècquines d'enginyería amb la pràctica clínica. Finalment, s'incloem també un breu estat de l'art del *software* necessari així com els requeriments i avantatges de cada eina, amb el fin d'obtenir una simulació adequada i una solució precisa del problema.

El nostre anàlisi continua avaluant la similitud del teixit glandular mamari entre dues

mamografies d'una pacient adquirides en un breu interval de temps. Aquest fet ens permet avaluar quin efecte té la compressió del pit sobre el patró parenquimal primari. Utilitzem el *software* comercial Volpara^{TM} per tal d'extreure la distribució del teixit glandular directament de les mamografies digitals. Després, s'analitzen els valors del volum del pit, volum de teixit glanduar i densitat mamària que ens proporciona el programari. Pel que fa als mapes de densitat -imatge de la distribució del teixit glandular a la mamografia-, avaluem la informació així com la similitud espacial mitjançant el registre de les imatges. Els nostres resultats mostren que la informació donada per aquest *software* és estable, independentment de certs factors en l'adquisició, com són l'espectre energètic dels raigs X o petites variacions en l'angle de projecciò. No obstant això, les variacions en la compressió del pit afecten clarament a la distribució del teixit glandular en la imatge.

Aquest anàlisi monomodal, ens serveix de base per a l'anàlisi multimodal entre la imatge de ressonància magntica (MRI) i la mamografia. Per això, s'ha desenvolupat un *framework* completament automàtic que registra els mapes de densitat de Volpara^{TM} amb les imatges de ressonància magnètica. Aquest *framework* utilitza un model biomecànic pacient-específic del pit que és utilitzat per a simular la compressió produïda durant la mamografia. Durant aquest treball es proposa una nova metodologia per projectar el teixit dens directament des de la MRI, evitant la pèrdua d'informació que es pot produir al deformar la imatge. L'avaluació de la similitud entre el mapa de densitat de Volpara^{TM} i la imatge sintètica generada pel nostre framework també ha requerit de la proposta d'una metodologia que considerés la naturalesa multimodal del problema. Tècniques i estadístics provinents d'altres camps d'estudi com la teoria de la informació, el camp de la percepció visual o l'estadística són plantejades en el nostre treball per tal d'avaluar la similitud de la quantitat i la distribució del teixit dens entre les imatges real i sintètica. El nostre estudi demostra una gran similitud entre la informació continguda en la mamografia i la MRI així com en la distribució espacial del teixit glandular de les dues modalitats. L'anàlisi visual de les imatges, utilitzant un patró *checkerboard*, aprecia continuïtat en les estructures del teixit dens, amb la particularitat que es produeix un efecte d'aliasing en projectar el teixit de la MRI.

Durant l'avaluació del framework de registre es va avaluar l'error degut al registre de la localització entre landmarks -i.e. lesions- visibles tant a la mamografia com a la MRI. El problema en 2D consisteix a projectar directament la posició d'aquesta lesió sobre la mamografia i calcular la distància Euclidiana respecte al landmark original. No obstant això, per a localitzar la posició en 3D, dins de la MRI del pit, des de les posicions corresponents a les mamografies, solia requerir de mètodes complexos i costosos per tal de desfer la inherent compressió del model biomecànic. Aquest fet, ens va portar a proposar una nova metodologia ràpida i eficient per localitzar la posició d'una lesió a la MRI a partir de les posició prèviament localitzada a les mamografíes. Al localitzar múltiples raigs provinents de diferents projeccions del pit (cranio caudal (CC) i mediolateral obliqua (MLO), principalment) la posició 3D del landmark es pot calcular com la intersecció (o el centre de masses dels punts més propers) entre els raigs. Aix, utilitzant una metodologia similar a la proposta per projectar el teixit dens des de la MRI, es pot realitzar un back-projection directament des de les mamografies que permet localitzar la trajectòria del raig en el nostre model original, evitant simular la descompressió del pit. Per accelerar el procés de localitzar el punt d'intersecció, proposem un senzill algorisme que subdivideix els raigs i que permet reduir-ne l'espai de cerca. Quantitativament, el nostre model redueix aquest espai de búsqueda fins a sis-centes vegades, comparat amb una cerca tradicional punt a punt. Gràcies a aquest fet, el temps emprat en calcular la intersecció ronda els 8 ms podent ser aplicable en la pràctica clínica com una aplicació en *real time*. A més, els errors de registre mesurat són propers a 1 cm, millors que els anteriorment proposats.

Per concloure, s'ha avaluat tamb la possibilitat d'utilitzar una altra informació, a part

de la quantitat del teixit dens, per a realitzar el registre entre les imatges. D'aquesta manera, centrem la nostra atenció en el gradient del teixit dens. Mentre que la metodologia (extracció del model biomecànic i optimització dels paràmetres) és similar als treballs realitzats anteriorment, el gradient del teixit dens de les imatges de ressonància magnètica i la mamografia s'extreu mitjançant tècniques de processament d'imatges. El gradient de MRI és projectat cap a la mamografia mitjançant dues tècniques diferents. La primera utilitza l'acumulació de la derivada direccional obtenint una valor escalar, comparable amb el mòdul dels gradients obtinguts a la mamografia. La segona, acumula el gradient considerant cada direcció independentment, produint un vector que pot ser comparat amb les derivades direccionals obtingudes de la mamografia mitjançant una mètrica de correlació de gradient. Per proveir d'una comparativa justa amb els mètodes proposats en l'estat de l'art, es proposa tamb un registre tradicional basat en intensitats on s'utilitza un model polienergètic, en comptes dels models monoenergètics prèviament proposats, convertint la MRI en una imatge pseudo-CT. Els nostres resultats mostren una millora en el registre utilitzant els valors escalars del gradient respecte el mètode tradicional basat en intensitats. A més, s'ha avaluat el diferent comportament obtingut utilitzant materials isotròpics i anisotròpics per al model biomecànic i s'han buscat correlacions amb diversos factors d'interès, com ara la glandularitat del pit i la posició interna de la lesió. Els models anisotròpics han mostrat una millora respecte els models isotròpics, mentre que la glandularitat i la posició interna dels *landmarks* han mostrat un grau mitj de correlació pel que fa a l'error del registre. D'altra banda, s'ha aconseguit reduir el temps de registre a la meitat en relació als registres anteriorment realitzats.

En definitiva, aquesta tesi ajudarà a radiòlegs i metges a comprendre les petites variacions del teixit glandular que poden ser clarament visibles en una modalitat però no en l'altra. A més, l'avaluació de la informació pot orientar els investigadors cap a segmentacions més precises que tinguin en compte l'efecte parcial en els voxels de MRI, així com la millora del registre entre les dues modalitats d'imatge, no només per mètodes basats en intensitats sinó considerant tamb informació addicional com el gradient. Finalment, els nostres mètodes inclouen propostes per a desenvolupar aplicacions en temps reals i amb intervals de temps acceptables en la pràctica clínica diària.

1 Introduction

Each year in Europe, 500,000 new cases of breast cancer are diagnosed and 143,000 women die from this disease [7]. In order to reduce this mortality, early breast cancer detection is a pivotal step, since the patients' treatment would be less aggressive and more effective [20]. Magnetic Resonance Imaging (MRI) and X-ray mammography, together with ultrasound imaging, are the imaging modalities used for the early detection and diagnosis of breast diseases [3]. The physics underlying each modality are different and provide complementary information about the internal tissues of the breast.

X-ray mammography is considered the gold standard in early disease detection, and is widely used in national screening programmes [29, 32, 40]. It is an optical process in which the breast is exposed to an X-ray beam to obtain one or more 2D images of the internal tissue distribution. The relative prevalence of glandular and adipose tissues in the breast is inferred from the image pattern of brightness. Since glandular tissue has a larger X-ray attenuation coefficient than fatty tissue, it appears brighter on mammograms [2]. However, X-ray images present decreased sensitivity in dense breasts, resulting in limited applicability in these cases. Moreover, the 2D-projection makes locating suspicious lesions within the uncompressed breast difficult, a crucial step for biopsy procedures.

Hence, MRI and ultrasound scans are acquired to overcome some of these issues, but they have other limitations. Breast MRI uses a powerful magnetic field and pulses of radio waves to compute detailed 3D images of the internal structure based on the amount of water each tissue contains. Since glandular and fat tissues have different water concentration, they can be differentiated [14]. However, MRI suffers from low specificity and, usually, requires the use of contrast agents. On the other hand, ultrasound imaging is difficult to interpret due to its relatively low spatial resolution, noise and contrast.

Several studies have demonstrated that a combination of these modalities leads to a more accurate diagnosis and, hence, a more effective medical treatment of the breast diseases [24]. However, the fusion of the information from different modalities is a challenging task. Not only due to differences in the physics of each imaging modality but also because internal tissues are deformed differently due to the patient positioning and movement restrictions applied during the acquisition in each modality.

The main goal of registration is to establish a spatial correspondence between two images. In the case of breast imaging, and considering, in particular, the multimodal MRI-mammography registration, the physics underlying each modality and the deformable nature of the breast need to be considered. The aim of this thesis is to establishing correspondences

between breast MRI images and X-ray mammograms, using a patient-specific finite element (FE) model. The biomechanical model is extracted from the MRI volume and compressed, mimicking the mammographic acquisition.

1.1 Image formation

The image formation depends on both the physics underlying the image modality as well as the deformation performed during the acquisition. During the mammographic acquisition, the woman stands upright while the breast is highly compressed between the paddle and breast support. Then, an X-ray beam is applied in order to obtain internal tissue images. However, during MRI acquisition, the patient lies in the prone position with the breast hanging downwards into the radiofrequency receiver coil and is subjected to magnetic fields and radiofrequency pulses in order to yield the excitation of the atoms.

The aim of this section is to briefly introduce the basis of the image formation for both X-ray mammography and MRI images, not only from a theoretical point of view but including some practical considerations, such as artifacts and quality image requirements, of the two modalities.

1.1.1 X-ray mammography

During this thesis, the reference book in X-ray mammography has been the *European guidelines for quality assurance in breast cancer screening and diagnosis* [34]. Other books have been considered for obtaining complementary information [2, 16]. Even when the European guidelines document does not represent a text book about mammography, this book is almost mandatory for understanding the patient positioning and the requirements of the image acquisition and quality. Therefore, this section is not only focused on the process belonging to the image formation but also in the mammographic acquisition.

Mammography is the process of examining the internal structure of the breast, for diagnosis or screening purposes. The mammographic images are obtained using ionizing radiation -i.e. low-energy X-rays. During the image acquisition, the X-ray beam traverse the breast and the beam intensity is attenuated by the tissue. Formally, the expression, which describes the attenuation of the ray beam with respect to the properties of the material, is known as the Beer-Lambert law and is expressed as follows:

$$I = I_0 e^{-\int_0^L \mu(x)dx} \tag{1.1}$$

where I represent the transmitted radiation, I_0 is the incident energy flux and μ the material attenuation coefficient. The attenuation is defined by the material thickness, L, traversed by the ray, in the direction x. Usually, in mammography, the anode is composed of Rhodium, Molybdenum or Tungsten while the filter material is Rhodium, Molybdenum, Silver or Aluminium. The photon energy spectrum during the mammographic acquisition is related to the anode and filter material, as well as the filter thickness and the tube voltage (usually around 30 kVp).

The history of mammography began in 1913, when Albert Salomon (1883-1973), surgeon at the Royal Surgical University Clinic (Berlin, Germany), used X-ray technologies to analyze 3,000 mastectomies, localizing microcalcifications, differentiating between healthy and non-

healthy tissue in X-ray images and figuring out multiple types of breast cancer [21]. However, this technology was not applied in the clinical practice.

In 1930, Stafford L. Warren (1896-1981), physician and radiologist at Rochester Memorial Hospital (New York, USA), published "A roentgenologic study of the breast" [42], where 119 patients were analyzed using a stereoscopic technique to perform *in-vivo* mammographies. In this study, 54 cases (from 58) were diagnosed with breast cancer before subjecting the patient to surgery. This fact sparked intense interest in the technique around the world. Other pioneers in this field of study, such as Walter Vogel, lecturing to the Leipzig Medical Society (Lipzig, Germany), Paul S. Seabold (USA), Stafford Warren, University of Rochester (NY, USA), Jacob Gershon-Cohen, radiologist and medical author at Temple University School of Medicine (Philadelphia, USA), Robert L. Egan (USA) among others, established the root of the modern mammography [12].

In the 1960s, radiologists carried out mammographic exams using general purpose X-ray tubes, without performing the breast compression. The image acquisition was similar to chest X-rays images, obtaining a poor contrast and underexposure artifacts in certain areas such as close to the chest wall. In 1965, Charles-Marie Gros (1910-1984), professor of medicine at the University of Strasbourg (Strasbourg, France), in collaboration with the *Compagnie Générale de Radiologie* (CGR), introduced the first fully-dedicated X-ray device, the *Senographe* machine, where the breast was highly compressed to acquire mammographic images [5].

The importance of breast compression lies in:

- the scattered radiation diminishes, thus improving the contrast of the images,
- the internal structures of the breast are separated, providing a better visualization of the tissues,
- radiation dose is reduced and, also, the image blurring due to movement is reduced.

The role of the radiographer, from the position to the compression of the breast, is essential to producing high quality mammograms. The radiographer places the patient's breast on the support, trying to cover the maximum possible breast area to visualize all possible lesions and, then, the breast is compressed using the second paddle. The compression of the breast tissue should be tolerable by the patient but firm enough to immobilize the breast. The breast should be properly compressed, but no more than the necessary to achieve a good image quality. Too much compression will only cause the woman pain.

Furthermore, mammograms are acquired from different angles. In screening mammography and breast diagnosis, two standard projection views are mainly used: the cranio-caudal (CC) and mediolateral oblique (MLO) projections. In the first case, the breast is compressed vertically and the X-ray is projected in the direction from the head to the toes of the patient. In the second case, the compression paddles are situated in a given oblique angle, and the projection is performed from one shoulder to the opposite hip of the patient. Figure 1.1 shows the CC and MLO mammographic acquisition, obtained from a clinical scenario [1].

High quality images require the absence of skin folds, overlying artifacts and motion blurring among others issues due to the exposure or the development technique. Common artifacts in mammography are a poor breast compression, that yields pale images, and

[1]The images were acquired by Dr. Oliver Diaz at the UDIAT centre diagnostic (Corporació Sanitària Parc Taulí, Sabadell, Barcelona), in 2016

(a) (b)

Figure 1.1: Mammographic acquisition in (a) CC- and (b) MLO- position.

movement blur, incorrect positioning, obtaining skin folds or poor location of the nipple, pectoral muscle or inframammary angle (in MLO-projections).

In particular, the European guideline exposes that the criteria for CC requires that the breast needs to be centred in the image, with the nipple in profile, and exposed as much as possible, except the most lateral and axillary part. Other considerations exposed in the guidelines are:

- the medial border of the breast is shown,
- as much as possible of the lateral aspect of the breast is shown,
- if possible, the pectoral muscle shadow is shows on the posterior edge of the breast,
- the nipple should be in profile, and
- symmetrical images.

Regarding the MLO, the pectoral muscle needs to be clearly visible in the image, at a correct angle, as well as the inframammary, without overlying tissues. In this case, the European guidelines exposed that the image assessment of the MLO view are:

- all the breast tissue is clearly shown,
- the nipple should be in profile,
- the pectoral muscle needs to be to nipple level,
- the inframammary angle is clearly demonstrated, and
- symmetrical images.

Figure 1.2 shows an example of CC and MLO mammograms obtained from the same patient during a screening study. Other additional projections can be performed by the radiographer, including the lateral view (lateromedial/mediolateral) and the extended craniocaudal view. Furthermore, diagnostic mammography may include these and other views, including geometrically magnified and spot-compressed views of the particular area of concern.

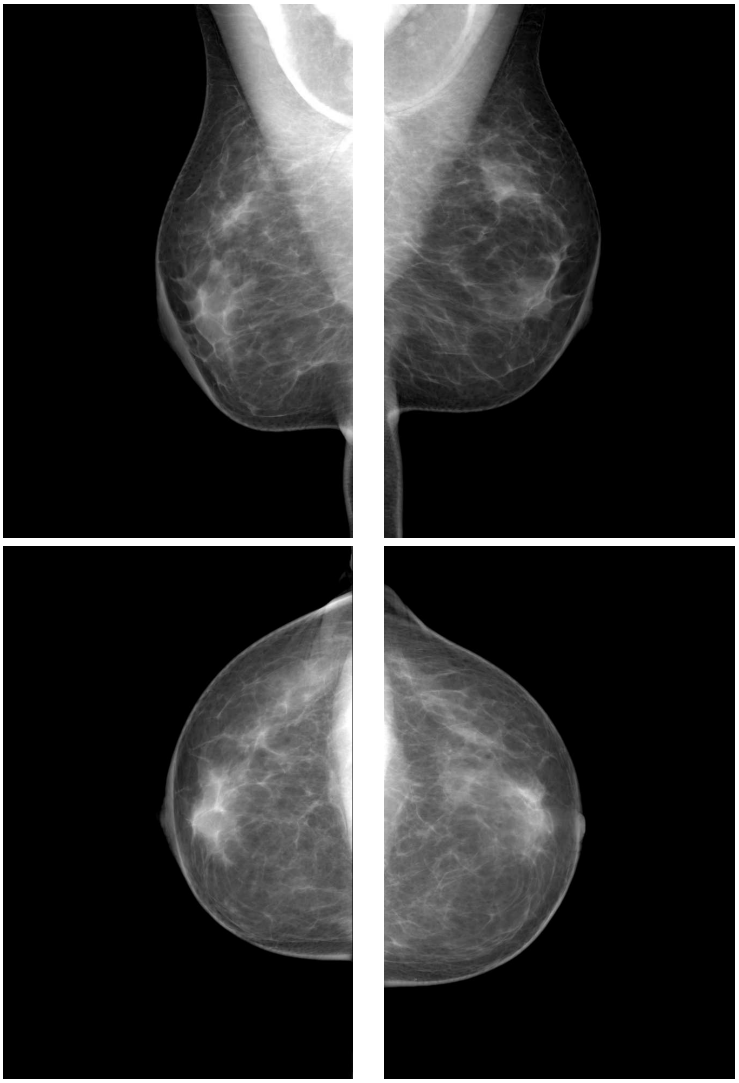

Figure 1.2: (Up) Medio-lateral oblique and (down) cranio caudal projections obtained from the same patient.

The *Senographe* represents the beginning of the modern mammography. During the 1980s and 1990s, improvements in the technology allow reducing the radiation dose, obtaining a high contrast between the internal tissue of the breast by means of screen films. At the begin of this century, the analogic screen-film mammography is being relegated by digital mammography -i.e. Full-Field Digital Mammograms (FFDM). Digital mammography is a specialized form of mammography that uses digital receptors and computers instead of x-ray films to help examine breast tissue for breast cancer. The electrical signals can be read on computer screens, permitting more manipulation of images to theoretically allow radiologists to more clearly view the results.

From the patient point of view, the mammographic acquisition is performed in the same way while, in the radiologic practice, digital images provide better quality, increasing the tissue contrast and using a lower radiation dose compared to traditional screen-film mammography. The first FFDM system was approved by the FDA in the U.S. in 2000. Concern by the FDA that digital mammography equipment demonstrate that it is at least as good as screen-film mammography at detecting breast cancers without increasing breast dose or

the number of women recalled for further evaluation.

Furthermore, FFDM also carries potentially significant advantages for technological developments such as digital breast tomosynthesis (DBT), X-ray phase contrast and dark-field mammography and 3D reconstructions.

1.1.2 Magnetic resonance imaging

During this thesis, the reference book of breast MRI has been *Breast MRI. Fundamentals and Technical Aspects* [14]. This section aims to briefly introduce the physic underlying, tissue excitation and relaxation and, finally, the MRI image formation. For a more detailed description, we encourage the reader to review specialized literature that may be useful in some parts of this work.

MRI allows separating a sample or region of tissue into individual volume elements (voxels) and producing images based on the total signal from the nucleus of interest in each voxel. Subatomic particles, such as protons and electrons are quantized particles (they obey the laws of quantum physics) with discrete mass, charge and spin. Therefore, the magnetic dipole moment is also discrete and can be oriented by means of an externally applied magnetic field.

The orientation of the particles can be performed in two different ways: the magnetic dipole is pointed either along the magnetic field lines (named *up* state) or opposite the magnetic field lines (named *down* state). These two orientations have slightly different energy levels (usually, establishing the *down* orientation requires more energy than the *up* orientation). The magnetic dipole moments of all materials -i.e. tissues- are defined by the magnetic moments and the number of protons and neutrons composing the nucleus. The collective effect of a huge number of nuclei produces a net tissue magnetization.

In MRI, the hydrogen atoms of the molecules are stimulated when the body is subjected to a strong magnetic field, yielding a measurable tissue magnetization. The difference in the energy of the two states (*up* and *down*), ΔE, depends only on the nucleus's magnetic dipole strength, μ, and the externally applied magnetic field, B_0. Formally, this is expressed as follows:

$$\Delta E = \mu B_0 \tag{1.2}$$

A typical B_0 value for breast MRI is 1.5 T[2]. In perspective, the earth's magnetic field is about half a gauss (1 Tesla = 10,000 gauss) at the earth's surface. Therefore, a 1.5 T scanner has a magnetic field strength about 30,000 times stronger than the earth's magnetic field.

The yielded energy depends only on the nuclear constituent and the external magnetic field and it is expressed as follows:

$$\Delta E = h\nu_0 = \mu B_0 \tag{1.3}$$

where ν_0 is the Larmor frequency in units of Hertz or cycles per second, μ is the magnetic moment of the nucleus or particle of interest, and B_0 is the magnetic field strength in which

[2]MRI scanners using magnetic fields with $B_0 = 3$ T are also available to obtain breast images.

the nucleus resides. The Larmor frequency for the hydrogen nucleus is given by the Larmor equation:

$$\omega_0 = \gamma_p B_0 \tag{1.4}$$

where $\gamma_p = \frac{2\pi\mu_p}{h}$ is the gyromagnetic radio of the proton. The gyromagnetic ratio of a particle or nucleus is the ratio of its magnetic dipole moment (μ) to its spin angular momentum, which is given in units of $\frac{h}{2\pi}$. Considering the previous example, using a magnetic field with strength $B_0 = 1.5$ T, the Larmor frequency of the hydrogen atom is $\nu_0 = 63.90$ Hz.

The Boltzmann equation, from statistical mechanics, describes the imbalance of hydrogen dipoles contained in a voxel of tissue, when it is subject to a strong magnetic field. Therefore, the difference in the number of hydrogen nuclei in the two energy states(*up* and *down*) is determined by the ratio of the energy difference between the two magnetic dipole energy states and the thermal energy of tissue.

After applying the magnetic field, the challenge in MRI is to measure tissue magnetization. A radiofrequency (RF) transmitter coil, transmitting at the Larmor frequency of the hydrogen atom, is used to excite nuclei, in order to flip the magnetization in tissue away from the direction of B_0. In a reasonable short amount of time (on the order of tenths of seconds) the magnetization decays away and the signal is measured.

Faraday's law of induction describes the electromagnetic induction that can be measured by the RF receiver coil. RF receiver coils measure the signal emitted from the excited tissue. The coils, and the associated electronics, are built to ressonate at the Larmor frequency, which depends on the scanner's magnetic field strength. In breast imaging, the RF receiver coil is specialized breast coil. In the early days of breast imaging, RF receiver coils were unilateral but today, most of them, are bilateral. Breast coils are designed to receive signal from the breast, axilla and chest wall but not from the entire upper torso. This is because the larger the sensitive volume of the receiver coil, the more unwanted noise is measured, interfering with the signal from the breast that you would like to measure.

Relaxation times are strictly MR-based parameters that describe the re-growth of longitudinal magnetization (T1) and loss of transverse magnetization(T2) after a RF pulse. Two separate phenomena take place after a 90° pulse is applied. One phenomenon is the recovery of the longitudinal magnetization, described by the time constant T1 and called spin-lattice relaxation, T1 relaxation or T1-recovery. The other phenomenon is the decay of transverse magnetization, the magnetization that is flipped into the transverse plane,which is described by the time constant T2 or T2* and is called spin-spin relaxation or T2-decay. In 1971, Damadian [4] demonstrated that the MR relaxation times, specifically the T1/T2 ratios of tissues, could be used to distinguish cancer from normal tissues.

T1-relaxation or T1-recovery describes the recovery of longitudinal magnetization along the direction of the static magnetic field, B_0 just after applying a RF pulse. An example of a T1-weighted MRI image is shown in Figure 1.3. In the breast, T1 values are shortest for fat (about 250 ms at 1.5 T), intermediate for fibroglandular tissues (about 700 ms at 1.5 T) higher for most lesions, including cancers (800 ms to 1 second at 1.5 T), and highest for non-bloody cystic fluids (about 3 second at 1.5 T). The reason that T1 is higher for most breast lesions, including cancers, than for normal fibroglandular tissues is that lesions tend to have higher water concentration, and therefore fewer macromolecules per unit volume, than normal breast tissue. The exceptions to this rule are lesions with high fat content, such as lipomas or lesions with a high fibrous content, both of which have shorter T1 values than normal fibroglandular tissues.

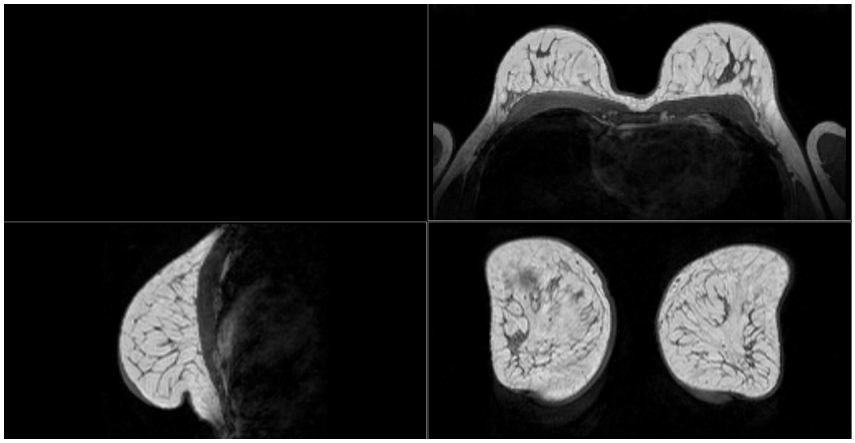

Figure 1.3: Example of T1 non-fat suppressed MRI image

The heterogeneity of T1 values in cancers, benign breast lesions and fibroglandular tissues means that breast lesions are often isointense or slightly darker than, normal fibroglandular tissue, making suspicious lesions difficult to detect in T1-weighted sequences without the addition of paramagnetic contrast agent.

The dephasing of the measurable MR signal, the transverse magnetization is described by T2. T2-type decay describes the exponential loss of transverse magnetization immediately after a 90 pulse. T2 is the parameter that describes how quickly the magnitude of the transverse magnetization decreases over time. Tissues with shorter T2-values have a more rapid loss of transverse magnetization. In the breast, fat and normal fibroglandular tissues have the shortest T2 values ($60 - 80$ ms). Most of breast lesions, including cancers, have slightly longer values($80 - 100$ ms) and cystic fluids have the longest T2-values (several hundreds ms)

Breast cancers, on average, were found to have T1 and T2 values higher than those of normal fibroglandular tissue, but lower than those of many benign breast lesions. This fact makes breast cancers appear slightly darker than normal fibroglandular tissues on unenhanced T1-weighted images and somewhat brighter than normal fibroglandular tissues on unenhanced T2-weighted images. In addition, due to the heterogeneity of both benign and malignant breast lesions, significant overlap was found between the T1 and T2 values of breast cancers and benign breast lesions such as fibroadenomas.

By the mid-1980s, contrast agents based on the rare-earth element gadolinium (Gd) were developed to enhance cancers in the brain and spinal core. The first Gd-based contrast agent was approved by the FDA for central nervous system indications in 1988. Gadolinium is a paramagnetic ion due to the presence of the unpaired electrons in the outer shell. When placed in a strong magnetic field, these unpaired electrons align with the field and their electron magnetic dipole moments add together, creating a strong local magnetic field in the vicinity of the Gd ion. Elemental gadolinium is toxic. To make gadolinium safe for human injection, it is chelated by a molecule that renders the Gd-compound non-toxic.

Invasive breast cancers tend to exhibit more rapid and more focal uptake of contrast agent than normal fibroglandular tissues or benign breast lesions. After uptake, invasive breast cancers tends to exhibit irregular margins and some exhibit washout of contrast agent, which is untypical of benign lesions. The time after injection during which invasive breast cancers demonstrate greater enhancement than surrounding fibroglandular tissues is usually 5 to 10 minutes, with increasing contrast between lesion and normal fibroglandular

tissues for the first 1 to 3 minutes after injection a slowly decreasing contrast after that. By 6 to 10 minutes after injection, normal fibroglandular tissues have increased in signal intensities to the point that invasive breast cancers are far less distinct relative to background fibroglandular tissues.

Percent signal increase ($\%SI$) in enhancing breast lesions is defined as the difference between enhanced signal (S_{post}) and unenhanced signal (S_{pre}) relative to the amount of unenhanced signal:

$$\%SI = \frac{S_{post} - S_{pre}}{S_{pre}} \cdot 100\% \tag{1.5}$$

in a ROI that is fully contained within the enhancing lesion, using the same ROI placement for pre- and post-contrast images.

Beyond the primary acquired images, several image post-processing approaches, such as subtracted images, maximum intensity projections (MIP) of subtracted data or time-enhance curves for suspicious lesions can be applied in order to interpret the supplementary data provide by DCE-MRI.

Image subtraction involves computing the difference between pre-contrast images from each post-contrast image. Difference image represents the change in data due to contrast administration. Furthermore, a MIP can be performed from the difference image, yielding a 2D image which allows localizing brightest objects -i.e. enhancing areas- in one single 2D image. To examine details of enhancing nodes or lesions, primary or subtracted planar images should be examined in addition to MIP images.

Like other breast imaging modalities, breast MRI can have image artifacts. The complexity of MRI makes artifacts more difficult to recognize and their causes more obscure than in mammography. Among others, blurring or ghosting, due to the motion of the patient, bias field, aliasing, truncation or reconstruction and metallic artifacts, including metallic biopsy marker clips artifacts, are the most commons errors in breast MRI.

1.2 Motivation

Since 1970, X-ray mammography is a valuable technique for detection of breast cancer and is considered the gold standard in early disease detection in screening programs [29, 32, 40]. MRI was introduced in the clinical application in the 1980s and is often used as a complementary modality. However, so far, MRI is not part of the initial diagnostic work-up. The full role and place of MRI in breast diagnosis is still being evaluated, whilst the procedure is becoming more established and widely used. MRI is a proven value in helping to establish the degree of disease present. It has also been shown to have a high sensitivity in the detection of malignancy in younger women of high risk groups.

MRI images, and, in particular, DCE-MRI series, can be acquired to complement to mammography, for instance, in the following cases:

- Problem solving when findings from conventional imaging (MG or ultrasound) are inconclusive as DCE-MRI has been shown to have high sensitivity but poor specificity.
- Screening in patients with dense breast who are at increased risk and more frequent

screening in patients at high genetic risk of cancer. In particular, those known to be more radiosensitive.

- Monitoring and assessing the tumor response of patients treated with neoadjuvant chemotherapy.
- Staging of women with breast cancer. In particular for women with dense breasts and patients with histologic evidence of invasive lobular carcinoma.
- Determining the primary lesion, when this is not visible in mammography. For example axillary metastases with and occult primary tumor.
- Imaging after breast conservative therapy, for example to evaluate possible residual disease of further evaluate suspected recurrence.

In the last decades, researchers have focused their efforts on developing algorithms to fuse the information of different imaging modalities. In the cases, exposed below, registration between MRI and mammography could help disambiguate among them. A common process consists in using a finite element biomechanical model that simulates in a physically realistic way the deformations produced in both the surface and internal tissues of the breast during the mammographic acquisition. Biomechanical models have been widely used in various medical applications, including brain [6], heart [38], liver [19], lungs [8] or prostate [31] imaging, composing a wide bibliography [10, 30, 33]. In breast modeling, they have been used in several challenging problems, such as the co-localization of information between different image modalities [23], temporal studies [36], identifying lesions or tumors [17], tracking of these lesions during biopsy [1], review of the progress of suspicious lesions or evaluation of the effectiveness of treatments and, even, aiding implant selection for breast augmentation procedures [11].

The aim of this thesis is to analyze the correlation of the information contained in both breast MRI and X-ray mammography, in order to improve the registration and to establish an accurate correspondence between the two modalities. To achieve this purpose, this thesis is mainly divided into two big parts. The first part is focused on evaluating the similarity between the information contained in both breast MRI and X-ray mammography, specifically the glandular tissue distribution obtained from the two image modalities. The second part introduces several algorithms to establish spatial correspondence of lesions and susceptible areas.

1.3 Objectives

The aim of the IA-BioBreast, ASSURE and SMARTER projects is to figure out biomarkers such as breast density and to correlate the information contained in different image modalities. This thesis focus the attention in MRI and mammographic images and its aim is to analyze the similarity between the information contained in the two modalities as well as to propose new methods to correlate this information.

To achieve this goal, we defined the following objectives:

- To review of the literature. First step is to analyze the proposed methodology to correlate the MRI and mammographic images. We focus our attention in that methodologies based on patient-specific biomechanical model and, in particular, those performing a realistic deformation using a finite element analysis.

- To analyze the reliability of automatic density measures using FFDM. Using the commercial software Volpara^{TM}, the amount of glandular tissue can be extracted for every pixel in the mammograms. The aim of this part is to evaluate the share information between two mammographic acquisitions that are acquired in a short time frame.

- To analyze the correlation of the glandular tissue between MRI and mammography. Since the two image modalities have a different physics underlying, we aim at evaluating the similarity between the information provided by both modalities. In particular, we focus our attention in the glandular tissue, with the aim of evaluating not only the shared information -i.e. amount of glandular tissue- but also the structural similarity between the two image.

- To propose new methods to co-locate susceptible areas o lesions. Once the correlation of the glandular tissue has been evaluated, the main idea is to develop new registration algorithms based on internal landmark or unused features, so far. We aim at providing fast and computational efficient algorithms, reducing the computational cost of the process.

1.4 Thesis outline

This thesis is presented as a compendium of publications. A brief introduction of the papers composing this thesis is exposed as follows:

- Chapter 2 introduces a step-by-step review in breast MRI to X-ray mammography registration using patient-specific FE biomechanical models. The combination of these modalities leads to a more accurate diagnosis and treatment of breast diseases. In contrast with other reviews, we do not only expose the overall process of compression and registration but we also include main ideas, describe challenges and provide an overview of software options in each step of the process. Extracting an accurate description from the MR images and preserving the stability during the finite element analysis require an accurate knowledge about the algorithms used, as well as the software and underlying physics. The wide perspective offered makes the paper suitable not only for expert researchers but also for graduate students and clinicians. We also include several medical applications in the paper, with the aim to fill the gap between the engineering and clinical performance.

- Chapter 3 aims to evaluate the spatial glandular tissue distribution as well as the automatic density measures provided by the commercial software Volpara^{TM} Density Maps using a dataset composed of repeatedly acquired full-field digital mammograms, where each pair was acquiredwithin a short temporal window. The global measures provided by Volpara^{TM}, such as breast volume (BV), volume of glandular tissue (VGT) and volumetric breast density (VBD), are compared between the two acquisitions. Furthermore, the evaluation of the information is performed using histogram similarity metrics, such as intersection and correlation, and local measures, such as statistics from the difference image and local gradient correlation measures, are used to evaluate the structural similarity.

- Chapter 4 aims to compare the breast parenchymal distributions (i.e. density maps) obtained from FFDM and MRI. To achieve this goal, we have developed a fully automatic framework which registers MRI volumes to X-ray mammograms using a subject-specific biomechanical model of the breast. The optimization step modifies the position, orientation and elastic parameters of the breast model to perform the alignment

between the images. When the model reaches an optimal solution, the MRI glandular tissue is projected and compared to the one obtained from the corresponding mammograms. To reduce the loss of information during the ray-casting, we introduce a new approach that avoids resampling the MRI volume. In the results we focus our efforts on evaluating the agreement of the distributions of glandular tissue, the degree of structural similarity and the correlation between the real and synthetic density maps.

- Chapter 5 introduces a fast method to localize the 3D position of the lesion within the MRI, using both CC and MLO mammographic projections. Suspicious lesions in the MRI volume can be projected into the 2D mammographic space, however, most registration algorithms do not provide the reverse information, avoiding to obtain the 3D geometrical information from the lesions localized in the mammograms. The overall process consists of indexing the tetrahedral elements of the biomechanical model using a uniform grid. For each marked lesion in the FFDM, the X-ray path from source to the marker is calculated. Barycentric coordinates are computed in the tetrahedrons traversed by the ray. The list of elements and coordinates allows to localize two curves within the MRI and the closest point between both curves is taken as the 3D position of the lesion.

- Chapter 6 introduces two gradient-based registration approaches for breast MRI and X-ray mammography, comparing the result with a traditional intensity-based algorithm. During the intensity-based optimization, the MRI volume is transformed to a pseudo-CT image using the tissue segmentation. Therefore, digitally reconstructed radiographies (DRR) can be obtained by a direct intensity projection. Furthermore, in the gradient-based approaches, the intensity gradients of the glandular tissue are projected from the 3D MRI volume to the 2D mammographic space.

- Chapter 7 summarizes the methodology and results obtained at each chapter in this thesis, analyzing the main contribution of each one.

- Finally, Chapter 8 exposes the conclusions and the potential extension in future work, with the aim at improving the methodology and their applications.

1.5 Context

This thesis is positioned within the framework of different research projects associated with the Computer Vision and Robotics Institute (ViCOROB) of the University of Girona.

IA-BioBreast

Under the supervision of Dr. Joan Martí Bonmatí (Universitat de Girona, UdG) and in collaboration with the Universitat Rovira i Virgili (URV), the IA-BioBreast project (Ministry of Economy and Competitiveness of Spain, ref. TIN2012-37171-c02-01) aimed to research image analysis methods that focus on the development of two specific biomarkers: breast density and temporal evolution of existing lesions.

During the IA-BioBreast project, microtexture-specific techniques were developed using algorithms for feature extraction, selection and classification. Furthermore, image registration algorithms were researched for two main applications: combining images of different modalities (breast X-ray mammography, MRI and UltraSound) and registering temporal studies within the same image modality.

ASSURE

In collaboration with several international institutions (Radboud University Medical Centre, Nijmegen, The Netherlands; MeVis Medical Solutions AG, Bremen, Germany; Matakina Ltd., Wellington, New Zealand; Biomediq A/S, Copenhagen, Denmark; Mediri GmbH, Heidelberg, Germany; Fraunhofer MEVIS, Bremen, Germany; University of Manchester, UK; University Medical Centre Utrecht, The Netherlands; Institute Jules Bordet, Brussels, Belgium), the medical image group of the ViCOROB institute took part in the ASSURE project (FP7-Health 2012. ref. 306088, 01/12/2012 - 30/11/2015) under the supervision of Dr. Robert Martí.

The aim of ASSURE was to develop methods to personalize breast cancer screening, based on risk and breast density markers. New screening methods using MRI and automated breast ultrasound imaging were developed. Personalized screening will minimize the risk of a particular patient to have a cancer missed at an early stage, resulting in decreased mortality and increased quality of life due to less radical treatment options.

SMARTER

The SMARTER project (Ministry of economy and competitiveness of Spain, ref. DPI2015-68442-R, 1/01/2016 - 31/12/2018), conducted by Dr. Robert Martí Marly (Univeritat de Girona, UdG) aims at developing and evaluate novel imaging tools that can be integrated early into the screening workflow to steer image acquisition and guide the selection of appropriate personalised screening protocols; and to process imaging data in an intelligent way to minimize interpretation time. Tools are based on breast density estimation algorithms and automated breast cancer detection algorithms applied to DBT, ABUS and MRI.

2

A step-by-step review in breast MRI to X-ray mammography registration

This chapter introduces a step-by-step review in breast MRI to X-ray mammography registration using patient-specific FE biomechanical models. The combination of these modalities leads to a more accurate diagnosis and treatment of breast diseases. In contrast with other reviews, we do not only expose the overall process of compression and registration but we also include main ideas, describe challenges and provide an overview of software options in each step of the process. Extracting an accurate description from the MR images and preserving the stability during the finite element analysis require an accurate knowledge about the algorithms used, as well as the software and underlying physics. The wide perspective offered makes the paper suitable not only for expert researchers but also for graduate students and clinicians. We also include several medical applications in the paper, with the aim to fill the gap between the engineering and clinical performance.

Title: A step-by-step review on patient-specific biomechanical finite element models for breast MRI to X-ray mammography registration.
Authors: Eloy García, Yago Diez, Oliver Diaz, Xavier Lladó, Robert Martí, Joan Martí, and Arnau Oliver.
Published in: Medical Physics, vol. 45, issue 1, pp. e6-e31, January 2018. JCR RNMMI IF: 2.617, Q2(37/127)
DOI: 10.1002/MP.12673

A step-by-step review on patient-specific biomechanical finite element models for breast MRI to x-ray mammography registration

Eloy García[a)]
Institute of Computer Vision and Robotics, University of Girona Campus Montilivi, Ed. P-IV 17003, Girona, Spain

Yago Diez
Department of Mathematical Sciences, Faculty of Sciences, Yamagata University, Yamagata, Japan

Oliver Diaz, Xavier Lladó, Robert Martí, Joan Martí, and Arnau Oliver[a)]
Institute of Computer Vision and Robotics, University of Girona Campus Montilivi, Ed. P-IV 17003, Girona, Spain

(Received 7 March 2017; revised 27 September 2017; accepted for publication 3 November 2017; published 19 December 2017)

Breast magnetic resonance imaging (MRI) and x-ray mammography are two image modalities widely used for the early detection and diagnosis of breast diseases in women. The combination of these modalities leads to a more accurate diagnosis and treatment of breast diseases. The aim of this paper is to review the registration between breast MRI and x-ray mammographic images using patient-specific finite element-based biomechanical models. Specifically, a biomechanical model is obtained from the patient's MRI volume and is subsequently used to mimic the mammographic acquisition. Due to the different patient positioning and movement restrictions applied in each image modality, the finite element analysis provides a realistic physics-based approach to perform the breast deformation. In contrast with other reviews, we do not only expose the overall process of compression and registration but we also include main ideas, describe challenges, and provide an overview of the used software in each step of the process. Extracting an accurate description from the MR images and preserving the stability during the finite element analysis require an accurate knowledge about the algorithms used, as well as the software and underlying physics. The wide perspective offered makes the paper suitable not only for expert researchers but also for graduate students and clinicians. We also include several medical applications in the paper, with the aim to fill the gap between the engineering and clinical performance. [https://doi.org/10.1002/mp.12673]

Key words: finite element models, MRI, multimodal registration, patient-specific, X-ray mammography

1. INTRODUCTION

Magnetic resonance imaging (MRI) and x-ray mammography, together with ultrasound imaging, are the imaging modalities used for the early detection and diagnosis of breast diseases.[1] The physics underlying each modality are different and provide complementary information about the internal tissues of the breast. On one hand, mammography is an optical process in which the breast is exposed to an x-ray beam to obtain one or more 2D images of the internal tissue distribution. The relative prevalence of glandular and adipose tissues in the breast is inferred from the image pattern of brightness.[2] On the other hand, breast MRI uses a powerful magnetic field and pulses of radio waves to compute detailed 3D images of the internal structure based on the amount of water each tissue contains. Since glandular and fat tissues have different water concentrations, they can be differentiated.[3]

X-ray mammography is considered the gold standard in early disease detection in screening programs.[4–6] However, x-ray images present decreased sensitivity in dense breasts, resulting in limited applicability in these cases. Moreover, the 2D projection makes locating suspicious lesions within the uncompressed breast difficult, a crucial step for biopsy procedures. Hence, MRI and ultrasound scans are acquired to overcome some of these issues, but they have other limitations. For instance, MRI provides detailed 3D images but, usually, requires the use of contrast agents to localize lesions and tumors. On the other hand, ultrasound imaging is difficult to interpret due to its relatively low spatial resolution, noise, and contrast. Several studies have demonstrated that a combination of these modalities leads to a more accurate diagnosis and, hence, a more effective medical treatment of the breast diseases.[7] However, the fusion of the information from different modalities is a challenging task. Inner structures, such as nerves, blood vessel, and ligaments can be clearly visible in one modality but undetected in the others due to the physics underlying and image resolution. Moreover, internal tissues are deformed differently due to the patient positioning and movement restrictions applied during the acquisition in each modality. During MRI acquisition, the patient lies in prone position with the breast hanging downwards into the magnetic resonance machine.[8] By contrast, mammographic acquisition is performed while the patient stands upright and the breast is compressed between two paddles.[8] Furthermore, mammograms are acquired from different angles, with the craniocaudal (CC) and mediolateral oblique (MLO) projections being the most common ones. In the first case, the breast is compressed vertically, and the x-ray beam is projected in the direction from the head to the toes of the patient. In the second case, the compression paddles are situated in a

given oblique angle, and the projection is performed from one shoulder to the opposite hip of the patient.

Furthermore, the image quality depends on the acquisition protocol as well as human intervention. During the mammographic acquisition, the radiographer places the patient's breast on the support trying to cover the maximum possible area to visualize completely the internal tissues,[9] while during the MRI acquisition, the receiver coil aims not only to acquire the radiofrequency signal from the excited tissues but also to minimize breast motion (in order to avoid motion and ghost artifacts), yielding a predeformed configuration.[3] Figure 1 shows an example of precontrast T1 MRI (top row) and the CC and MLO mammographic projections (bottom row).

In the last decades, researchers have focused their efforts on developing algorithms to fuse the information of different imaging modalities considering the patient's position and loading conditions of the breast during image acquisition.[10–12] A common process consists in using a biomechanical finite element (FE) model that simulates in a physically realistic way the deformations produced in both the surface and internal tissues of the breast during the mammographic acquisition. Finite element models have been widely used in various medical applications, including brain,[13] heart,[14] liver,[15] lungs,[16] or prostate[17] imaging, composing a wide bibliography.[18–20] In breast modeling, they have been used in several challenging problems, such as the colocalization of information between different image modalities,[21] temporal studies,[22] identifying lesions or tumors,[23] tracking of these lesions during biopsy,[24] review of the progress of suspicious lesions or evaluation of the effectiveness of treatments and, even, aiding implant selection for breast augmentation procedures.[25]

The overall process, which is schematized in Fig. 2, consists of the following steps:

- Geometry extraction. It consists of building a FE model from the MRI volume of the patient.
- Mechanical deformation of the model. Simulating the breast compression suffered during the mammographic acquisition. Material parameters, internal and external forces, and boundary conditions are applied to the model. The differential equations that describe the compression of the breast between two paddles are solved using the FE method.
- X-ray image simulation. Using the compressed biomechanical model and MRI, a synthetic mammogram is generated by simulating the x-ray beam using ray-tracing procedures.
- Image registration. Finally, both, the real and the simulated mammograms, are registered, becoming spatially aligned and allowing correspondence between the regions in both the MRI and x-ray mammography images.

In this paper, we aim to review the main technical challenges in MRI and x-ray mammography registration using patient-specific biomechanical FE models that mimic the mammographic acquisition. A comprehensive analysis of the four steps previously described is performed in the paper, while, at the same time, we analyze and review the state-of-the-art software and characteristics that make it suitable to face each step. With respect to other reviews, such as those presented by Babarenda et al.[26] and Hipwell et al.[27], our survey is more focused on these specific tasks, skipping other problems, such as prone-to-supine registration[28] or multimodal 3D–3D registration.[29] We believe that issues such as an accurate synthetic mammogram generation and the resolution of the biomechanical model, as well as obtaining a suitable geometry extraction, have been overlooked in those other works. We provide a wide perspective from the biomechanical model construction, including MRI segmentation, surface mesh, and volume mesh extraction as well as methods to quantify the accuracy and quality of the reported approaches, to the physics underlying the mechanical deformation and the elastic and hyperelastic parameters reported in the literature. Moreover, none of the other works exposes the software options so far used in this task, requirements or advantages of each tool, to yield a highly accurate solution of these problems. Finally, we also include the technical aspects needed to validate these registration methods using a clinical dataset as well as several medical applications, helping to build the bridge between engineering and clinical knowledge. To conclude the document, we provide a brief summary of

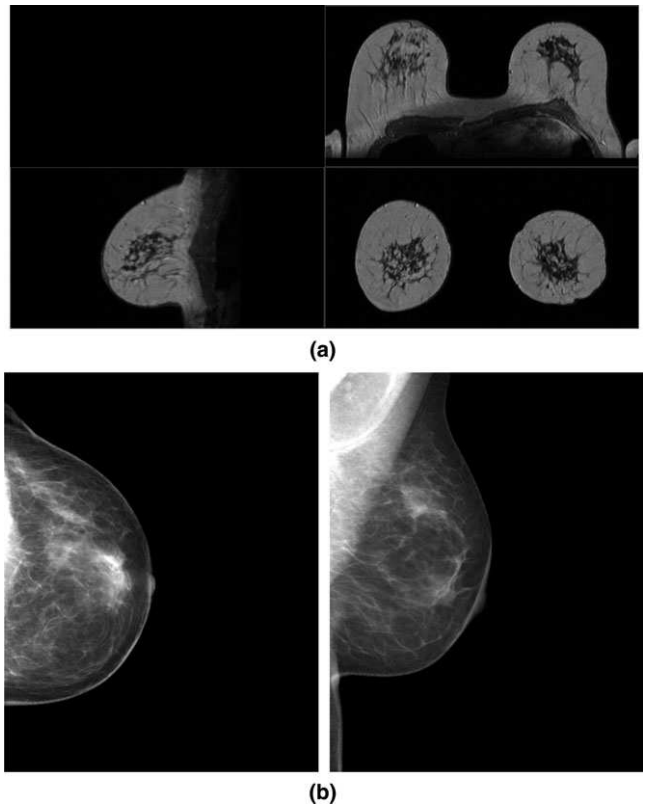

FIG. 1. T1 precontrast MR image (a) and x-ray mammographies in craniocaudal (CC) and mediolateral oblique (MLO) projections (b). Notice that in the MRI, the glandular tissue appears darker than the adipose, while in the x-ray mammograms, the glandular tissue is brighter.

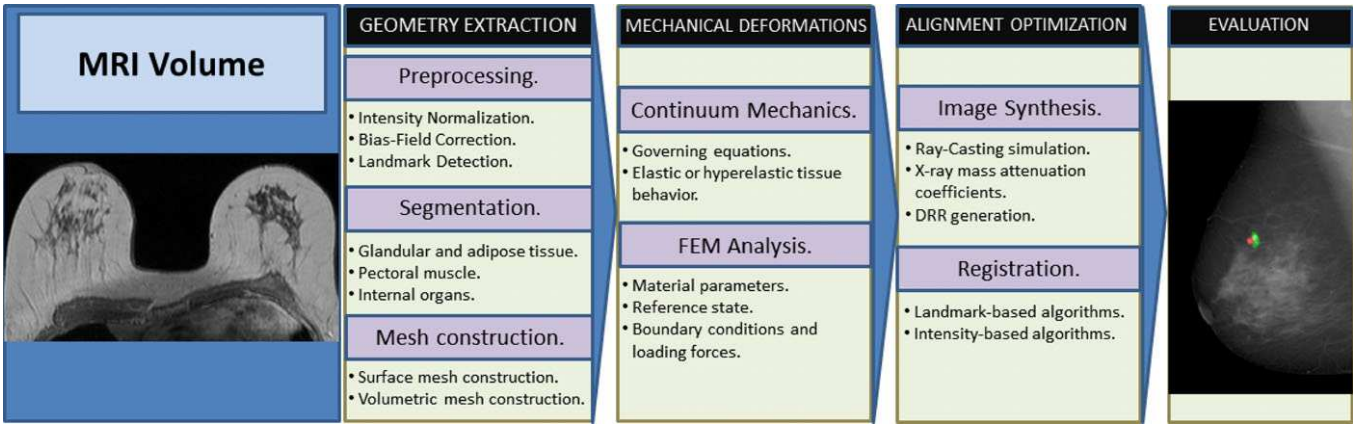

FIG. 2. A step by step MRI to x-ray mammography registration process. The overall procedure includes the FE model extraction and mechanical deformation, as well as the x-ray mammography simulation and evaluation.

software and techniques that have not been used in the current problem but they may lead the future research in the multimodal MRI–mammography registration. The wide perspective offered makes the paper suitable not only for expert researchers but also for graduate students and clinicians and from a theoretical point of view to a practical application.

The remainder of this review is organized as follows: Section 2 briefly introduces the breast anatomy necessary for a full comprehension of the overall MRI–mammography registration. Section 3 describes the breast geometric information extraction as well as the knowledge about solid mechanics, FE analysis, and material approaches needed to obtain the 3D model from the MRI and to compress it according to the mammographic views. Section 4 introduces the methods that allow the correct positioning and registration of the 3D model with the given mammograms. Section 5 performs an overall review of the results obtained by the different approaches found using the state-of-the-art, while Section 6 discusses other software and improvements that can be made in the different parts of the MRI–mammography registration. The paper ends with conclusions.

2. BREAST ANATOMY

Female breasts are situated on the chest, between the second and sixth rib. Each breast is extended from just below the clavicle to the axilla and across the sternum. The tail of the breast, which is extended into the axilla (called axillary tail of Spence), is an important area because breast cancer masses can develop in this region, although they seem to be located outside the proper breast.[30]

The breast is mainly composed of adipose and glandular tissues. Each breast has several sections (lobules) that branch out from the nipple and are linked by a network of ducts. The lobules are responsible for the milk production during lactation. Spaces around the lobules and ducts are filled with ligaments and adipose and connective tissues. Figure 3 shows the internal structure of the female breast.[186] The breast does not have muscular tissues but includes lymph vessels, lymph nodes (deep to the breast or under the axilla), and blood vessels. Additionally, several nerves are present in the breast, including nerves in the chest and arms and sensory nerves in the skin of the chest and armpit.[31]

The pectoral muscle lies under the breast, separating it from the ribs. Connective tissue and ligaments provide support to the breast. The size and shape of the breast are mainly determined by the amount of adipose tissue and ligaments (Cooper's ligaments), respectively. The breast tissue is encircled by connective tissue (fascia mammae). The deep layer of the fascia sits on top of the pectoral muscle. On the other hand, the superficial layer sits under the skin.[32] The superficial fascia is separated from the skin of the breast by subcutaneous fat between 0.5- and 3-mm thick.

Breast tissue changes at several times during a woman's life. Mainly, these changes occur during puberty, the menstrual cycle, pregnancy, and after menopause, responding to

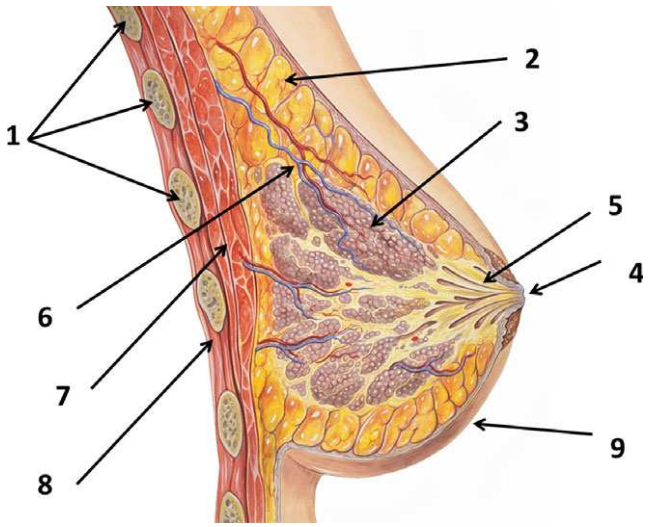

FIG. 3. Anatomy of the healthy female breast. Labels represent: (1) ribs, (2) adipose tissue, (3) lobules, (4) nipple, (5) lactiferous duct, (6) blood vessels, (7) chest wall, (8) pectoral muscle, and (9) skin. Original authors: Patrick J. Lynch, medical illustrator, via Wikimedia Commons.

hormonal changes, and they affect the breast by varying its size and shape and by changing the elasticity of the ligaments. Furthermore, the breast density (the ratio between the glandular and adipose tissues) tends to be higher in younger women. This implies that glandular and ductal tissues are replaced by fatty tissue.

3. PATIENT-SPECIFIC BIOMECHANICAL MODELING

A biomechanical model stores information about the geometry and structure of the organs, and provides a physics basis to simulate mechanical deformations. The motivation to simulate breast biomechanics corresponds to the need to obtain a physically realistic deformation in both the surface and internal tissues of the breast. A reliable biomechanical breast model is essential to predict the deformation of the internal tissues and movement of suspicious lesions in the breast during imaging procedures, simplifying the clinical tumor-tracking problem.

Computational modeling theories have been used to simulate soft-tissue biomechanics. Briefly, these theories can be categorized into nonphysical models, mainly statistical deformation or geometrical deformable models,[33] and physical models, which include heuristic (mass–spring[34] or mass–tensor models[35]) and continuum mechanics approaches. Heuristic models are less computationally expensive than continuum mechanical models and can be used to solve time-dependent mechanical problems in real-time simulations. These methods have been used to model breast deformations; for instance, in breast augmentation procedures,[34] follow-up of breast diseases,[36] and temporal MRI registration,[35] and they show a good performance when small deformations are simulated. However, they produce nonphysical solutions, conversely to continuum mechanics and the FE method. Furthermore, the FE method provides increased accuracy for large deformations compared to heuristic models and can be used to model the interrelationship of different tissue types by applying displacements, forces, and restrictions to the movement.[37]

To describe a precise physical behavior, a realistic biomechanical model of the breast requires accurate knowledge about internal and external factors, such as internal tissue distribution, an suitable geometric model of the anatomical area, an unloaded reference state as a starting loading condition, a suitable set of valid boundary conditions, and an appropriate material constitutive model. Therefore, to obtain the model, several aspects need to be addressed:

- The geometry is built using the skin and pectoral muscle surfaces. Usually, the breast is separated from the body and the internal tissues of the breast are segmented.
- Using the segmented regions, a volumetric mesh is constructed. This model is either composed of one single tissue — i.e., all of the elements belong to the same material class — or of different tissues, where the elements are assigned to the materials considering the previous segmentation.
- A suitable material description is necessary in order to obtain an accurate simulation of the deformation. In this case, elastic or hyperelastic properties need to be properly defined for each material.
- The reference state, loading forces and boundary conditions define the deformation of the model. Thus, the breast model is compressed by applying and solving the mechanical equations using the FE method.

Notice that, in most of the works, while the geometry is patient-specific, extracted from MRI images in this case, the material parameters used during the FE simulation are usually extracted from the literature (see Section 3.B.2). Furthermore, the definition of the loading forces and boundary conditions is related to the mathematical formulation of the problem for each particular work. The following sections describe common techniques and software used in this task

3.A. Geometry extraction

Geometry extraction is the first step in FE analysis, and it consists of obtaining the biomechanical 3D model of the breast. Since we use the MRI volume of the patient to obtain this model, we refer to a patient-specific biomechanical model. This phase consists of two different steps: segmentation and meshing.

Segmentation consists of dividing an image into regions to delineate the organs or differentiate the parts of the body. Notice that the segmentation strategy depends on the specific image acquisition process. For instance, cystic breast lesions, containing blood, appear bright on MR T1-weighted images and dark on MR T2-weighted images.[3] At the end of the segmentation step, all voxels of the MRI volume have been labeled according to a specific region, as depicted in Fig. 4, where labeled regions obtained from a T1 MR image are shown using different colors. The labeled regions represent either an organ or different tissues that will be subsequently used to build the FE model using a meshing step. In contrast to mechanical engineering where Computer Assisted Design (CAD) software allows the creation of smooth models that are easy to subdivide into nodes and elements, the irregular shapes of internal organs or body parts require a piecewise approximation of the shape. Consequently, the mesh construction is usually subdivided into two steps:

- Surface mesh construction, in which the outer shape of the object is discretized by 2D (triangular or square) elements; and
- Volume mesh construction, in which the space between the surface meshes is subdivided using 3D (tetrahedral or hexahedral) elements.

The following subsections describe the geometry extraction applied to breast biomechanical modeling.

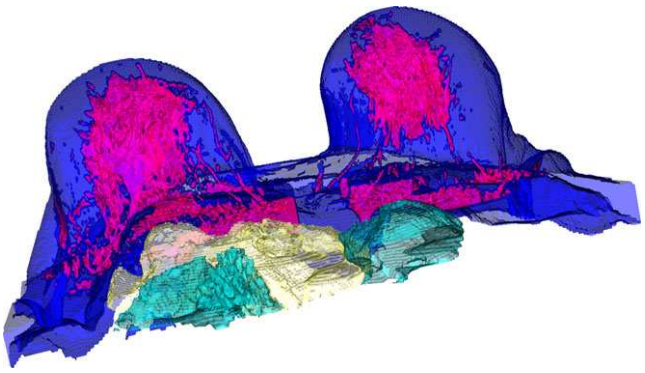

FIG. 4. Labeled regions from T1 precontrast MR image. The internal organs were delineated using a probabilistic atlas approach while a slicewise region growing algorithm was used to segment the background. The breast tissues were segmented using an expectation–maximization algorithm, obtaining: the adipose tissue in blue, the glandular tissue in purple, and the internal organs, such as the pectoral muscle, the heart, and the lungs, in dark blue, yellow, and green, respectively. The visualization was carried out using the software MeVisLab^{TM} (Section 6.D).

3.A.1. Segmentation

During the MRI acquisition, the patient lies in prone position with the breast hanging downward into a radio-frequency (RF) receiver coil. This coil measure the signal emitted from excited tissues. We will not discuss here the physics underling the process of forming a MR image. The tissue excitation, relaxation properties of the nuclei [T1, T2 or proton density (PD)], clinical protocols as well as the response to changes of the acquisition parameters [repetition time (TR), echo time (TE) among others] can be found in the specialized literature.[3] However, the importance of the acquisition and its effects in the segmentation strategy are well established.[38]

For breast and many other applications, such as head and spine, RF receiver coils are limited to receive signal only from tissues of interest. An ideal receiver coil for the breast should accommodate both breasts, the axilla and the chest wall. A critical step to obtain a patient-specific biomechanical model is to isolate the breast from the other parts of the body that appear in the MRI volume. For this task, the segmentation requires the identification of both the air–breast interface and the pectoral muscle. The first interface separates the air background and the breast region, while the pectoral muscle defines the boundary between the breast and the rest of the body. Furthermore, depending on the mechanical model used, internal tissues of the breast are sometimes also identified (being either adipose or glandular) and used in subsequent steps. In addition, the bias field is a common intensity inhomogeneity in breast MRI and may considerably affect the appearance of breast tissue. The bias field, which is specific for each MRI scanner,[3] yields a smooth variation in the intensity distribution of a tissue with respect to the spatial position, causing additional difficulty in discriminating the glandular tissue from other tissues and artifacts in breast MRI images. Several approaches have been proposed to correct the effect of the bias field in MRI images,[39] being the N3[40] and N4[41] algorithms the most common approaches.

In order to extract the air–breast interface, usually intensity-based algorithms, via thresholding,[42] and region-based algorithms[21,43] are used to remove the air background due to the homogeneity of pixel intensities in this region. Also, slicewise segmentation or combining multiple approaches, have been proposed. Hopp et al.[44] used a thresholding segmentation with morphological operations and active contours[45] to define the breast surface. Most of the related publications consider that the skin has little influence on breast compressions during the simulation.[46,47] However, the skin might be included in the biomechanical model as a 2D shell mesh or a 3D membrane (see Section 3.A.2). For instance, Solves-Llorens et al.[48] used a C-means algorithm to segment the skin voxels and compare the results obtained using both the 2D shell and 3D membrane. In contrast to the above studies, they conclude that the skin representation has a big influence in the simulation, and they found that the errors yielded when the 2D shell was used were larger than those when the 3D membrane was included in the simulation.

On the other hand, identifying the pectoral muscle boundary is a challenging task. Shape variations of the pectoral muscle and poor contrast between glandular and pectoral muscle have a large effect in the segmentation of this structure.[43] Thus, automatic algorithms for chest wall segmentation of the breast MRI are infrequent, and manual or interactive segmentation approaches are usually used during this step.[42] Edge-based algorithms have been tested in this task. Wu et al.[49] proposed a pectoral boundary detection based on a slicewise edge-enhance in sagittal MRI images while Giannini et al.[50] used the gradient characteristics of the pectoral muscle. Wang et al.[51] proposed a Hessian-based filter, using eigenvalues, to differentiate the specific geometrical structure of the chest wall. This algorithm was used by Solves-Llorens et al.[52] in order to perform a fully automatic MRI–mammography registration. Later, Wang et al.[53] extended their previous work to localize the air–breast boundary, obtaining a fully automatic whole breast segmentation. Atlas-based segmentation algorithms are also used in this task, showing a good performance, due to the prior knowledge of the anatomical structures. Ortiz and Martel[54] used a method based on 3D edge detection, combined also with a probabilistic atlas, to separate the breast volume. Gubern-Mérida et al.[55] automatically segmented the breast tissues and pectoral muscle by means of a probabilistic atlas which contained information of the pectoral muscle, lungs, heart, and thorax. This approach was also used by García et al.[56] in order to extract a patient-specific FE model of the breast to localize breast lesions between digital mammograms and MRI images.

Once the whole breast has been isolated, internal tissues (glandular and adipose but also tumors) can be segmented, depending on the requirements of the biomechanical model. Furthermore, breast density — i.e., the ratio between the whole breast volume and the glandular tissue volume — is an important risk factor, associated with the development of

breast cancer. Therefore, most of the proposed algorithms are focused on segmenting glandular tissue, instead of adipose tissue, of the breast. Moreover, due to the variability of amount, shape and patterns of glandular tissue, clustering- and intensity-based algorithms are frequently used to segment the tissue. Clustering-based algorithms, such as k-means and fuzzy c-means (FCM) have been widely used in this task.[48] Fuzzy approaches have been tested to evaluate the partial voxel effect from the membership of each voxel to each tissue class. Conversely, Pathmanathan et al.[42] used a 3D region-growing algorithm to maintain the spatial properties that classical clustering techniques do not consider. Similarly, Azar et al.[46] used a fuzzy connectedness algorithm. Intensity-based algorithms have been also used via a direct thresholding[21] or assuming that the intensity of each tissue voxel follows a probabilistic distribution, usually a Gaussian distribution. Gaussian mixture models can be fitted using an expectation–maximization (EM) algorithm, allowing the computation of the likelihood of each voxel to belong to both glandular and adipose tissues. However, because it is well known that the intensity distribution is not a perfect Gaussian distribution due to the partial volume effect,[57] some authors have proposed a spatial regularization scheme to reduce misclassified voxels. For instance, Eiben et al.[28] and Mertzanidou[58] used the EM algorithm in combination with Markov random field (MRF) regularization. An implementation of the EM algorithm and MRF regularization can be found in the Insight Toolkit (ITK) library or in the work developed at the University College London by Cardoso et al.,[59] available online under the name of *NiftySeg*.[187]

Commercial tools are also available to perform this segmentation step. Tanner et al.,[60,61] Carter et al.,[62] and Schnabel et al.,[29] among others, have used the commercial software ANALYZE^{TM} [Biomedical Imaging Resource (BIR), Mayo Clinic, Rochester, MN, USA]. This is a software package for the multidimensional displaying, processing, and measurement of multimodal biomedical imaging [MRI, computed tomography (CT), and positron emission tomography (PET)]. This software provides several segmentation and classification algorithms based on thresholding approaches. Additionally, ANALYZE^{TM} provides interactive tools to segment manually or iteratively, and it allows the extraction of the surface mesh from the segmented images.

Evaluating the accuracy of the segmentation requires a ground truth, which is obtained by expert radiologists delineating the MR images manually. The quantitative evaluation of a segmentation algorithm is obtained by using the Dice overlap coefficient,[63] Jaccard similarity coefficient,[64] false-negative fraction, and false-positive fraction errors. For instance, Gubern-Mérida et al.[65] reported a Dice coefficient of 0.94 for breast segmentation, 0.75 for pectoral muscle segmentation, and 0.80 for glandular tissue segmentation, using a fully automatic approach. However, segmentation alone cannot fully describe the biomechanical model shape. The spatial information needs to be addressed by means of a mathematical description. Usually, the breast surfaces are represented by parametric expressions, such as polynomial-based functions, or piecewise approximations, such as triangular meshes. The next section introduces the most common approaches.

3.A.2. Surface mesh construction

Once internal tissues of the breast have been segmented, the next step is to generate the anatomically realistic patient-specific FE model. Two different meshes are used to build the model: the surface mesh to define the external boundaries of the model and the volumetric mesh defining the internal behavior of the model. The first mesh, corresponding to the breast surface, is obtained from the borders of the breast (skin–air and breast–pectoral boundaries).

To obtain a smooth surface, high-order polygonal bases have been studied to parameterize the breast surfaces. For instance, Zhang et al.[66] defined the breast contour using a slicewise process. The border was described using a B-spline method to create smooth 2D contours and, finally, all contours were connected and merged into a 3D surface. Similarly, Chung et al.[67] and Rajagopal et al.,[68] used a semiautomatic method that parameterized the skin and muscle surface contours from the segmented MR images. The breast geometry was represented using a smoothly continuous tricubic Hermite polynomial-based function. Their method used a nonlinear least-squares approach to fit the surfaces of the volume elements to the segmented datasets. On the other hand, isosurface extraction can be used to fit the surfaces to data using piecewise linear interpolation algorithms, such as the marching cubes algorithm[69] or level sets,[70] to subdivide the surface into triangular facets. Schnabel et al.[29] and Mertzanidou et al.[71] used the standard marching cubes algorithm to extract the surface mesh, which is subsequently softened using a Laplacian smoothing algorithm.[72] This approach extracted a triangular mesh directly from the MR segmentation.

Due to volume mesh quality assumptions (notice that regular elements are preferred in order to obtain an accurate FE analysis) and Delaunay triangulation conditions,[73,74] the number of elements comprising the volumetric mesh is related to the number of elements composing the surface mesh. From a standard MRI, the number of voxels belonging to the breast surface is too large and it results with a large number of elements. To overcome this problem, the number of points on the surface is reduced either by reducing the surface mesh using a downsampling algorithm[29] or by reducing the image resolution before meshing.[71] In the former approach, after extracting the surface mesh from the MRI segmentation, a decimation algorithm, such as quadric[75] or clustering[76] decimation, is used to reduce the number of points forming the mesh. In the latter approach, the MRI volume is downsampled to large isotropic voxels, where the voxel size is defined by the desired number of elements in the volumetric mesh. However, none of both solutions is optimal. When downsampling the mesh, the Delaunay condition might be not satisfied, and the neighboring vertex degrees could be different depending on the node selected,

developing skinny triangles or other geometric irregularities on the surface. On the other hand, when downsampling the MRI, the partial volume effect is aggravated, disturbing the total volume and, even, the shape of the breast. Topological irregularities, such as skin folding, can occur during the MR acquisition and might be removed after resampling.

Implementations of the marching cubes algorithm and mesh decimation algorithms are provided, for instance, by the Visualization Toolkit (VTK) library. Improving the surface mesh quality, beyond only smoothing,[28], can be performed using several software platforms, such as *Meshlab* (Visual Computing Laboratory of ISTI-CNR, Italy). MeshLab allows the processing and editing of unstructured 3D triangular meshes. Among other functions, Meshlab provides tools to clean, edit, inspect, and render the meshes.

The accuracy of the biomechanical model representation, with respect to the original MRI segmentation, can be evaluated using metrics such as the root-mean-squared and Hausdorff[77] distances among others. These metrics aim to evaluate the gap between the surface mesh and the segmentation or the parametric surface previously obtained.[74] Rajagopal et al.,[78] Chung et al.,[79] and Lee et al.[21] report values between 0.5 and 1.5 mm, using the root-mean-square error to compute the distance between the FE mesh, composed of tricubic Hermite hexahedral elements, and the segmented breast surface.

3.A.3. Volume mesh construction

After extracting the surface mesh, the internal spatial information needs to be encoded using a volumetric mesh (Fig. 5). The volumetric mesh could be formed from a single material (homogeneous tissue) or, in contrast, by different materials (corresponding to different tissues). There are two different options to divide the volumetric mesh into different regions. In the first approach, the surface mesh corresponding to each tissue is computed and then the inner parts are joined into one volumetric mesh that can contain several disjointed regions.[84] In the second one, the elements are labeled *a posteriori*, once the volumetric mesh has been constructed as one single region, considering the voxels belonging to each class that are warped by the element.[85]

Pioneers in this field of study used eight-node hexahedral elements;[80,81] however, lately, four-node tetrahedral elements were preferred to compose the volumetric mesh.[28,44,71] Furthermore, Zhang et al.[66] used 10-node tetrahedral elements to increase the accuracy of the model for large deformations. The use of tetrahedral or hexahedral elements in the simulation of FE models is an open problem and topic of debate.[82] Each type of element has its own properties and advantages. Tetrahedral elements are widely used due to their geometrical flexibility and because they produce acceptable displacement behavior. However, hexahedral elements produce more accurate and more stable simulation results.[83]

Table I summarize different examples of meshes used in breast modeling, including the purpose of the work, the tissues modeled, and the type and number of elements. Notice that the number of elements that compose each mesh ranges from just a couple of dozens to over three hundred thousand elements. So far, no experimental studies have determined the optimal resolution of the volumetric mesh for this task. However, del Palomar et al.[84] demonstrated that a tetrahedral mesh needs to be fine enough to minimize numerical errors during the solver, using more than three hundred thousand elements in their experiments.[74]

Usually, 4-node tetrahedral meshes are extracted using the open-source package TetGen.[93] TetGen[188] is a type of software used to generate high quality tetrahedral meshes from 3D polyhedral domains, generating Delaunay tetrahedralizations and Voronoi partitions. Another option is to convert the segmented image directly to a 3D mesh avoiding the step in-between. For instance, to construct a hexahedral mesh, Pathmanathan et al.[42] used a voxel-based method, converting voxels or groups of voxels into elements. Hopp et al.[44] used the open-source package *iso2mesh*,[189] which is a Delaunay mesh generator widely used in biomechanical modeling. Developed by Fang and Boas,[85] this software uses a labeled image to construct a tetrahedral mesh and label each element depending on the corresponding tissue class. The surface is extracted and repaired using the CGAL[190] library, before using TetGen to create the final mesh. This toolbox is compatible with Matlab^{TM} or GNU Octave.

On the other hand, commercial software is also available to convert the segmented image to a FE mesh. The main advantage of using commercial software is the robustness regarding mesh quality, capability of importing these meshes into commercial FE software packages and the option of creating the surface and volume mesh as well as several types of elements. Hence, to construct the breast volume, Solves-Llorens et al.[48] used the commercial software ScanIP (Simpleware^{TM}, Bradninch Hall, Exeter, UK), which can create models that can be imported by any FE commercial tool, while del Palomar et al.[84] used the Harpoon mesh generator[191] (Sharc Ltd., Manchester, UK). Geometries can be imported from CAD systems and the software creates surfaces and volume meshes.

To evaluate the quality of the volume mesh, several quality metrics have been proposed depending on the type of the element. For instance, shape measures for triangular and tetrahedral elements, such as the aspect ratio, shape factor, radius ratio, or minimum solid angle, among others.[94] Hipwell et al.[88] and Tanner et al.[60] defined a minimum mesh quality, where elements exceeding an aspect ratio of 20 or an angle of 165° were kept to a minimum. The aspect ratio is defined as the ratio of the longest edge to the shortest normal dropped from a vertex to the opposite face, normalized with respect to the shortest normal dropped from a vertex to the opposite face of a perfect tetrahedral element. The aspect ratio of an ideal tetrahedral element is 1.0 while extremely large values $\gg$40 should be closely examined to determine where they exist and whether the stress results in those areas are of interest or not. Apart from tetrahedral elements, hexahedral, pentahedral, and pyramid elements are common in FE models.

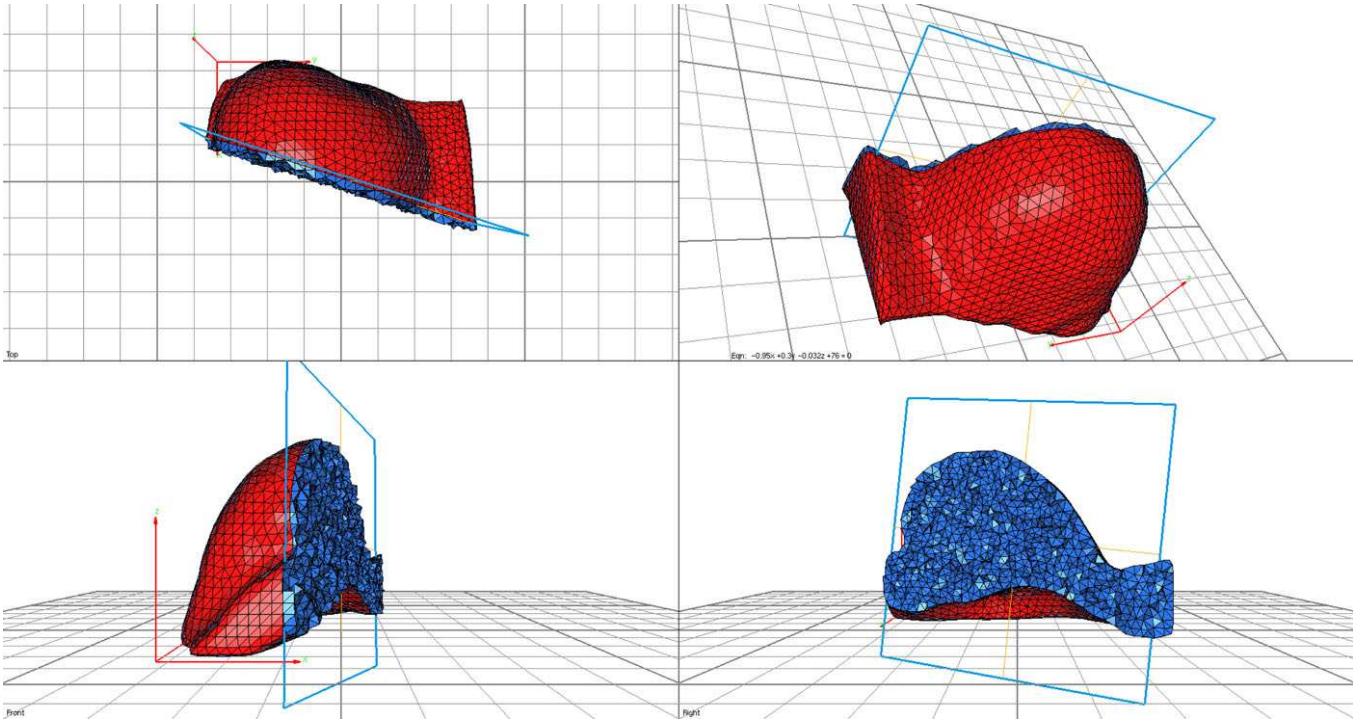

FIG. 5. Finite element biomechanical model of the right breast, composed of two tissues: skin (red), as a shell mesh composed of triangular elements, and one single internal material (blue), composed of tetrahedral elements. The surface mesh was extracted using a standard marching cube algorithm and smoothed by means of a Laplacian approach, the volumetric mesh was extracted using the open source package TetGen, and the visualization was carried out using the software Medit (See Section 6.D).

To evaluate the quality of these elements, the quality metrics exposed above can be extended to the particular geometry of each problem.[74]

3.B. Mechanical deformations

In the previous section, we have reviewed the process of building the mechanical patient-specific model using segmentation of the MRI and encoding the spatial information using surface and volumetric meshes. The next step is to deform the obtained model to reproduce the mammographic acquisition. This is performed using the FE analysis, which allows the simulation of large deformations (of the breast) in a physically realistic way.

3.B.1. Continuum mechanics

During mammographic acquisition, the breast is highly compressed. To simulate an accurate behavior of the biomechanical model of the breast, the stress–strain relationships must be known. Different approaches, such as classical linear elasticity,[29] nonlinear elasticity,[81] and pseudo-nonlinear elasticity[46] have been used by researchers for years. Furthermore, the experimental data available show both linear[95] and exponential[96] relationship between the tissue deformation applied (strain) and response (stress) of the breast tissues. An overview of the elastic and hyperelastic parameters, as well as physical behavior of breast tissues, reported in the literature is exposed in Section 3.B.2.

In this section, we will provide a brief overview of the physics that allows the simulation of the deformation of the breast, with special attention to the nonlinear formulation of the elasticity theory.[97] A comparison among the linear, nonlinear, and pseudo-nonlinear formulation in breast tissue modeling is provided by Whiteley et al.[98] Furthermore, we encourage the reader to review specialized books concerning solid mechanics simulations[99,100,101] and, more specifically, soft-tissue mechanics and breast tissue modeling[102,103,98] for further reference.

Kinematics: When a body is in equilibrium, the principle of the conservation of linear momentum states that the external forces are equal to the internal forces. To describe the motion of a body, subjected to applied loads, kinematic relations need to be defined. During deformation, the constitutive particles change their positions. The deformed state of the body and, therefore, the mechanical equations can be referred either to the initial, i.e., undeformed — configuration using a Lagrangian description, also called material description, or to the current, i.e., deformed — configuration using a Eulerian description, called spatial description. Deformation and stress measures can be defined using both configurations.

The relative spatial position of two neighboring particles after deformation, ∂x can be described in terms of their relative material position before the deformation, ∂X, by the deformation gradient tensor, F. Considering the displacements, the deformation gradient tensor is defined as:

TABLE I. Summary of the meshes used in breast modeling, detailing publications, simulation developed, type of tissues modeled, type of elements used as well as the number of elements and nodes.

Author	Application	Tissues	Elements	# Elements	# Nodes
Samani et al.[81]	Breast compression	Adipose, glandular	8-Node tetrahedrons	2–16 k	2–16 k
Azar et al.[80]	Breast compression	Adipose, glandular, and lesion	8-Node hexahedrons (trilinear isoparametric elements)	2,793	3,712
		Skin	3-Node triangular	2,394	–
Schnabel et al.[29]	3D–3D registration	Adipose, glandular, and tumor	10-Node tetrahedrons	40–120 k	30–90 k
		Skin	3-Node triangular	–	–
Pathamanathan et al.[86,42]	Breast compression	Adipose, glandular	8-Node hexahedrons (trilinear elements)	4.0–4.6 k	5.0–5.6 k
Ruiter et al.[47]	3D–2D registration	Adipose, glandular	8-Node hexahedrons	7^3	–
Carter et al.[87]	Prone-to-supine registration	Adipose, glandular	10-Node tetrahedrons	55,359	–
Hipwell et al.[88]	Breast compression	Adipose, glandular, and tumor	10-Node tetrahedrons	40–70 k	–
Zhang et al.[66]	3D–2D registration	Breast volume	10-Node tetrahedrons	9 k	13 k
Chung et al.[67]	Breast compression	Breast volume	8-Node hexahedrons (tricubic Hermite elements)	120	231
del Palomar et al.[84]	Gravity load	Adipose, glandular	4-Node tetrahedrons	313 k	61 k
		Skin	3-Node triangular	–	–
Tanner et al.[61,89]	Breast compression	Adipose, glandular	10-Node tetrahedrons	34–80 k	50–120 k
Rajagopal et al.[68]	Unloaded configuration	Breast volume	8-Node hexahedrons (tricubic Hermite elements)	24–112	70–216
Hsu et al.[90]	Breast compression (phantom generation)	Adipose, glandular and skin	4-Node tetrahedrons	131–719 k	–
Han et al.[91]	Breast compression	Adipose, glandular, and tumor	4-Node tetrahedrons	161,997	29,30
Lee et al.[21]	3D–2D registration	Breast volume	8-Node hexahedrons (tricubic Hermite elements)	96	–
Hopp et al.[92,44]	3D–2D registration	Breast volume	4-Node tetrahedrons	25 k	–
Mertzanidou et al.[71]	3D–2D registration	Breast volume	4-Node tetrahedrons	2,500	800
Solves-Llorens et al.[52]	3D–2D registration	Adipose, glandular	4-Node tetrahedrons	313 k	61 k
		Skin	3-Node triangular	–	–
García et al.[56]	3D–2D registration	Adipose, glandular	4-Node tetrahedrons	30–270 k	5–45 k

$$F = \frac{\partial x}{\partial X} \tag{1}$$

F can be used to determine the change in length and direction of a differential line element. Therefore, the determinant of the deformation gradient (the Jacobian, $J = det(F)$) defines the changes in volume of the element, and hence, volume changes can be expressed as:

$$\partial v = J \partial V \tag{2}$$

where ∂V is a volume element in the reference configuration and ∂v the corresponding form in the current configuration. Notice that the transformations of the material can be isochoric — i.e., volume-preserving ($J = 1$)- or nonisochoric.

To describe the body deformation Cauchy–Green tensors are often defined.[100] The right Cauchy–Green tensor is defined as the material scalar product — i.e., considering the reference configuration of the particles — of the deformation gradient tensor, $C = F^T F$, while the left Cauchy–Green tensor is defined as the spatial scalar product — i.e., considering the deformed configuration of the particles — of the deformation gradient tensor, $b = FF^T$ (being F^T the transposed of the deformation gradient tensor). Isochoric components are often expressed in terms of the principal invariants of the right Cauchy-Green.

Stress tensors: Additionally, stress is a measure of the amount of force per unit area acting on a body. The Cauchy

stress, $\sigma = \sigma_{ij}$, and the Kirchhoff stress, $\tau = \tau_{ij} = J\sigma_{ij}$, are two common stress measures, both of them defined in the deformed configuration. Regarding the reference configuration, the first Piola-Kirchhoff stress tensor, P, defined as the nominal stress, and the second Piola-Kirchhoff stress tensor, S, defined as the material stress are used to evaluate the amount of force acting on the body.[100]

Using a Lagrangian formulation is often more convenient, with the coordinates of the undeformed body as the independent variables and the coordinates of the deformed body as the dependent variables.[98] The relationship between the stress in the deformed and the undeformed configurations is defined as follows:

$$\tau = J\sigma = PF^T \tag{3a}$$

$$\tau = FSF^T \tag{3b}$$

Governing equations: The local equilibrium equations are derived considering three fundamental conservation principles in physics: conservation of mass, linear momentum, and angular momentum.

1. The conservation of mass principle requires that the mass of the body remains constant before and after the deformation. Therefore, the mass density in the deformed configuration, ρ, is related to the mass density in the initial configuration, ρ_0, considering Eq. (2) as follows:

$$\rho = J\rho_0 \tag{4}$$

2. The conservation of linear momentum exposes the local equilibrium equation and is obtained as a force balance. In the deformed configuration, it is expressed as follows:

$$\frac{\partial \sigma_{ij}}{\partial x_i} + \rho b_j = \rho \dot{v}_j \tag{5}$$

where b_j is the force per unit mass, ρ is the mass density, v_j represents the velocity of a given particle, and $\dot{v}_j$ the derivative of the velocity, i.e., the acceleration. Notice that summation convention is used in this equation regarding $i,j = 1,2,3$ that represent the coordinates of the system of reference. The equilibrium requirements may also be written in the reference configuration, using the corresponding relations between stress measures.[78,100]

3. The conservation of angular momentum requires that the applied moments need to be balanced in order that the total angular momentum of the system remains constant. This principle yields symmetry of stress measures, such as the Cauchy stress, $\sigma_{ij} = \sigma_{ji}$, and the second Piola–Kirchhoff tensor, $S_{ij} = S_{ji}$. However, notice that the first Piola–Kirchhoff stress tensor introduces an asymmetric behavior.

The formal definition of the problem requires to establish a set of suitable initial and boundary conditions. Initial conditions describe the state of the body at the beginning of the analysis and can be related to the kinematic state (considering the position and velocity at the initial time point) or the initial stress state for every point in the body. Regarding the boundary conditions, two types need to be considered, related to (a) the displacement (or restriction of movements) of a set of points, and (b) the traction of the points on a surface in the body.

Constitutive relations: The material behavior facing deformations is defined as either incompressible, when the material preserves its volume under arbitrary loads, or compressible, when its volume changes. Formally, the changes in the volume are explained by the Jacobian. A material is considered incompressible when the Jacobian is equal to one ($J = 1$). Furthermore, when a material is compressed in one direction, it tends to expand in the perpendicular direction to the compression. The Poisson's ratio (v) is defined as the coefficient of expansion on the transverse axial or negative ratio of the transverse to axial strain. The Poisson's ratio of an isotropic and linear elastic material cannot be less than -1.0 or greater than 0.5 due to Young's modulus (E), while the shear modulus, μ, and bulk modulus, κ, must be positive. The shear and bulk moduli are two measures for evaluating the stiffness of materials and are defined as follows:

$$\mu = \frac{E}{2(1+v)} \tag{6}$$

$$\kappa = \frac{E}{3(1-2v)} \tag{7}$$

A given material can be categorized according to its homogeneity and isotropy:

- Isotropic material, when its response to an applied deformation is invariant to the direction of the loading. This kind of material was used by del Palomar et al.,[84] Lee et al.,[21] and Hopp et al.[92] among others.
- Transversely isotropic material, when there is a preferred direction in the material in which its response varies with respect to the other directions when the deformation is applied. For instance, Mertzanidou et al.[71] used this material categorization to simulate the behavior of the Cooper's ligaments during the compression of the biomechanical breast model.
- Anisotropic material, when the material response is different depending on the loading in any direction. In breast model simulation, Hopp et al.[105] compared the behavior of isotropic and anisotropic materials applied to MRI-mammography registration, obtaining similar results.

The constitutive relations describe the behavior of the materials under a deformation. These relations are composed of a set of stress–train relationship equations. The simplest mechanical model follows Hooke's Law, in which the strain,

ε, is related to the internal stress, σ, using the Young's modulus of the material, E:

$$\sigma = E\epsilon \tag{8}$$

Hooke's Law defines the behavior of the material as linear and elastic. Currently, no method can measure the internal stress distribution *in vivo*,[106] although under certain assumptions, Young's modulus can be estimated. However, to simulate the behavior of human tissues, a linear approach is not enough.[107] In the case of hyperelastic materials, the behavior is expressed by the strain energy function, U. Furthermore, for an isotropic material, the strain energy function must be independent of rigid body rotations and the particular choice of coordinates and must, therefore, be a function only of the three invariants of the right Cauchy–Green tensor, C.

$$I_1 = trace(C) \tag{9a}$$

$$I_2 = \frac{1}{2}((trace(C))^2 - trace(C^2)) \tag{9b}$$

$$I_3 = det(C) = J^2 \tag{9c}$$

Using the strain energy function, U, the Cauchy stress and the second Piola–Kirchhoff stress tensor can be defined as follows:

$$\sigma = \frac{\partial U}{\partial \epsilon} \tag{10a}$$

$$S = 2\frac{\partial U}{\partial C} \tag{10b}$$

In soft-tissue modeling, several material definitions have been tested. The most common material models are:

- Neo-Hookean model:

$$U_{NH} = \frac{\mu}{2}(I_1 - 3 - 2\ln J) + \frac{\kappa}{2}(J-1)^2 \tag{11}$$

where μ and κ are the shear and bulk moduli, respectively, defined in Eqs. (6) and (7). Although it is the simplest, this model is the most commonly used to describe the hyperelastic behavior of breast tissues.

- Mooney–Rivlin model:

$$U_{MR} = \frac{\mu_1}{2}(I_1 - 3) + \frac{\mu_2}{2}(I_2 - 3) + \frac{\kappa}{2}(J-1)^2 \tag{12}$$

Notice that, in this case, for small deformations, the shear modulus is $\mu = \mu_1 + \mu_2$.

- Arruda–Boyce model:

$$U_{AB} = \frac{\kappa}{2}\left(\frac{J^2-1}{2} - \ln J\right) + \mu\sum_{i=1}^{5}\frac{C_i}{\lambda^{2(i-1)}}(I_1^2 - 3^i) \tag{13}$$

where λ is the locking stretch and C_i are constants equal to: $C_1 = 0.5$, $C_2 = 0.05$, $C_3 = 11/1050$, $C_4 = 19/7000$ and $C_5 = 519/673750$.

- Yeoh models:

$$U_Y = \sum_{i=1}^{n} A_i(\bar{I}_1 - 3)^i + \sum_{k=1}^{n} B_k(J-1)^{2k} \tag{14}$$

where A_i and B_k are material constants. When $n = 1$, the Yeoh model reduces to the neo-Hookean model for incompressible materials, being $A_1 = \frac{\mu}{2}$ and $B_1 = \frac{\kappa}{2}$.

3.B.2. Physical behavior

The elastic and hyperelastic properties of soft tissues have gained significant interest during past decades. Since healthy and unhealthy tissues have different elastic values, this property is important in medical applications such as diagnosis, treatment planing, or soft-tissue simulation. Consequently, to develop an accurate model of the breast, the elastic properties and stress–strain relationship of breast tissues need to be properly defined. The elastic properties of soft tissues depend on the microscopic and macroscopic structural organization of their molecules. Measuring these properties requires specific *a priori* assumptions about the tissue mechanical behavior. Because tissues are mainly composed of water, an usual assumption is to consider them as nearly incompressible,[107] thus implying a definition of the Poisson ratio close to $v = 0.5$.

There are different studies measuring that property per tissue. Earlier studies were performed ex-vivo. However, living tissue properties are not conserved ex vivo and it is also known that mechanical properties depend on the age of the tissue, the strain rate used to test the tissue and the strain range investigated. One of the first studies was performed by Krouskop et al.,[95] where the time between the ex vivo sample removal and the tests varied over a range from 25 to 120 minutes. The physical size of the tissue samples were considered and selected to assure that the assumptions about homogeneity and isotropy were held. Another study was conducted by Wellman,[96] who performed an ex vivo study in which the tissue samples were tested immediately after removal from the body. Wellman proposed an exponential stress–strain relationship for large deformations of breast tissues, similar to other biological tissues,[107] and it is one of the most used approaches in breast modeling. Figure 6 shows a representation of the stress–strain measured by Wellman, Krouskop, and by other authors. Notice that Krouskop et al.[95] found a linear strain–stress relationship for adipose tissue and an exponential relationship to describe the glandular tissue behavior. Azar[110] proposed a material model similar to Wellman; however, Azar corrected the relationship for adipose tissue to simulate the effects of Cooper's ligaments. Similarly, Samani et al.[81] used a hyperelastic neo-Hookean material model to approximate Wellman's stress–strain properties. Corrections used by Azar and Samani are presented in Table II, as well as the experimental results provided by other studies.

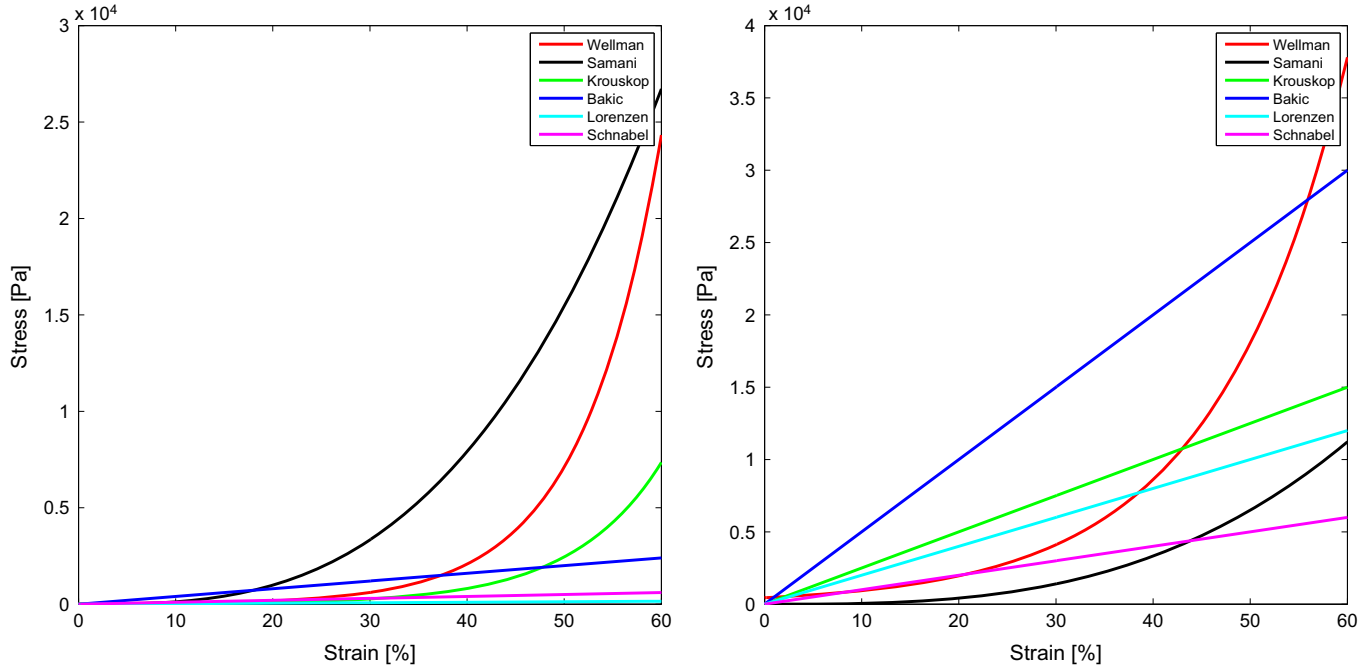

FIG. 6. Stress–strain relationship for glandular (left) and adipose (right) tissue, in the strain interval between 0 and 60%, used by several authors.[29,81,95,96,108,109]

On the other hand, *in vivo* experimental data are currently available. Shear wave elasticity imaging, sonoelastography, and magnetic resonance elastography have been used to measure the elastic parameters of living tissues.[106] Usually, in vivo experiments are carried out using small deformations or changing the loading conditions of the breast. Babarenda et al.[111] introduced a material parameter identification approach using several gravity-loading states. Del Palomar et al.[84] computed elastic values using computer tomography images both with the patient lying in the prone position and with the patient standing-up. Han et al.[91] used MR images of compressed (in the same way as the MRI-guide breast biopsy) and uncompressed breast. Finally, in these cases, the hyperelastic values were optimized using a FE simulation. Other authors, such as Bakic,[108] Lorenzen et al.[109] (both using linear stress–stress relationship), Tanner et al.[61] (linear,

TABLE II. Mechanical behavior of glandular and adipose tissues of the breast. This table shows the strain–stress approximation and material parameters provided in the literature. E represents the Young's modulus while ε corresponds to the strain. In order to acquire a complete representation, Section 3.B provides the constitutive relations which describe the behavior of the materials under deformation.

Reference	Constitutive model	Adipose	Glandular
Lorenzen et al.[109]	Linear	$E = 2\ kPa$	$E = 2.5\ kPa$
Krouskop et al.[95]	Linear	$E = 18 \pm 7\ kPa$ (at Strain = 5%)	
	Exponential		$E = 28 \pm 14\ kPa$ (at Strain = 5%)
Wellman[96]	Exponential	$E = 4.46\ kPa$ (at Strain = 0.0)	$E = 15.1\ kPa$ (at Strain = 0.0)
		$m = 7.4$	$m = 12.3$
Azar et al.[46]	Exponential	$E = \frac{E_{gland} - E(0)_{fat}}{\epsilon_{lim}} * \epsilon + E(0)_{fat}$ (if $\varepsilon < \varepsilon_{lim}$)[a]	$E = 15.1\ kPa$ (at Strain = 0.0)
		$E = 184\ kPa$ (if $\varepsilon \geq \varepsilon_{lim}$)	$m = 10$
Samani et al.-[81]	Polynomial	$E = 0.5197\varepsilon^2 + 0.0024\varepsilon + 0.0049$	$E = 123.8889\varepsilon^3 - 11.7667\varepsilon^2 + 0.6969\varepsilon + 0.0121$
Samani and Plewes[114]	Polynomial	$C_{10} = 0.31 \pm 0.03\ kPa$	$C_{10} = 0.33 \pm 0.04\ kPa$
		$C_{01} = 0.3 \pm 0.02\ kPa$	$C_{01} = 0.28 \pm 0.0\ kPa$
		$C_{11} = 2.25 \pm 0.3\ kPa$	$C_{11} = 4.49 \pm 0.8\ kPa$
		$C_{20} = 3.8 \pm 0.6\ kPa$	$C_{20} = 7.7 \pm 1.1\ kPa$
		$C_{02} = 4.7 \pm 0.7\ kPa$	$C_{02} = 9.45 \pm 1.3\ kPa$
Rajagopal et al.[112]	Neo-Hookean	$C_{10} = 0.08\ kPa$	$C_{10} = 0.15\ kPa$
del Palomar et al.[84]	Neo-Hookean	$C_{10} = 3\ kPa$	$C_{10} = 12\ kPa$

[a] $E(0)_{gland}$ and $E(0)_{fat}$ are the values fitted by Wellman[96] at Strain = 0.0. ε_{lim} correspond to the limit $\varepsilon_{lim} = 25\%$

neo-Hookean, and polynomial behavior), Rajagopal et al.[112], and Lapuebla-Ferri et al.[113] (both using neo-Hookean), have also proposed empirical elastic property values for breast tissue simulations.

In addition to the fatty and dense tissues, there are other structures in the breast that can affect the final simulation, such as the skin, abnormal tissue, Cooper's ligaments, and vessels and lymphatic nodes. The elastic properties of human skin are available in the bibliography. Authors such as Reishner et al.,[115] Edwards et al.[116], Groves et al.[117], Bischoff et al.,[118] or Mahmud et al.[119], among others, have measured the elastic and hyperelastic parameters of the skin. Non-healthy tissue data is also available. Wellman[96] and O'Hagan and Samani[120,121] measured the elastic and hyperelastic properties of fat necrosis, fibroadenoma, ductal carcinoma and other breast diseases. In general, the stiffness of unhealthy tissues is until 20 times the one of the healthy adipose tissue.[96] In these studies, experimental data were fitted to hyperelastic models, such as Yeoh, Ogden, Arruda-Boyce, or polynomial models. However, these models have not been used to evaluate the glandular or adipose tissue behavior. Detecting Cooper's ligaments in MR images is not possible. Thus, some researchers have modeled their effects in the physical behavior of the breast using indirect ways, for instance, assuming linear transverse isotropic material models[71] or defining explicitly the ligaments as binding conditions.[122] Finally, vessels and lymphatic nodes are not modeled due to their tiny contribution to the mechanical behavior. This typically also occurs with the skin. Although the influence of the skin on breast deformation is small,[46,61] some works include it as a shell mesh that wraps the volumetric breast mesh.

3.B.3. Loading forces and boundary conditions

A realistic biomechanical model of the breast requires accurate knowledge about the internal and external forces of the body. The previous section has focused on the internal properties of the breast model. In this section, we describe the loading forces and boundary conditions, both of which have a large influence on the behavior of the model.[61] We differentiate between two stages: computing the unloaded reference state and establishing the boundary conditions for the compression.

Unloaded reference state: The first step is to determine a correct starting loading condition, which is known as the unloaded reference state.[123] During the MRI acquisition, the woman lies in the prone position; however, during the mammographic acquisition, the patient stands up in front of the mammograph. Hence, the direction of the gravity in the patient's body is different for the two image modalities. Therefore, the natural state of the model will be the unloaded configuration, before being deformed by any force, including gravity. Although this defines a physically unreal state, the unloaded configuration is useful, or even necessary, to establish an initial stress state in mechanical simulations. Several approaches have been proposed to compute the unloaded configuration. The methodology can be divided into three big groups: (a) the simplest method, which consist in the inversion of the gravity, (b) iterative methods, and (c) inverse FEs approaches.[124]

The inversion of the gravity without consideration of prestresses was used by Lee et al.[21] during the multimodal MRI–mammography registration. However, just reversing the gravity effect is not enough to obtain the unloaded reference state.[68] Thus, Rajagopal et al.[123] introduced a numerical method to compute the reference state using a Lagrangian formulation — i.e., the undeformed FE configuration. The estimated undeformed state is perturbed and residual forces are evaluated until convergence. Similarly, Pathmanathan et al.[42,86] computed the unloaded state from the prone model as the reference position to perform the mammographic simulation to predict the tumor location during the deformation.

Carter et al.[62] introduced an iterative FE methodology where the reference state is computed assuming an internal stress equal to zero, applying gravity in the anterior direction. Subsequently, the gravity is again considered. The model is iteratively deformed to match the supine model up to a predefined threshold. This method was later extended by Eiben et al.,[28] inverting the gravity and relaxing the stresses of the breast model. Then, as in the previous case, the iterative process apply gravity and the unloaded configuration is updated. These techniques have been validated using phantoms[28,125] and neutral buoyancy studies, immersing the patient breast into water while the woman is lying in prone position.[126]

Finally, inverse FEs approaches were considered. Eiben et al.[124] tested the approach proposed by Govindjee and Mihalic[127] to obtain the patient-specific unloaded configuration of breast models. The method consists in reparameterizing the equilibrium equation, using a numerical approach to solve the inverse motion. The results were compared to that obtained using the simple inversion of gravity and the inverse finite deformation previously exposed,[28] showing that the iterative and the inverse methodology produce similar zero-gravity estimates, whereas the inversion of gravity is only appropriate for small or highly constrained deformations. Lately, Vavourakis et al.[128] proposed an inverse FE formulation to predict the unloaded state of soft tissues. The method is based on a Eulerian — i.e., current FE configuration- displacement/pressure formulation.

Breast compression simulation: Once the model is in the unloaded reference state, the mammographic acquisition is reproduced. However, boundary conditions are necessary to restrict the movement of the surface corresponding to the breast–body interface. From an anatomical point of view, the breast is not rigidly fixed to the body, it sits on the thorax and is joined by connective tissue, allowing the breast to slightly slide along the thorax. During the mammographic acquisition, the paddles do not compress the breast sufficiently to perform the displacement of the breast with respect to the thorax. Consequently, several assumptions need to be

considered. Zhang et al.[66] used the full constraint of the movement, meaning that nodes belonging to the breast–thorax interface are fixed. By contrast, Chung[79] allowed these nodes to slide along the surface using frictionless contact mechanics constraints. Similarly, Mertzanidou et al.[71] allowed the nodes to slide in the parallel direction of the compression paddle displacement.

Breast deformation can be modeled by solving the motion equations using two different types of boundary conditions, regarding either displacement (Dirichlet conditions) or force (Neumann conditions). Usually, the available data that are acquired during the mammographic compression or computational requirements restrict the option of using one or the other during the multimodal registration process. For instance, digital mammography allows to record compression magnitudes such as breast thickness or the force applied by the compression paddles, because protocols for the quality control of mammography are based on the applied force[9] and, sometimes, on the pressure.[129] Therefore, during mammographic compression simulation, applying Neumann conditions becomes a challenging task to define the force applied at each node, and most of studies reproduce the compression applying the Dirichlet condition.[66]

The simulation of breast compression has been studied independently from MRI to mammography registration.[67] Mainly, breast compression can be modeled following two approaches: nodes on the surface of the biomechanical model are directly subjected to displacements, emulating the effects of the compression paddles[110] or the breast compression is modeled as a dynamic contact problem using explicitly defined compression plates.[79] In the first case, the compression plates are not defined, and the nodes on the breast surface are controlled using direct displacements.[61,110] These displacements are applied as boundary conditions during the simulation. However, this method does not reflect a physically realistic deformation of the breast and leads to artifacts in areas closer to where the displacements are applied. In the second case, to define explicitly the compression plates, they are simulated only using a parametric surface[58,67] or as rigid bodies.[12] This second approach is more common when the FE solver is a commercial tool.

The contact problem can be solved using friction or frictionless contact, the latter being the most common approach.[71] The main reason is that the friction coefficient between the paddles and the breast is unknown. However, Hopp et al.[44] modeled the contact problem assuming a high friction. This feature allows only small relative sliding between neighboring nodes on both surfaces. Zhang et al.[66] constrained the movement of the nodes in contact with the compression paddle, allowing them to move only in the direction of the compression and avoiding sliding movements in the transverse direction. The main advantage in these approaches is that just the initial and final positions of the compression paddles are needed to simulate the deformation.[67] However, the contact problems can cause numerical difficulties and instabilities during the FE optimization. Small imperfections on the breast surface, such as skin folding, can make it difficult to reach a numerical solution. Furthermore, situating the plates with respect to the pectoral muscle is still an open problem.

3.B.4. Finite element solvers

Commercial and open-source FE packages can be used to solve the equations introduced previously (Section 3.B). Usually, commercial software provide complete FEs tools that allow the FE analysis, pre- and post-processing and visualization. The most common commercial software packages used for this task are ABAQUS^{TM} and ANSYS^{TM}. ABAQUS[192] (SIMULIA, Dassault Systèmes, Providence, RI, USA) is a popular commercial product used by researchers because of its multiphysics capabilities (mechanic, acoustic, or piezoelectric among others). To simulate breast mechanical deformations, ABAQUS has been used by Hopp et al.[11] and Azar et al.,[80] among others. On the other hand, ANSYS[193] (Cannonsburg, PA, USA) is a commercial FE solver. The mechanical toolbox includes support for linear, nonlinear, and dynamic studies. ANSYS^{TM} has been used by Qiu et al.,[22] Solves-Llorens et al.[48] and Hipwell et al.,[88] to simulate the breast model compression.

Regarding open-source FE packages, universities, groups, and research institutes have developed their own FE tools and, sometimes, they release the software to be used by interested parties. These software packages are usually designed to solve a specific problem. For instance, the Bioengineering Institute from the University of Auckland and University College of London have developed OpenCMISS and NiftySim, respectively, which are specific tools dedicated to soft-tissue simulation. OpenCMISS,[194] Open Continuum Mechanics, Imaging, Signal processing and System identification (Wellcome Trust) has been used to simulate mechanical deformations of the breast for years.[21,67,86] During the work performed by Rajagopal,[78] OpenCMISS was validated using ABAQUS^{TM}. NiftySim[195] is an open-source software package, available online. This software uses GPU implementation to solve the total Lagrangian explicit dynamic (TLED) FE formulation to define the soft-tissue behavior. Eiben et al.[28] and Mertzanidou et al.[71] have used NiftySim to simulate breast deformations. This software was validated against ABAQUS^{TM} in the work developed by Han et al.,[91] providing the same accuracy for deformation prediction but requiring much less computation time.

4. MRI TO X-RAY MAMMOGRAPHY REGISTRATION

Once the biomechanical model is compressed, mimicking the mammographic acquisition, the internal tissues of the breast needs to be projected into the 2D image, which sometimes is referred to as pseudo-mammogram. However, due to inherent errors in the previous steps, the pseudo-mammogram can differ from the mammogram, and a transformation is needed to obtain a more similar image. This transformation, called registration, allows to better replicate the

acquisition parameters. Following subsections describes these steps in detail.

4.A. 2D projection of the 3D model

Synthesizing mammographic images from other types of data, such as breast phantoms or other image modalities, requires a physics-based simulation approach. This procedure simulates the x-ray beam, where each ray traversing the breast computes the attenuation of glandular and adipose tissue at each pixel (i.e., detector) position. In these cases, several image acquisition parameters (input energy spectrum), detailed information of materials and geometry (compression paddle, antiscatter grid, detector performance), and other physical phenomena (scattered radiation, focal spot blurring) are required.[130]

To produce a realistic synthetic mammogram, the original 3D image is deformed using the deformation field computed from the biomechanical model. This is a common approach to obtain a voxelized breast phantom.[47] Also, polygonal mesh phantoms are described in the literature,[90,131] where the isosurfaces are extracted in the original image and reconstructed using the compressed model. Afterwards, the projection of the 3D biomechanical model to the 2D synthetic mammographic image is performed using a ray-casting algorithm. The intensity value for each pixel in the simulated mammograms is computed using the Beer–Lambert Law and the appropriate attenuation coefficients. X-ray spectrum data, tissue attenuation coefficients, and other mandatory information to generate a realistic synthetic mammogram can be found in the National Institute of Standards and Technology (NIST) database.[196] A realistic image synthesis requires physics-based simulations, usually related to complex approaches with a high computational cost, such as Monte Carlo methods.[132]

However, during the 3D–2D intensity-based registration, simpler approaches can be used. First, anode and filter materials, as well as the end point energy, for each synthetic image can be extracted from the DICOM tag header of the original x-ray mammogram. Hence, the synthetic mammogram can be simulated just using the transmitted primary x-ray.[21] without considering other physical phenomena. Also, monoenergetic approaches,[21] instead of polyenergetic spectrum, can be considered, computing previously the effective attenuation coefficient for the particular monoenergetic beam, and reducing the computational cost of the simulation.

Other authors have proposed techniques to generate synthetic CT images from MRI data.[133] Conversely to MRI, CT voxel intensities are related to the x-ray linear attenuation coefficients by means of the Hounsfield units,[197] and, therefore, a digitally reconstructed radiograph (DRR) can be synthesized using typical approaches.[134,135] A similar methodology is proposed by Mertzanidou et al.[136] This methodology was later extended, using a biomechanical model to simulate the breast compression.[71] To avoid resampling the 3D volume and then exposing the compressed breast image to the simulated x-ray beam, Mertzanidou et al.[71] used a transformation that undoes the compression, localizing each sampled point along the ray in its corresponding position in the MR image.

Finally, notice that feature-based registration methods do not require synthesizing detailed 2D projections. The internal landmarks can be localized within the compressed biomechanical model and directly projected within the 2D mammographic space.

4.B. Image registration

There is a consensus in the literature that a transformation of the obtained image is needed to compensate the inherent errors obtained due to patient positioning and deformation.[137–140] This transformation is called registration, and describes the process of establishing the spatial correspondence between the 3D MRI volume and the 2D simulated mammogram. Mainly, this task allows the colocalization of tumors, microcalcifications, and suspicious lesions in the two modalities.

The first attempt to perform the MRI to x-ray mammography registration process, emulating a physically realistic compression of the breast using FEM, was carried out by Ruiter et al.[47] Previously, several approaches to register MRI and x-ray mammograms were introduced. Muller et al.[141] used a nonlinear scaling algorithm to compute the specific projection angle of every projection and register mammograms to MR images. Behrenbruch et al.[142] used the breast boundary and internal landmarks to register mammograms. They applied the registration when one lesion was visible in both modalities and included the lesion as a salient structure in the landmark detection process. Marti et al.[143] used internal landmarks, evaluating the probability of finding a projection angle. On the other hand, Kita et al.[144] used epipolar line curves to compute the lesion location in the 3D MRI space from 2D mammograms. However, all of these approaches use a direct projection of uncompressed breast MR images and, therefore, the deformation of internal tissues were not considered.

Ruiter et al.[47] described the breast as composing by one single tissue material, using a nearly incompressible, homogeneous and isotropic neo-Hookean model, meanwhile the skin was modeled as being linear elastic with the material parameters determined by Bakic.[108] Finally, the deformation process was formulated by applying loads at certain nodes. The registration was performed in two steps. In the first step, the plate compression was applied; in the second step, the shape of the deformed breast and circumference of the corresponding mammogram were used to estimate the 3D shape of the breast. The boundary conditions of the simulation were formulated as the displacement between the undeformed and deformed surfaces of the estimated 3D shape. The final result was that the MR projection had the same circumference as that of the mammogram. This approach was later extended by Hopp et al.[92], including the rotation of the breast about the anterior–posterior axis. Solves-Llorens et al.[52] used a two-step approach, simulating the compression only once and

both, real and simulated mammograms, were registered using a B-spline registration. Similarly, García et al.[145] used rigid, affine and B-Spline registration, as well as the Demons algorithm[146] to compare the local breast density.

In a different approach, Zhang et al.[66] used a feature-based registration between MRI and x-ray mammograms to obtain a correlation between CC and MLO projections. Soft tissues were modeled as isotropic, linear, and homogeneous. To improve the registration between both modalities, a initial global shape calibration was used. The compression parameter was optimized until the silhouette of the biomechanical model overlapped with the silhouette of the mammogram. The registration was performed compressing the biomechanical model, using the calibrated compression parameter, and identifying any feature point, for instance calcifications, on CC and MLO views. On the other hand, Lee et al.[21] used an isotropic, homogeneous, and incompressible neo-Hookean material to define the breast model. In this case, the unloaded state was computed, removing the effect of gravity on the prone configuration. The breast model was allowed to slide over the surface of the ribs, using contact constraints, to mimic the loose attachment via Cooper ligaments. The registration consisted of maximizing the normalized cross-correlation (NCC) between the real mammogram and simulated one. Again, the problem was limited to a 2D registration. After obtaining a proper position of the compression plates, a rigid registration approach was used to align both mammograms.

The first 3D–2D intensity-based registration approach was introduced by Hopp et al.[44] This approach optimized several parameters, such as position and orientation of the patient, to adapt the registration process to the patient-specific conditions. The intensity-based optimization of the parameters was computed using the normalized mutual information (NMI) similarity measure. Mertzanidou et al. evaluated different MRI–mammography registration approaches, some of them involved using a patient-specific model while others referred to affine[136] or statistical deformation models.[147] With the obtained conclusions, Mertzanidou et al.[71] introduced a new intensity-based registration method, using NCC to evaluate the similarity between both the real and the simulated mammograms, and including the elastic parameters of the mechanical model and the amount of compression as the features to optimize. In this case, they used a transversely isotropic material model to consider the reinforcement of the biomechanical properties from fiber-like connective tissue in a given direction. The stiffness anisotropy ratio and the Poisson's ratio were allowed to change. In previous approaches, the material was described as incompressible ($\nu \approx 0.5$). However, Hopp et al.[44] exposed that an optimum Poisson ratio was $\nu = 0.3$, while Han et al.[91] established this measure higher than $\nu = 0.45$. Moreover, Hopp et al.[105] introduced the paddle position as a new feature for optimization during an MRI–mammography registration process. Recently, García et al.[56] also included an unrestricted rotation of the model around its principal axis. Furthermore, the Young's modulus of both, glandular and adipose tissue, were independently considered during the optimization.

5. EVALUATION METHODS AND CLINICAL APPLICATIONS

Quantitative evaluation of the registration between the MRI and mammogram is not an easy task. The common solution is to use some key characteristic between both image modalities that in breast image analysis is reduced to the localization of masses, since microcalcifications are hardly visible in MRI. The common procedure for localizing the mass in clinical practice consists in the use of contrast agents to enhance the lesion(s). Due to this contrast agent, during the MRI acquisition, the intensity of the lesion voxels in the MRI volume varies along the time. However, even with that contrast, checking the MR images to localize the suspicious regions is a slow task. Thus, several methods are used to reduce the time expended. For instance, under a set of quality assumptions, such as avoiding or removing chemical and motion artifacts, the lesion diagnosis is performed using the maximum intensity projection (MIP) of the subtraction image between a time point during the dynamic contrast enhancement and the precontrast acquisition. Figure 7 shows the MIP image of a patient. Notice that the contrast agent enhances several structures such as the blood vessels as well as two small lesions that can be appreciated in the center of the left breast. Although, nowadays, this procedure is manually performed, there is an increased interest in computer-aided diagnosis methods for breast MRI.[148–150] These algorithms can help radiologists to accelerate the analysis of MR images.

Once we have the MRI volume and the mammogram registered, the lesion that is localized within the MRI can be projected into the 2D image (mammographic space). Hence, the closer the real and the projected lesions, the better the registration. The common measure in the literature to evaluate this distance has been the target error registration (TRE), which is defined as the 2D distance between the centroid of both the real and projected lesions. Table III reports the results reported by previous methods. Notice that there is not a standard database to evaluate the proposed methods and, therefore, one should be cautious in the comparison of the results. Besides the inherent differences in the data, the experts' inter- and intra-observer variability, as well as the accuracy of the annotation process, may affect the results of the registration. Other features have been also considered for evaluation, like the overlap coefficient between the real lesion and the projected one[21,44] or the surface distance between both lesions.[21]

On the other hand, the use of multimodal breast phantoms allows to evaluate the algorithms in a controlled environment. Lee et al.[21] used the Tripe Modality Biopsy Training Phantom, model 051 (Computerized Imaging Reference System;[198], Norfolk, VA, USA) to evaluate their work. The phantom mimics the shape and properties of a human breast and can be used in MRI, mammography, and ultrasound acquisitions. This phantom contains 12 inclusions — i.e., lesions — with diameters ranging from 3 to 10 mm, clearly visible in all the modalities and simulating dense and cystic masses. Although being a simpler approach than using real

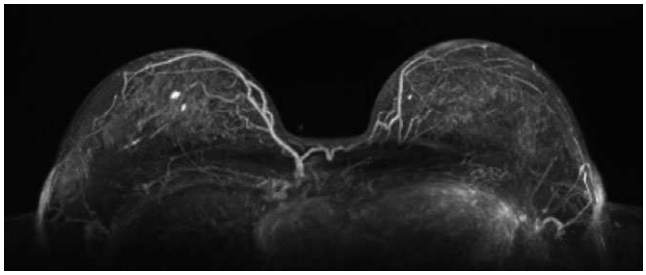

FIG. 7. Maximum intensity projection from a MR image. The T1-weighted acquisition was performed using a gadolinium-based agent. The last 3D image was subtracted to the initial precontrast 3D image and the maximum intensity pixel values were projected in the superior–inferior direction using MeVisLab^{TM}.

data, the use of phantoms may allow establishing an idealized ground-truth for the registration evaluation.

An example of a result of a registration between MRI and mammograms is presented in Fig. 8. The figure shows the location of both the real (in red) and computed (green) lesions in the mammograms. The methodology is widely exposed in our previous work.[56,152] In this particular case, the biomechanical model is composed of 78098 tetrahedral elements. The stress–strain relationship of the biomechanical model is approximated by a nearly incompressible, isotropic, and hyperelastic neo-Hookean model for both glandular and addipose tissue using the Young's modulus measured by Wellman.[96] The compression details to reproduce the mammographic acquisition are extracted from the DICOM header of the corresponding full-field digital mammogram and optimize using a simulated annealing algorithm.[153]

In the clinical practice, the suspicious lesion is firstly localized in the mammogram, while the MRI is used (if used) to confirm or reject the hypothesis of malignancy. Analyzing the 2D mammograms is faster than checking the 3D MRI volumes. In x-ray mammography, lesions are brighter than the glandular tissue. However, few papers provide the 3D geometrical information of the suspicious lesion in the MR image when they are located in the mammograms. Qiu et al.[22,154] used a 3D FE model to register temporal mammograms. The process consisted of compressing the mechanical model and aligning it with the corresponding mammographic view (CC or MLO). A back-projection ray-casting algorithm was applied, and the elements traversed by the ray could be labeled. The compressed model was restored to the reference state, and the straight line became a 3D curve in the initial model. When both CC and MLO projections were available, the 3D lesion was localized, finding the minimum distance between both 3D curves. Similarly, Hopp et al.[92] described this approach to localize lesions within MR images using a patient-specific model. In a different way, Solves-Llorens et al.[52] used the tetrahedrons that composed the model to localize lesions before and after compression, as well as between the mammographic and MR images. Finally, García et al.[56] proposed an efficient algorithm to compute the 3D position of a lesion in the MRI using an uniform grid[155] to store the elements of the biomechanical model. A backprojection of the lesion is performed from the mammogram to the compressed model, and the ray is simultaneously localized in the uncompressed model and, therefore, in the MRI. Moreover, this approach performed also a search space reduction to fast localize the intersection of the rays coming from the CC and MLO mammograms.

Not only the lesions presented in the breast can be used to evaluate the registration. In some clinical procedures, external landmarks are placed inside the breast and if they are visible in both modalities can be used to evaluate the registration. Figure 9 shows a mammogram and a MRI of a patient containing one small metallic clip which is used for image-guided biopsy procedures. In the mammographic views, the clip is clearly visible as a small bright spot, while in the MRI, it yield a paramagnetic artifact which is visually seen as a small black bubble.[156] This type of external landmarks was

TABLE III. Reported results for breast MRI and x-ray mammography registration using patient-specific biomechanical models of the breast. The error value corresponds to distance between the centers of masses of the lesion observed in the mammogram and the projected lesion from the MR volume. Notice that there is not a standard database to evaluate the proposed methods and, therefore, one should be cautious in the comparison of the results.

Reference	No. cases	Projection	Mean error value (mm)
Ruiter et al.[47]	6	CC	4.3
Lee et al.[21]	5	CC	16.42 ± 8.9
	4	MLO	16.65 ± 10
Hopp et al.[44]	79	CC	13.2
Solves-Llorens et al.[52]	14	CC	4.2 ± 1.9
	14	MLO	4.8 ± 1.3
Mertzanidou et al.[151]	5	CC	7.6 ± 2.4
	5	MLO	10.2 ± 2.3
Mertzanidou et al.[71]	10	CC	11.6 ± 3.8
	10	MLO	11 ± 5.4
García et al.[56]	10	CC	9.89 ± 3.72
	10	MLO	8.04 ± 4.68

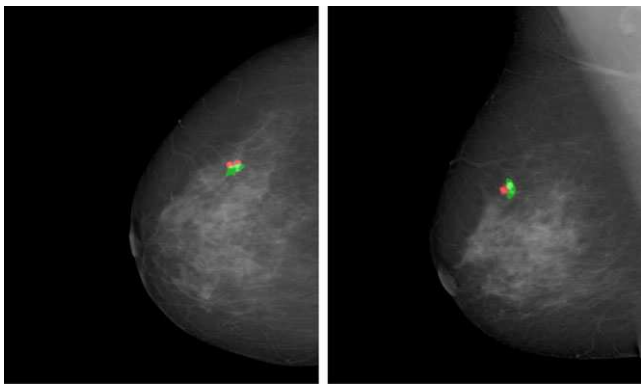

FIG. 8. CC and MLO mammograms of the same breast. The red area corresponds to the suspicious regions in the mammograms, while the green area represents the location of the MRI lesion, once the registration has been performed.

used by Mertzanidou[58] to evaluate the temporal and ipsilateral mammographic registration, two other possible applications of using a patient-specific biomechanical model in the clinical practice. The ipsilateral registration consists in correlating the internal breast structures between the CC and MLO projections while the temporal registration[22] allows to detect the change of the breast tissues between two (or more) time points. Using the same biomechanical model, two different mammograms are correlated, helping radiologists to evaluate susceptible areas. Furthermore, a computer-assisted diagnosis system can also be improved using multimodal features to classify the lesions[23] or using the capabilities of the biomechanical model to track tumors in image-guide procedures.[87]

However, so far, the application of these algorithms is not available in the clinical practice. Several works demonstrate that a multimodal combination leads to a more accurate diagnosis and treatment of the breast diseases from a medical point of view.[7] However, the lack of commercial tools to correlate the different image modalities, such as MRI and mammography, avoids analyzing the clinical benefits of combining these modalities and how it affects the clinical decision. Even when the trend seems to be to provide the radiologist with multimodal workstations, the vendor machines skip those approaches that involves long computational times. In the current problem, the use of the biomechanical model and the FE simulation require a long computational time in a conventional workstation (the time values reported in the literature are around 2 h for one single registration). These values are excessive in the clinical practice. Even when these approaches may be useful for clinicians and radiologists, these packages are only available from a research point of view.

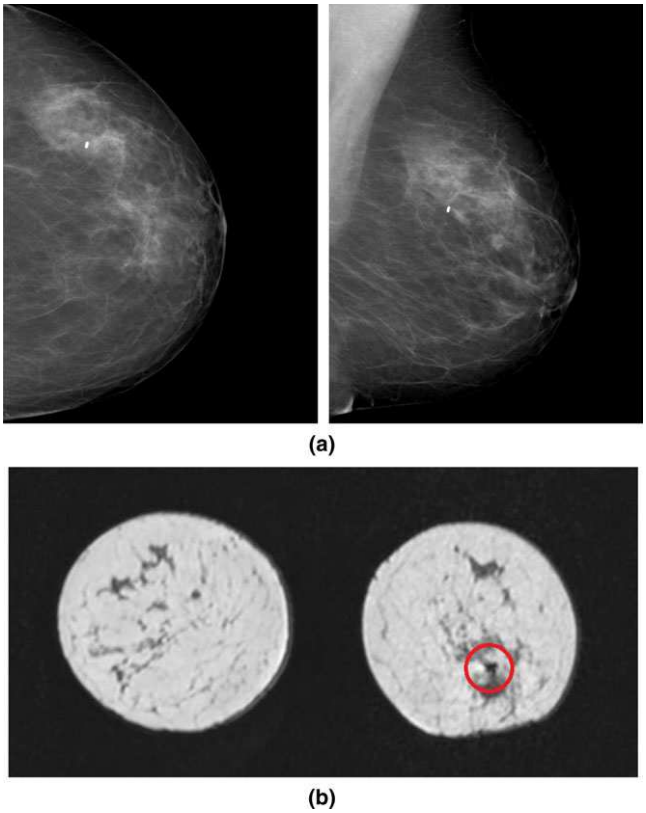

FIG. 9. Metallic clip for image-guide biopsy. The clip is visible in (a) CC and MLO mammograms as a bright spot, while (b) in MRI it yields a dark bubble.

6. DISCUSSION AND FUTURE TRENDS

During the MRI to x-ray mammogram registration, several processes are involved to yield the spatial correlation between both modalities. What makes a difference with respect to other 3D–2D registration algorithms is that the breast is highly deformed during the mammographic acquisition. Hence, the MRI to x-ray mammography registration is, *per se*, a local deformable process that involves the optimization of a high number of parameters.[66] Such a complex process requires highly accurate solutions at each stage of the problem, beginning with image preprocessing and segmentation, followed by 3D mesh model generation and compression using FEM. Finally, the 3D to 2D projection and registration. In next subsections, we explore new trends and software that can be used for these tasks.

6.A. Geometry extraction

The preprocessing of MR images, including bias-field correction and image intensity normalization, as well as tissue segmentation, are widely studied fields. In this document, we have exposed some algorithms previously used in this task, with special emphasis in those used in the multimodal MRI–mammography registration. These methods include automatic pectoral muscle[55,49] and whole breast[53] segmentation algorithms, and breast tissue segmentation by means of clustering-,[48] intensity-based,[21] or those that preserve the spatial information.[71] However, new algorithms are still appearing such as the ones based on deep-learning.[157,158] Similarly, image-to-mesh methods[159] are gaining interest to obtain more accurate biomechanical models. Several mesh generation methods have been introduced in other contexts to convert medical images into hexahedral[160,161] or tetrahedral meshes.[162–164] However, few of these approaches are open-source code or free software available to the general community.

Image processing and segmentation software used in other biomechanical modeling topics may be explored. The ITK libraries have become the reference software for image processing and registration. VTK libraries may be used, in combination with ITK, not only as a visualization tool but also as a simple library to extract surface meshes from medical images. Furthermore, some specialized software, derived from those libraries, may be suitable for these applications. This is the case of ITK-SNAP,[199] a software application used to segment structures in 3D medical images. Other complementary software is also available, such as Seg3D.[165] Seg3D is a volume segmentation and processing tool, that combines the flexibility of the manual segmentation interface with automatic image processing and segmentation derived from the

ITK library. Some other options include software such as: ImageJ,[200] OsirisX,[201,166] or Crystal Image.[202,167]

Regarding mesh generation, we described the principal methods used to extract the breast shape and convert MR images into meshes. We focused our attention on the extraction of, first, the surface and, later, the volume mesh. The surface extraction can be performed using high-order polynomials to parameterize the breast surface[21] or by means of isosurface extraction algorithms.[71] Regarding the volume mesh, we exposed the most common procedures to encode the spatial information, type and number of elements as well as the tissue modeled and the simulation performed (see Table I). Notice the wide range of elements and criterions in this section, depending the biomechanical model application. Thus far, image-to-mesh conversion is an open problem. An accurate conversion should fulfill two criteria: obtaining a high-quality mesh to describe organs and tissues without sacrificing geometry or topology, and obtaining an accurate physical behavior when simulating the mechanical deformations. Several approaches have been proposed for this. CGAL[190] is a library that allows extracting the surface and volume meshes as well as the image-to-mesh conversion. Indirectly, CGAL has been used in MRI to mammography registration using the open-source package *iso2mesh* as well as TetGen. Other tetrahedral mesh generator softwares include NetGen,[203] Gmsh,[204,168] BioMesh3D (NIH-SCI, University of Utah),[169] and Cleaver[205,170] (NIH-SCI, University of Utah). Furthermore, the University of Iowa provides the hexahedral mesh generator IA-MESH,[206,171] a freely available software toolkit that employs a multiblock meshing scheme.[207]

6.B. Mechanical deformation

Biomechanical models are becoming increasingly precise and useful tools to simulate the mechanical behavior of human organs, such as the heart, liver, lungs, or pancreas, among others. In addition to the accurate description of the topology and geometry of the breast, knowledge about material parameters or establishing suitable boundary condition for the patient-specific model are required. In Section 3.B Mechanical deformation, we exposed a brief introduction of the physics underling the mechanical deformation with special emphasis on the nonlinear formulation of the elasticity theory.[97] The equations and constitutive relations — i.e., material models — are presented in this section, in order to illustrate the options of the model behavior to the reader. Furthermore, available empirical data of the elastic and hyperelastic parameters are provided, considering the most accepted studies as well as those that have been tested in the FE mechanical simulation. The section concludes with the exposition of loading forces and boundary conditions to obtain an unloaded reference state, to perform the breast compression simulation and a brief overview of the commercial and open-source FE packages that have been tested in the registration between MRI and x-ray mammography. Most of the time, the commercial FE analysis software need to be used. However, some FE solvers have been recently developed specifically to simulate soft-tissue deformations. This is the case not only for CMISS and NiftySim, but also for SOFA[208,172] and FEBio.[209,173] SOFA is an open-source framework focused on real-time medical simulations. In addition to FE simulations, SOFA allows mass–spring and rigid articulated body simulations. In contrast to the software exposed during this work, SOFA has not be tested in breast modeling. On the other hand, FEBio has been tested to simulate breast compression in order to create phantom models from breast CT images.[90] Similar, to previous FEM open-source packages, FEBio does not have mesh generation capabilities. However, to convert FEBio as a complete FE tool, the University of Utah provides complementary frameworks such as: PreView for the preprocessing stage, BioMesh3D as the tetrahedral mesh generator, and PostView for the post-processing stage.

Moreover, newer, faster, and more robust and stable algorithms are being introduced. For instance, NiftySim employs a TLED FE Formulation proposed by Miller et al.[103] for soft-tissue simulation. The efficiency of this algorithm derives from the total Lagrangian framework allowing the shape function derivatives to be precomputed and stored, although the low stiffness of the biological tissues avoids a fast-time step integration. Furthermore, NiftySim has the option of accelerating the simulation using its GPU implementation. Equally, Kuhlmann et al.[102] recently proposed a coupled Eulerian–Lagrangian (CEL) method to simulate the tissue behavior in a more robust and stable way than previous algorithms. These approaches show how the current trend in biomechanical modeling is not only to employ previous tools or software but also to obtain specific formulations for each particular problem.

Furthermore, usually breast FE models are composed of glandular and adipose tissues and, at most, skin, while nerves, blood vessels, and lymph nodes are not considered. Similarly, lesions (tumors) could be included but the accurate segmentation as well as the histopathology of the lesion should be known in advance. Hence, obtaining a fully automatic biomechanical model in diseased breasts, feasible in the clinical practice, may require the segmentation of the nonhealthy structures and adding an automatic diagnosis system, to correct the elastic or hyperelastic properties in these areas.

6.C. Registration

The 3D–2D registration process is divided into ray-casting projection and own registration to optimize the position, orientation and specific parameters of the model. Both task are susceptible to improvement. Several papers have proposed methods to accelerate the ray-casting projection[134,174,175] or accelerating the ray-tracing using GPU technology.[176–179] However, the final intensity values do not depend only on the ray-casting algorithm. Considering the option of accelerating the registration process using GPU capabilities, divergences between monoenergetic beams or one-single-photon rays and a more realistic approximation, such as Monte-Carlo

projection methods, and their influences on the registration process, could be considered.

Regarding the second task, to correlate 3D models to 2D images, Markelj et al.[180] divided the 3D/2D registration process into different groups according to the nature of the registration, such as feature-, intensity-, or gradient-based methods, and according to the strategy to achieve spatial correspondence, such as projective, back-projection, or reconstruction algorithms. The registration methods introduced in the paper are focused on external landmarks, such as breast contour or dice overlap coefficient, and intensity-based methods. Usually, the intensity-based methods are more robust and accurate than feature-based approaches.[181] Nevertheless, the use of gradient-based methods or using back-projective transformations needs to be studied. To our experience, gradient-based metrics, such as gradient correlation, are related to poor results as similarity metrics and they depend on MRI segmentation. However, Mertzanidou et al.[182] obtained good results using gradient difference to lead the registration. Reconstruction-based methods cannot be applied because they require multiple projections from the undeformed body. The addition of DBT (digital breast tomosynthesis) in the registration could be an option to exploit those methods.

6.D. Software

There are many software options regarding image processing, mesh processing and FE analysis. Usually, visualization tools need to be included in the process. Most of the commercial FE software packages include their own tools to visualize the deformation, forces and stress–strain relationship after the analysis. When visualization tools are not available internally, external software, such as Paraview*TM*,[210] ImageMagick,[211] or OpenDX[212] are useful. During this work, we have used the software Medit[213] (INRIA, Rocquencourt, France)[185] to visualize the internal structure of a biomechanical model (Fig. 5), and MeVisLab*TM* [214] (MeVis Medical Solutions AG, Bremen, Germany) to process and visualize the 2D and 3D images.

So far, there is not a single tool that includes or integrates the entire process of developing a biomechanical model using a single software package. Additionally, the segmentation of medical images and parametrization of the surfaces are hardly found together in the same tool. Consequently, many software options need to be evaluated to obtain a suitable result in the simulation. Table IV collects the software platforms employed in this task, referenced in the literature. Choosing the tools to be employed wisely can reduce and improve the final result. From a practical point of view, the discussion can be focused on using commercial or open-source software. Both options imply advantages and disadvantages. Obviously, commercial software has been widely tested until a final version is released, while, open-source software allows the user to examine the actual state of the program and to even modify it under GNU licenses, improving or adapting their characteristics to the proposed problem. This question requires not only to be familiarized with the problem and the mathematical formulation but also the knowledge of computer programming and the algorithms. Depending on the background of the researcher, these considerations may imply added difficulty.

Interpreted programming languages, such as MATLAB and python, provide a good basis for fast algorithm prototyping and are easy to learn, while compiled languages, such as C++, may require more experience and the availability of the corresponding compiler. However, most of open-source libraries, such as ITK and VTK, are written (or provide a version) in C++. Similarly, FE open-source packages, such as Nifty-Sim and SOFA, have been developed in C++. Conversely to commercial FE packages that provide an installer executable, open-source libraries may provide just the source-code which needs to be compiled, and may depend on additional third-party libraries that need to be installed independently. Commercial FE packages provide graphical users interface (GUI) to facilitate the communication between the user and the software while open-source packages may require to be executed in terminal.

In addition to the accuracy, the potential clinical application of an algorithm requires to consider the computational time to make it suitable in the practice. When dealing with biomechanical models, the computational time is related to the number of elements, among other factors such as the type of FE analysis (static/dynamic) and the number of iterations to solve the equations. Furthermore, when the registration algorithm needs to repeat the FE analysis, as is the case of Mertzanidou et al.[71], the number of simulations as well as hardware capabilities need to be considered. In our experience, software packages such as ANSYS, Abaqus, and FeBio may require a long time to perform one single simulation — i.e., the compression of the breast — depending on the number of elements, when they are running in a personal computer. Notice that these tools are able to use multiprocessor servers, accelerating the results. Furthermore, SOFA is focused on real time simulations and NiftySim uses the GPU capabilities to speed-up the simulation. Regarding NiftySim, one single compression of the model exposed in Section 5, composed of 78,098 4-node tetrahedral elements, may require about 1 min. Notice that NiftySim was written using CUDA and it requires NVIDIA graphic cards. Similarly, ANSYS and Abaqus support a large number of NVIDIA[215] (NVIDIA, Santa Clara, CA, USA) and AMD[216] (Advanced Micro Devices Inc., Sunnyvale, CA, USA) graphic cards.

Finally, open-source FE packages may reduce the number of options with respect to commercial packages. While NiftySim is focused on a dynamic explicit solution of the nonlinear tissue behavior, FeBio includes Multiphysics (mechanics, fluid flow, heat conduction) simulations but is also focused on nonlinear FE simulations. Even when this particular skill is suitable to simulate the soft-tissue behavior, other applications may require to define a different approach. Thus, ANSYS and Abaqus can perform linear and nonlinear as well as static/dynamic and explicit/implicit simulations.

Involving a large number of software options in the resolution of a problem requires the capability of communicating

TABLE IV. Software options.

	Area	Software	
Commercial software	Image processing	Matlab^{TM}	Hsu et al.[90], Han et al.[91], Hopp et al.[44], Solves-Llorens[52]
		ANALYZE^{TM}	Samani et al.[81], Tanner et al.[60,61,89], Schnabel et al.[29], Carter et al.[87,62], Han et al.[91]
	Mesh processing	ScanIP^{TM}	Solves-Llorens et al.[52]
		Harpoon^{TM}	del Palomar et al.[84]
	FE analysis	ANSYS^{TM}	Tanner et al.[60,61,89], Schnabel et al.[29], Qiu et al.[154,22], Ruiter et al.[183], Carter et al.[87,62], Hipwell et al.[88], Zhang et al.[66], Solves-Llorens et al.[52]
		Abaqus^{TM}	Samani et al.[81], Azar et al.[46], del Palomar et al.[84], Han et al.[91], Hopp et al.[11,44]
Open-source software	Image processing	ITK	Lee et al.[184,21], García et al.[145,56]
		VTK	Tanner et al.[60,61,89]), Schnabel et al.[29], Carter et al.[87],Mertzanidou et al.[58], Eiben et al.[28], García et al.[56]
		NiftySeg	Mertzanidou et al.[58], Han et al.[91]
	Mesh processing	Tetgen	Han et al.[91], Eiben et al.[28,124], Mertzanidou et al.[71], García et al.[56]
		iso2mesh	Hopp et al.[11,44]
		MeshLab	Eiben et al.[28]
	FE analysis	FeBio	Hsu et al.[90], Eiben et al.[124]
		NiftySim	Han et al.[91], Mertzanidou et al.[58], Eiben et al.[28,124], García et al.[56]
		OpenCMISS	Pathmanathan et al.[86,42], Rajagopal et al.[78], Chung et al.[79], Lee et al.[21]

all of these software. Usually, open-source tools can be included as a library in the project; meanwhile, establishing a connection with a commercial tool may be challenging. Some exceptions can be found, provided by the environment [for instance, COMSOL Multiphysics*TM* [217] (COMSOL Group, Stockholm, Sweden) provides to a server to establish communication with MATLAB^{TM}] or by means of free code communities (lately, a tool to establish communication between MATLAB^{TM} and ABAQUS^{TM} can be found in the Matlab Central webpage[218]). Otherwise, FE model files must be written using the native scripting language for each tool.

7. CONCLUSIONS

In this paper, we have reviewed the breast MRI to x-ray mammography registration problem solved using a patient-specific biomechanical model. This is a hard task because of, among other factors, the inherent breast deformation that is performed during the mammographic acquisition. We presented a step-by-step description of the whole process. From the MRI volume, the woman's breast geometry is extracted including the internal tissue distribution, and is used to create a 3D model. This model, comprising surface and volumetric meshes, is deformed using the FE approach, allowing physically reliable deformation. Subsequently, the 2D projections of the model are obtained to represent the mammographic views and are used to register the model in an iterative process. Each step has been largely discussed, introducing the principal software tools, different materials and the parameters proposed in the literature. In addition, the results obtained by these approaches have been summarized.

Although current results start to make MRI to x-ray mammography registration a realistic tool, many avenues remain to be investigated that makes this topic an active area within computer vision. We believe that the commented trends and software proposed will improve the paradigm, obtaining faster and more robust registration approaches that can significantly help crucial aspects of every-day clinical practice such as the diagnosis, follow-up, and breast mapping studies.

ACKNOWLEDGMENTS

This work was partially funded by the Ministry of Economy and Competitiveness of Spain grant under project reference DPI2015-68442-R and by Universitat de Girona by UdG grant MPCUdG2016/022. Eloy Garca holds a FPI grant BES-2013-065314.

CONFLICTS OF INTEREST

The authors have no relevant conflicts of interest to disclose.

[a]Authors to whom correspondence should be addressed. Electronic mails: eloygm82@gmail.com, aoliver@eia.udg.edu.

REFERENCES

1. BreastCancer.org.; 2016. BreastCancer.org, url: http://www.breastcancer.org/symptoms/testing/types.
2. Yaffe MJ. Basic physics of digital mammography. In: Bick U, Diekmann F, eds. *Digital Mammography.* Berlin: Springer; 2010:1–11.
3. Hendrick RE, ed. *Breast MRI. Fundamentals and Technical Aspects*. Berlin: Springer; 2008.
4. Miller AB, Wall C, Baines CJ, Sun P, To T, Narod SA. Twenty five year follow-up for breast cancer incidence and mortality of the Canadian National Breast Screening Study: randomised screening trial. *Br Med J.* 2014;348:g366.
5. Moss SM, Cuckle H, Evans A, et al. Effect of mammographic screening from age 40 years on breast cancer mortality at 10 years' follow-up: a randomised controlled trial. *Lancet.* 2006;368:2053–2060.

6. Tabar L, Yen M-F, Vitak B, Chen H-HT, Smith RA, Duffy SW. Mammography service screening and mortality in breast cancer patients: 20-year follow-up before and after introduction of screening. *Lancet.* 2003;361:1405–1410.
7. Malur S, Wurdinger S, Moritz A, Michels W, Schneider A. Comparison of written reports of mammography, sonography and magnetic resonance mammography for preoperative evaluation of breast lesions, with special emphasis on magnetic resonance mammography. *Breast Cancer Res.* 2001;3:55–60.
8. American Cancer Society Inc. 2016.
9. Perry N, Broeders M, Wolf C, Törnberg S, Holland R, Karsa L, eds. *European Guidelines for Quality Assurance in Breast Cancer Screening and Diagnosis* (4th ed.). Luxembourg: European Commission, Office for Official Publications of the European Union; 2006.
10. Dietzel M, Hopp T, Ruiter N, et al. Fusion of dynamic contrast-enhanced magnetic resonance mammography at 3.0T with X-ray mammograms: pilot study evaluation using dedicated semi-automatic registration software. *Eur J Radiol.* 2011:98–102.
11. Hopp T, Baltzer P, Dietzel M, Kaiser WA, Ruitter NV. 2D/3D Image fusion of X-ray mammograms with breast MRI: visualizing dynamic contrast enhancement in mammograms. *Int J Comput Assist Radiol Surg*. 2012;7:339–348.
12. Hopp T, Duric N, Ruiter NV. Image fusion of ultrasound computer tomography volumes with X-ray mammograms using a biomechanical model based 2D/3D registration. *Comput Med Imaging Graph.* 2015;40:170–181.
13. Ferrant M, Wardfield SK, Nabavi A, Jolesz FA, Kikinis R. Registration of 3D intraoperative MR images of the brain using a finite element biomechanical Model*Proceeding in Medical Image Computing and Computer-Assisted Intervention, Berlin, in Lecture Notes in Computer Science.*; 2000:1935:19-28.
14. Sermesant M, Forest C, Pennec X, Ayache H, Delingette H., Ayache N. Deformable biomechanical models: application to 4D cardiac image analysis. *Med Image Anal.* 2003;7:475–488.
15. Hu T, Desai JP. A biomechanical model of the liver for reality-based haptic feedback. In: *Medical Image Computing and Computer-Assisted Intervention - MICCAI 2003*. Berlin, Heidelberg: Springer; 2003:75–82.
16. Fuerst B, Mansi T, Carnis F, et al. Patient-specific biomechanical model for the prediction of lung motion from 4-D CT images. *IEEE Trans Med Imaging.* 2015;34:599–607.
17. Mohamed A, Davatzikos C, Taylor R. A combined statistical and biomechanical model for estimation of intra-operative prostate deformation. In: Dohi T, Kikinis R, eds, *Medical Image Computing and Computer-Assisted Intervention — MICCAI 2002*. Vol. 2489. Berlin, Heidelberg: Springer; 2002:452–460.
18. Miller K, Nielsen P. *Computational Biomechanics for Medicine*. Germany: Springer Science and Business Media; 2010.
19. Payan Y. *Soft Tissue Biomechanical Modeling for Computer Assisted Surgery.* Germany: Springer Science and Business Media; 2012.
20. Gefen A, ed. *Patient-Specific Modeling in Tomorrow's Medicine*. Berlin: Springer Berlin Heidelberg; 2011.
21. Lee A, Rajagopal V, Gamage TPB, Doyle AJ, Nielsen PMF, Nash MP. Breast lesion co-localisation between X-Ray and MR images using finite element modelling. *Med Image Anal*. 2013;17:1256–1264.
22. Qiu Y, Sun X, Manohar V, Goldgof D. Towards registration of temporal mammograms by finite element simulation of MR breast volumes. In: *Medical Imaging*. Bellingham: International Society for Optics and Photonics; 2008:69182F.
23. Hopp T, Neupane B, Ruiter N. Automated multimodal computer aided detection based on a 3D-2D image registration. In: *International Workshop on Digital Mammography - IWDM'16*. Berlin: Springer; 2016:383–309.
24. Azar FS, Metaxas DN, Schnall MD. A Finite Element Model of the Breast for Prediction Mechanical Deformations during Biopsy Procedures. Mathematical Methods in Biomedical Image Analysis, Proceedings. IEEE Workshop; 2000:38-45.
25. Georgii J, Eder M, Bürger K, et al. A computational tool for preoperative breast augmentation planning in aesthetic plastic surgery. *IEEE J Biomed Health Inform.* 2014;14:907–919.
26. Gamage TPB, Rajagopal V, Nielsen PMF, Nash MP. Patient-specific modeling of breast biomechanics with applications to breast cancer detection and treatment. In: Gefen A, ed. *Patient-Specific Modeling in Tomorrow's Medicine*. Berlin, Heidelberg: Springer-Verlag; 2011:379–412.
27. Hipwell JH, Vavourakis V, Han L, Mertzanidou T, Eiben B, Hawkes DJ. A review of biomechanically informed breast image registration. *Phys Med Biol*. 2016;61:R1.
28. Eiben B, Han L, Hipwell J, et al. Biomechanically guided prone-to-supine image registration of breast MRI using an estimated reference state. IEEE 10th International Symposium on Biomedical Imaging: From Nano to Macro; 2013.
29. Schnabel J, Tanner C, Castellano-Smith AD, et al. Validation of non-rigid image registration using finite-element methods: application to breast MR images. *IEEE Trans Med Imaging*. 2003;22:283–247.
30. Hogg P, Kelly J, Mercer C, eds. *Digital Mammography: A Holistic Approach*. Berlin: Springer; 2015.
31. Foundation National Breast Cancer; 2016. National Breast Cancer Foundation, url: http://www.nationalbreastcancer.org/breast-anatomy.
32. Pathology Johns Hopkins; 2016. Johns Hopkins Pathology and Sidney Kimmel Cancer Center at Johns Hopkins, url: http://pathology.jhu.edu/breast/anatomy.php.
33. Krüger J, Ehrhardt J, Bischof A, Handels H. Simulation of mammographic breast compression in 3D MR images using ICP-based B-spline deformation for multimodality breast cancer diagnosis. *Int J Comput Assist Radiol Surg*. 2014;9:367–377.
34. Roose L, De Maerteleire W, Mollemans W, Suetens P. Validation of different soft tissue simulation methods for breast augmentation. *Int Congr Ser.* 2005;1281:485–490Elsevier.
35. Roose L, Mollemans W, Loeckx D, Maes F, Suetens P. *Biomechanically based elastic breast registration using mass tensor simulation*. In: Larsen R, Nielsen M, Sporring J, eds. Medical Image Computing and Computer-Assisted Intervention - MICCAI 2006. vol 4191. MICCAI 2006. Lecture Notes in Computer Science. Berlin, Heidelberg: Springer; 2006:718–725.
36. Roose L, Loeckx D, Mollemans W, Maes F, Suetens P. Adaptive boundary conditions for physically based follow-up breast MR image registration. *Med Image Comput Comput Assist Interv.* 2008;11:839–846.
37. Gamage TPB, Nielsen PMF, Nash MP. Clinical applications of breast biomechanics. In: *Biomechanics of Living Organs. Hyperelastic Constitutive Laws for Finite Element Modeling*. Cambridge, MA: Academic Press, Elsevier; 2017:215–242.
38. Wang L, Chitiboi T, Meine H, Günther M, Hahn HK. Principles and methods for automatic and semi-automatic tissue segmentation in MRI data. *Magn Reson Mater Phys Biol Med*. 2016;29:95–110.
39. Vovk U, Pernus F, Likar B. A review of methods for correction of intensity inhomogeneity in MRI. *IEEE Trans Med Imaging*. 2007;26:405–421.
40. Sled JG, Zijdenbos AP, Evans Alan C. A nonparametric method for automatic correction of intensity nonuniformity in MRI data. *IEEE Trans Med Imaging*. 1998;17:87–97.
41. Tustison NJ, Avants BB, Cook PA, et al. N4ITK: improved N3 bias correction. *IEEE Trans Med Imaging*. 2010;29:1310–1320.
42. Pathmanathan P, Whiteley J, Chapman SJ, Gavaghan D, Brady JM. Predicting tumour location by modelling the deformation of the breast. *IEEE Trans Biomed Eng*. 2008;55:2471–2480.
43. Gubern-Mérida A, Kallenberg M, Mann RM, Marti R, Karssemeijer N. Breast segmentation and density estimation in breast MRI: a fully automatic framework. *IEEE J Biomed Health Inform*. 2015;19:349–357.
44. Hopp T, Dietzel M, Baltzer M, Kaiser W, Gemmeke H, Ruiter N. Automatic multimodal 2D/3D breast image registration using biomechanical FEM models and intensity-based optimization. *Med Image Anal.* 2013;17:209–218.
45. Chan TF, Vese LA. Active contours without edges. *IEEE Trans Image Process*. 2001;10:266–277.
46. Azar FS, Metaxas DN, Schnall MD. A deformable finite element model of the breast for predicting mechanical deformations under external perturbations. *Acad Radiol*. 2001;8:965–975.
47. Ruiter NV, Stotzka R, Müller TO, Gemmeke H, Reichenbach JR, Kaiser WA. Model-based registration of X-ray mammograms and MR images of the female breast. *IEEE Trans Nucl Sci*. 2006;53:204–211.

48. Solves-Llorens JA, Rupérez MJ, Monserrat C, Feliu E, García M, Lloret M. Segmentation of the breast skin and its influence in the simulation of the breast compression during an X-ray mammography. *Sci World J*. 2012;876489.
49. Wu S, Weinstein SP, Conant EF, Schnall MDKontos D. Automated chest wall line detection for whole-breast segmentation in sagittal breast MR images. *Med Phys*. 2013;40:042301.
50. Giannini V, Vignati A, Morra L, et al. *A fully automatic algorithm for segmentation of the breasts in DCE-MR images*. In: *Engineering in Medicine and Biology Society (EMBC), 2010 Annual International Conference of the IEEE*. IEEE; 2010:3146–3149.
51. Wang L, Filippatos K, Friman O, Hahn HK. Fully automated segmentation of the pectoralis muscle boundary in breast MR images in *SPIE Medical Imaging*, International Society for Optics and Photonics; 2011: 796309.
52. Solves-Llorens JA, Rupérez MJ, Monserrat C. A complete software application for automatic registration of X-ray mammography and magnetic resonance images. *Med Phys*. 2014;41:081903.
53. Wang L, Platel B, Ivanovskaya T, Harz M, Hahn HK. *Fully automatic breast segmentation in 3D breast MRI* in *Biomedical Imaging (ISBI), 2012 9th IEEE International Symposium on*:2012;1024–1027.
54. Ortiz CG, Martel AL. Automatic atlas-based segmentation of the breast in MRI for 3D breast volume computation. *Med Phys*. 2012;39:5835–5848.
55. Gubern-Mérida A, Kallenberg M, Martí R, Karssemeijer N. Segmentation of the pectoral muscle in breast MRI using atlas-based approaches. In: *Medical Image Computing and Computer-Assisted Intervention, MICCAI*. Berlin, Heidelberg:Springer; 2012.
56. García E, Oliver A, Diez Y, et al. Mapping 3D breast lesions from full-field digital mammograms using subject-specific finite element models. in *SPIE Medical Imaging*:2017.
57. Lee J-D, Su H-R, Cheng PE. MR image segmentation using a power transformation approach. *IEEE Trans Med Imaging*. 2009;28:894–905.
58. Mertzanidou T. Automatic Correspondence between 2D and 3D Images of the Breast. PhD thesis. Centre for Medical Image Computing, University College London: London, UK; 2012.
59. Cardoso MJ, Clarkson MJ, Ridgway GR, et al. LoAd: a locally adaptive cortical segmentation algorithm. *Neuroimage*. 2011;56:1386–1397.
60. Tanner C, Degenhard A, Schnabel JA, et al. A method for the comparison of biomechanical breast models. In *Mathematical Methods in Biomedical Image Analysis, 2001. MMBIA 2001. IEEE Workshop on*. IEEE; 2001:11–18.
61. Tanner C, Schnabel JA, Hill DLG, Hawkes DJ, Leach MO, Hose DR. Factors influencing the accuracy of biomechanical breast models. *Med Phys*. 2006;33:1758–1769.
62. Carter T, Tanner C, Beechey-Newman N, Barrat D, Hawkes D. MR navigated breast surgery: method and initial clinical experience. 11th International Conference on Medical Image Computing and Computer-Assisted Intervention (MICCAI'08) in Lecture Notes in Computer Science. 2008;5242:356–363.
63. Dice LR. Measures of the amount of ecologic association between species. *Ecology*. 1945;26:297–302.
64. Levandowsky M, Winter D. Distance between sets. *Nature*. 1971;234:34–35.
65. Gubern-Mérida A, Kallenberg M, Platel B, Mann RM, Martí R, Karssemeijer N. Volumetric breast density estimation from full-field digital mammograms: a validation study. *PLoS One*. 2014;9:e85952.
66. Zhang Y, Qiu Y, Goldgof DB, Sarkar S, Li H. 3D finite element modeling of nonrigid breast deformation for feature registration in X-ray and MR image. 7th IEEE Workshop on Applications of Computer Vision (WACV'07). 2007.
67. Chung JH, Rajagopal V, Nielsen P, Nash M. Modeling mammographic compression of the breast. *11th International Conference on Medical Image Computing and Computer-Assisted Intervention (MICCAI'08) in Lecture Notes in Computer Science*. 2008;5242:758–765.
68. Rajagopal V, Lee A, Chung JH, et al. Toward tracking breast cancer across medical images using subject-specific biomechanical models. In: *Medical Image Computing and Computer-Assisted Intervention–MICCAI 2007*. 4791: Berlin: Springer; 2007:651–658.
69. Lorensen WE, Cline HE. Marching cubes: a high resolution 3D surfaces construction algorithm. *ACM Comput Graph*. 1987;21:163–169.
70. Osher S, Sethian JA. Fronts propagating with curvature-dependent speed: algorithms based on Hamilton-Jacobi formulations. *J Comput Phys*. 1988;79:12–49.
71. Mertzanidou T, Hipwell J, Johnsen S, et al. MRI to X-ray mammography intensity-based registration with simultaneous optimisation of pose and biomechanical transformation parameters. *Med Image Anal*. 2014;18:674–683.
72. Herrmann LR. Laplacian-isoparametric grid generation scheme. *J Eng Mech Divis*. 1976;102:749–907.
73. Lawson CL. Transforming triangulations. *Discr Math*. 1972;3:365–372.
74. Lo Daniel SH. *Finite Element Mesh Generation*. Boca Raton, FL: CRC Press; 2015.
75. Garland M, Heckbert PS. Surface simplification using quadric error metrics. In: Proceedings of the 24th annual conference on Computer graphics and interactive techniques. New York, NY: ACM Press/Addison-Wesley Publishing Co.; 1997:209–216.
76. Lindstrom P. Out-of-core simplification of large polygonal models. In: Proceedings of the 27th annual conference on Computer graphics and interactive techniques, ACM Press/Addison-Wesley Publishing Co.; 2000:259–262.
77. Aspert N, Santa-Cruz D, Ebrahimi T. Mesh: Measuring errors between surfaces using the Hausdorff distance. In: Multimedia and Expo, 2002. ICME'02. Proceedings. 2002 IEEE International Conference on. 1; IEEE; 2002:705–708.
78. Rajagopal V. *Modelling breast tissue mechanics under gravity loading*. PhD thesis. The University of Auckland New Zealand 2007.
79. Chung JH. *Modelling Mammographic Mechanics*. PhD thesis. University of Auckland, New Zealand 2008.
80. Azar FS, Metaxas DN, Schnall MD. Methods for modelling and predicting mechanical deformations of the breast under external perturbations. *Med Image Anal*. 2002;6:1–27.
81. Samani A, Bishop J, Yaffe MJ, Plewes DB. Biomechanical 3-D finite element modelling of the human breast using MRI data. *IEEE Trans Med Imaging*. 2001;20:271–279.
82. Ramos A, Simoes JA. Tetrahedral versus hexahedral finite elements in numerical modelling of the proximal femur. *Med Eng Phys*. 2006;28:916–924.
83. Zhang G. Image-based modeling for bioengineering problems. In: *Computational Bioengineering*. Boca Raton, FL: CRC Press; 2015.
84. Palomar AP, Calvo B, Herrero J, López J, Doblaré M. A finite element model to accurately predict real deformations of the breast. *Med Eng Phys*. 2008;30:1089–1097.
85. Fang Q, Boas D. Tetrahedral Mesh Generation from Volumetric Binary and Gray-Scale Images. In: *IEEE International Symposium on Biomedical Imaging, Proceedings of*: IEEE International Symposium on Biomedical Imaging Proceedings of; 2009: 1142–45.
86. Pathmanathan P, Gavaghan D, Whiteley J, et al. Predicting tumour location by simulating large deformations of the breast using a 3D finite element model and nonlinear elasticity. In: *Medical Image Computing and Computer-Assisted Intervention MICCAI*. vol. 3217, MICCAI: Berlin, Heidelberg: Springer; 2004:217–224.
87. Carter TJ, Tanner C, Crum WR, Beechey-Newman N, Hawkes DJ. A framework for image-guided breast surgery. In: *International Workshop on Medical Imaging and Virtual Reality*. Berlin: Springer; 2006:203–210.
88. Hipwell JH, Tanner C, Crum WR, Schnabel JA, Hawkes DJ. A new validation method for X-ray mammogram registration algorithms using a projection model of breast X-ray compression. *IEEE Trans Med Imaging*. 2007;26:1190–1200.
89. Tanner C, White M, Guarino S, Hall-Craggs M, Douek M, Hawkes D. Large breast compressions – observations and valuation of simulations. *Med Phys*. 2011;38:682–690.
90. Hsu CML, Palmeri ML, Segars WP, Veress AI, Dobbins III JT. An analysis of the mechanical parameters used for finite element compression of a high-resolution 3D breast phantom. *Med Phys*. 2011;38:5756–5770.
91. Han L, Hipwell J, Tanner C, et al. Development of patient-specific biomechanical models for predicting large breast deformation. *Phys Med Biol*. 2012;57:455–472.
92. Hopp T, Ruitter NV. 2D/3D Registration for localization of mammographically depicted lesions in breast MRI. Lecture Notes in Computer Science. 2012;7361:627–634.

93. Si HT. A Delaunay-based quality tetrahedral mesh generator. *ACM Trans Math Softw*. 2015;41:11.
94. Dompierre J, Vallet M-G, Labbé P, Guibault F. An analysis of simplex shape measures for anisotropic meshes. *Comput Methods Appl Mech Eng*. 2005;194:4895–4914.
95. Krouskop TA, Wheeler TM, Kallel F, Garra BS, Hall T. The elastic moduli of breast and prostate tissues under compression. *Ultraso Imaging*. 1998;20:151–159.
96. Wellman PS. *Tactile Imaging*. PhD thesis, Cambridge, MA: Harvard University's Division of Engineering and Applied Sciences 1999.
97. Malvern LE. *Introduction to the Mechanics of a Continuous Medium*: 282–290. New Jersey, NJ: Prentice-Hall; 1969.
98. Whiteley JP, Chapman SJ, Gavaghan DJ, Brady JM. Non-linear modelling of breast tissue. *Mat Med Biol*. 2007;24:327–345.
99. Bathe K-J. *Finite Element Procedures, 2nd edition*. Upper Saddle River: Prentice Hall; 2014.
100. Bonet J, Wood RD. *Nonlinear Continuum Mechanics for Finite Element Analysis*. Cambridge: Cambridge University Press; 1997.
101. Zienkiewicz OC, Taylor RL. *The Finite Element Method. Vol.2: Solid Mechanics*. New York, NY: McGraw-Hill; 2000.
102. Kuhlmann M, Fear EC, Ramirez-Serrano A, Federico S. Mechanical model of the breast for the prediction of deformation during imaging. *Med Eng Phys*. 2013;35:470–478.
103. Miller K, Joldes G, Lance D, Wittek A. Total Lagrangian explicit dynamics finite element algorithm for computing soft tissue deformation. *Commun Numer Methods Eng*. 2007;23:121–134.
104. Atkinson KE. *An Introduction to Numerical Analysis*. Hoboken, NJ: John Wiley & Sons; 2008.
105. Hopp T, Barros R, Simioni W, Perez JAE, Ruiters NV. Comparison of biomechanical models for MRI to X-ray mammography registration. In: Proceedings of, 3rd MICCAI Workshop on Breast Image Analysis, MICCAI-BIA. 3:Springer; 2015:81–89.
106. Doyley MM. Model-based elastography: a survey of approaches to the inverse elasticity problem. *Phys Med Biol*. 2012;57:R35–R75.
107. Fung YC. *Biomechanics: Mechanical Properties of Living Tissues, 2nd ed*. Berlin: Springer; 1993.
108. Bakic PR. *Breast tissue description and modeling in mammography.* PhD thesis, Lehigh University; 2000.
109. Lorenzen J, Sinkus R, Lorenzen M, et al. MR elastography of the breast: preliminary clinical results. In: *RoFo-Fortschritte auf dem Gebiete der Rontgenstrahlen und der Neuen Bildgebenden Verfahren*. 174: Stuttgart: Thieme, c1989-2002:830–834.
110. Azar FS. *A Deformable Finite Element Model of the Breast for Predicting Mechanical Deformations under External Perturbations*. PhD thesis, University of Pennsylvania; 2001.
111. Gamage TPB, Rajagopal V, Ehrgott M, Nash MP, Nielsen PMF. Identification of mechanical properties of heterogenous soft bodies using gravity loading. *J Numer Methods Biomed*. 2011;27:391–407.
112. Rajagopal V, Lee A, Chung JH, Nielsen P, Nash M. Creating individual-specific biomechanical models of the breast for medical image analysis. *Acad Radiol*. 2008;15:1425–1436.
113. Lapuebla-Ferri A, Palomar AP, Herrero J, Jiménez-Mocholí A-J. A patient-specific FE-based methodology to simulate prosthesis insertion during an augmentation mammoplasty. *Med Eng Phys*. 2011;33:1094–1102.
114. Samani A, Plewes DA. A method to measure the hyperelastic parameters of ex-vivo breast tissue samples. *Phys Med Biol*. 2004;9:4395–4405.
115. Reihsner R, Balogh B, Menzel E. Two dimensional elastic properties of human skin in terms of an incremental model at the in vivo configuration. *Med Eng Phys*. 1995;17:304–313.
116. Edwards C, Marks R. Evaluation of biomechanical properties of human skin. *Clin Dermatol*. 1995;13:375–380.
117. Groves RB, Coulman SA, Birchall JC, Evans SL. An anisotropic, hyperelastic model for skin: experimental measurements, finite element modelling and identification of parameters for human and murine skin. *J Mech Behav Biomed Mater*. 2013;18:167–180.
118. Bischoff JE, Arruda EM, Grosh K. Finite element modeling of human skin using an isotropic, nonlinear elastic constitutive model. *J Biomech*. 2000;33:645–652.
119. Mahmud J, Holt C, Evans S, Manan N, Fazli A, Chizari M. A parametric study and simulations in quantifying human skin hyperelastic parameters. *Proc Eng*. 2012;41:1580–1586.
120. O'Hagan JJ, Samani A. Measurement of the hyperelastic properties of tissue slices with tumour inclusion. *Phys Med Biol*. 2008;53:7087–7106.
121. O'Hagan JJ, Samani A. Measurement of the hyperelastic properties of 44 pathological ex vivo breast tissue samples. *Phys Med Biol*. 2009;54:2557–2569.
122. Georgii J, Pätz T, Harz MT, et al. Simulation and visualization to support breast surgery planning. In: Breast Imaging - 13th International Workshop, IWDM 2016, Malmö, Sweden, 2016, Proceedings: 2016:257–264.
123. Rajagopal V, Chung J-H, Bullivant D, Nielsen PMF, Nash MP. Determining the finite elasticity reference state from a loaded configuration. *Int J Numer Methods Eng*. 2007;72:1434–1451.
124. Eiben B, Vavourakis V, Hipwell JH, et al. Breast deformation modelling: comparison of methods to obtain a patient specific unloaded configuration. *Proc SPIE*. 2014; 9036:903615–8.
125. Carter TJ, Tanner C, Hawkes DJ. Determining material properties of the breast for image-guided surgery, In: SPIE Medical Imaging. International Society for Optics and Photonics; 2009:726124.
126. Rajagopal V, Nash MP, Highnam RP, Nielsen PMF. The breast biomechanics reference state for multi-modal image analysis. In: *Digital Mammography*. Berlin: Springer; 2008:385–392.
127. Govindjee S, Mihalic PA. Computational methods for inverse finite elastostatics. *Comput Methods Appl Mech Eng*. 1996;136:47–57.
128. Vavourakis V, Hipwell JH, Hawkes DJ. An inverse finite element u/p-formulation to predict the unloaded state of in vivo biological soft tissues. *Ann Biomed Eng*. 2016;44:187–201.
129. Groot JE, Branderhorst W, Grimbergen CA, Heeten GJ, Broeders MJM. Towards personalized compression in mammography: a comparison study between pressure-and force-standardization. *Eur J Radiol*. 2015;84:384–391.
130. Elangovan P, Warren LM, Mackenzie A, et al. Development and validation of a modelling framework for simulating 2D-mammography and breast tomosynthesis images. *Phys Med Biol*. 2014;59:4275.
131. Li CM, Segars WP, Tourassi GD, Boone JM, Dobbins JT. Methodology for generating a 3D computerized breast phantom from empirical data. *Med Phys*. 2009;36:3122–3131.
132. Peplow DE, Verghese K. Digital mammography image simulation using Monte Carlo. *Med Phys*. 2000;27:568–579.
133. Bom MJ, Pluim JPW, Gounis MJ, et al. Registration of 2D x-ray images to 3D MRI by generating pseudo-CT data. *Phys Med Biol*. 2011;56:1031.
134. Siddon RL. Fast calculation of the exact radiological path for a three-dimensional CT array. *Med Phys*. 1985;12:252–255.
135. Staub D, Murphy MJ. A digitally reconstructed radiograph algorithm calculated from first principles. *Med Phys*. 2013;40:011902.
136. Mertzanidou T, Hipwell J, Cardoso MJ, et al. MRI to X-ray mammography registration using a volume-preserving affine transformation. *Med Image Anal*. 2012;16:966–975.
137. Guo Y, Sivaramakrishna R, Lu C-C, Suri JS, Laxminarayan S. Breast image registration techniques: a survey. *Med Biol Eng Comput*. 2006;44:15–26.
138. Hill DLG, Batchelor PG, Holden M, Hawkes DJ. Medical image registration. *Phys Med Biol*. 2001;46:R1.
139. Maintz JBA, Viergever MA. A survey of medical image registration. *Med Image Anal*. 1998;2:1–36.
140. Rueckert D, Schnabel JA. Medical image registration. In: *Biomedical Image Processing*. Berlin: Springer; 2010:131–154.
141. Müller TO, Ruiter NV, Storzka R, Kaiser WA. Automatic matching of MR volume data and X-ray mammograms. *Eur Radiol*. 2000;10:F52.
142. Behrenbruch CP, Marias K, Yam M, Brady JM, English RE. The use of magnetic resonance imaging to model breast compression in X-Ray mammography for MR/X-Ray data fusion. In: Proceedings of, 5th Workshop on Digital Mammography. Citeseer; 2000:81–89.
143. Martí R, Zwiggelaar R, Rubin CME, Denton ERE. Two-dimensional–three-dimensional correspondence in mammography. *Cybern Syst Int J*. 2004;35:85–105.

144. Kita Y, Highnam R, Brady M. Correspondence between different view breast X-rays using curved epipolar lines. *Comput Vis Image Understand*. 2001;83:38–56.
145. García E, Oliver A, Diez Y, et al. Comparing regional breast density using Full-Field Digital Mammograms and Magnetic Resonance Imaging: A preliminary study. In: MICCAI Workshop on Breast Image Analysis; 2015:33–41.
146. Vercauteren T, Pennec X, Perchant A, Ayache N. Diffeomorphic demons: efficient non-parametric image registration. *NeuroImage*. 2009;45:S61–S72.
147. Mertzanidou T, Hipwell J, Han L, Huisman H, Karssemeijer N, Hawkes D. MRI to X-ray mammography registration using an ellipsoidal breast model and biomechanically simulated compressions. In: MICCAI Workshop on Breast Image Analysis.; 2011:191–168.
148. Chang Y-C, Huang Y-H, Huang C-S, Chen J-H, Chang R-F. Computerized breast lesions detection using kinetic and morphologic analysis for dynamic contrast-enhanced MRI. *Magn Reson Imaging*. 2014;32:514–522.
149. Gubern-Mérida A, Martí R, Melendez J, et al. Automated localization of breast cancer in DCE-MRI. *Med Image Anal*. 2015;20:265–274.
150. Renz DM, Böttcher J, Diekmann F, et al. Detection and classification of contrast-enhancing masses by a fully automatic computer-assisted diagnosis system for breast MRI. *J Magn Reson Imaging*. 2012;35:1077–1088.
151. Mertzanidou T, Hipwell JH, Han L, et al. Intensity-based MRI to X-ray mammography registration with an integrated fast biomechanical transformation. In: Maidment ADA, Bakic PR, Gavenonis S, eds. *International Workshop on Breast Imaging*. vol 7361. Berlin, Heidelberg: Springer; 2012:48–55.
152. García E, Diez Y, Diaz O, et al. Multimodal breast parenchymal patterns correlation using a patient-specific biomechanical model. *IEEE Trans Med Imaging*. 2017. DOI: 10.1109/TMI.2017.2749685
153. Kirkpatrick S, Gelatt CD, Vecchi MP. Optimization by simulated annealing. *Science*. 1983;220:671–680.
154. Qiu Y, Goldgof D, Li L, Sarkar S, Zhang Y, Anton S. Correspondence recovery in 2-view mammography. In: Biomedical Imaging: Nano to Macro, 2004. IEEE International Symposium on. IEEE; 2004:197–200.
155. Lagae A, Dutré P. Compact, fast and robust grids for ray tracing. *Comput Graph Forum*. 2008;27:1235–1244.
156. Fiaschetti V, Pistolese CA, Funel V, et al. Breast MRI artefacts: evaluation and solutions in 630 consecutive patients. *Clin Radiol*. 2013;68: e601–e608.
157. Kallenberg M, Petersen K, Nielsen M, et al. Unsupervised deep learning applied to breast density segmentation and mammographic risk scoring. *IEEE Trans Med Imaging*. 2016;35:1322–1331.
158. Petersen K, Nielsen M, Diao P, Karssemeijer N, Lillholm M. Breast tissue segmentation and mammographic risk scoring using deep learning. In: *Breast Imaging*. Berlin: Springer; 2014:88–94.
159. Foteinos PA, Chrisochoides NP. High-quality multi-tissue mesh generation for finite element analysis. In: *Image-Based Geometric Modeling and Mesh Generation*. Berlin: Springer; 2013:159–169.
160. Ji S, Ford JC, Greenwald RM, et al. Automated subject-specific, hexahedral mesh generation via image registration. *Finite Elem Anal Des*. 2011;47:1178–1185.
161. De Santis G, De Beule M, Van Canneyt K, Segers P, Verdonck P, Verhegghe B. Full-hexahedral structured meshing for image-based computational vascular modeling. *Med Eng Phys*. 2011;33:1318–1325.
162. Fedorov A, Chrisochoides N. Tetrahedral mesh generation for non-rigid registration of brain MRI: analysis of the requirements and evaluation of solutions. In: *Proceedings of the 17th International Meshing Roundtable*. Heidelberg: Springer; 2008:55–72.
163. Liu Y, Foteinos P, Chernikov A, Chrisochoides N. Multi-tissue mesh generation for brain images. In: *Proceedings of the 19th International Meshing Roundtable*. Heidelberg: Springer; 2010:367–384.
164. Drakopoulos F, Ortiz R, Enquobahrie A, Sasaki-Adams D, Chrisochoides N. Tetrahedral image-to-mesh conversion software for anatomic modeling of arteriovenous malformations. *Proc Eng*. 2015;124:278–290.
165. CIBC. 2015. Seg3D: Volumetric Image Segmentation and Visualization. Scientific Computing and Imaging Institute (SCI), Download from: http://www.seg3d.org.
166. Rosset A, Spadola L, Ratib O. Osiri X: an open-source software for navigating in multidimensional DICOM images. *J Dig Imaging*. 2004;17:205–216.
167. Haidekker MA. Advanced biomedical image analysis. In: *Image Analysis and Visualization Software*. Hoboken, NJ: John Wiley & Sons; 2011:441–475.
168. Geuzaine C, Remacle J-F. Gmsh: a 3-D finite element mesh generator with built-in pre-and post-processing facilities. *Int J Num Methods Eng*. 2009;79:1309–1331.
169. Institute SCI. 2015. BioMesh3D: Quality Mesh Generator for Biomedical Applications. Scientific Computing and Imaging Institute (SCI).
170. CIBC. 2015. Cleaver: A MultiMaterial Tetrahedral Meshing Library and Application. Scientific Computing and Imaging Institute (SCI), Download from: http://www.sci.utah.edu/cibc/software.html.
171. Grosland NM, Shivanna KH, Magnotta VA, et al. IA-FEMesh: an open-source, interactive, multiblock approach to anatomic finite element model development. *Comput Methods Programs Biomed*. 2009;94:96–107.
172. Allard J, Cotin S, Faure F, et al. SOFA - an open source framework for medical simulation. In: *MMVR 15-Medicine Meets Virtual Reality.* 125: Bristol: IOP Press; 2007:13–18.
173. Maas SA, Ellis BJ, Ateshian GA, Weiss JA. FEBio: finite elements for biomechanics. *J Biomech Eng*. 2012;134:011005.
174. Jacobs F, Sundermann E, De Sutter B, Christaens M, Lemahieu I. A fast algorithm to calculate the exact radiological path through a pixel or voxel space. *J Comput Inf Technol*. 1998;6:89–94.
175. Kohler Th, Turbell H, Grass M. Efficient forward projection through discrete data sets using tri-linear interpolation. In: Nuclear Science Symposium Conference Record, 2000 IEEE, vol. 2; 2000:15–113.
176. Ruijters D, Haar Romeny BM, Suetens P. GPU-accelerated digitally reconstructed radiographs. *BioMED*. 2008;8:431–435.
177. Greef M, Crezee J, Van Eijk JC, Pool R, Bel A. Accelerated ray tracing for radiotherapy dose calculations on a GPU. *Med Phys*. 2009;36:4095–4102.
178. Xu F. Fast implementation of iterative reconstruction with exact ray-driven projector on GPUs. *Tsinghua Sci Technol*. 2010;15:30–35.
179. Pratx G, Xing L. GPU computing in medical physics: a review. *Med Phys*. 2011;38:2685–2697.
180. Markelj P, Tomaževič D, Likar B, Pernuš F. A review of 3D/2D registration methods for image-guided interventions. *Med Image Anal*. 2012;16:642–661.
181. McLaughlin RA, Hipwell J, Hawkes DJ, Noble JA, Byrne JV, Cox T. A comparison of 2D-3D intensity-based registration and feature-based registration for neurointerventions. In: Dohi T, Kikinis R, eds. *International Conference on Medical Image Computing and Computer-Assisted Intervention*. Berlin: Springer; 2002:517–524.
182. Mertzanidou T, Hipwell J, Tanner C, Hawkes D. *An Intensity-based approach to X-ray mammography: MRI registration*. In: SPIE Medical Imaging; 2010:76232Z.
183. Ruiter N. *Registration of X-ray mammograms and MR-volumes of the female breast based on simulated mammographic deformation*. PhD thesis. Universitt Mannheim, Karlsruhe, Germany 2003.
184. Lee Angela WC, Rajagopal V, Chung J-H, Bier P, Nielsen PMF. Biomechanical modelling for breast image registration, In: Proc. of SPIE Vol; 2008:6918:69180U–1.
185. Frey P. *Medit: an interactive mesh visualization software*. PhD thesis, INRIA 2001.
186. Patrick J. Lynch, Medical illustrator, http://patricklynch.net [CC by 2.5, http://creativecommons.org/licenses/by/2.5], via Wikimedia Commons Original authors:
187. http://niftyseg.sourceforge.net
188. http://wias-berlin.de/software/tetgen/
189. http://iso2mesh.sourceforge.net/cgi-bin/index.cgi
190. http://www.cgal.org/
191. http://www.sharc.co.uk/index.htm
192. http://www.3ds.com
193. http://www.ansys.com/
194. http://opencmiss.org/
195. https://sourceforge.net/projects/niftysim/
196. https://www.nist.gov/
197. https://radiopaedia.org/articles/hounsfield-unit

198. http://www.cirsinc.com
199. http://www.itksnap.org/pmwiki/pmwiki.php
200. http://imagej.net/
201. http://www.osirix-viewer.com/
202. http://www.haidekker.org/cimage/
203. http://www.hpfem.jku.at/netgen/
204. http://gmsh.info/
205. https://www.sci.utah.edu/cibc-software/cleaver.html
206. https://www.ccad.uiowa.edu/MIMX/projects/IA-FEMesh
207. A complete review of software options for mesh generation is available on-line at. http://www.robertschneiders.de/meshgeneration/meshgeneration.html
208. https://www.sofa-framework.org/
209. http://febio.org/
210. http://www.paraview.org/
211. http://www.imagemagick.org/
212. http://www.opendx.org/
213. https://people.sc.fsu.edu/ jburkardt/examples/medit/medit.html
214. http://www.mevislab.de/
215. http://www.nvidia.com/
216. http://www.amd.com/
217. https://www.comsol.com/
218. https://es.mathworks.com/matlabcentral/

3

Local breast density assessment using reacquired full-field digital mammograms

This chapter aims to evaluate the spatial glandular tissue distribution as well as the automatic density measures provided by the commercial software Volpara^{TM} Density Maps using a dataset composed of repeatedly acquired full-field digital mammograms, where each pair was acquired in a short time frame. The global measures provided by Volpara^{TM}, such as breast volume (BV), volume of glandular tissue (VGT) and volumetric breast density (VBD), are compared between the two acquisitions. Furthermore, the evaluation of the information is performed using histogram similarity metrics, such as intersection and correlation, and local measures, such as statistics from the difference image and local gradient correlation measures, are used to evaluate the structural similarity.

Title: Local breast density assessment using reacquired mammographic images.
Authors: Eloy García, Oliver Diaz, Robert Martí, Yago Diez, Albert Gubern-Mérida, Melcior Sentís, Joan Martí, and Arnau Oliver.
Published in: European Journal of Radiology, vol. 93, pp 121-127, August 2017.
JCR RNMMI IF: 2.462, Q2(44/127)
DOI: 10.1016/J.EJRAD.2017.05.033

European Journal of Radiology 93 (2017) 121–127

Contents lists available at ScienceDirect

European Journal of Radiology

journal homepage: www.elsevier.com/locate/ejrad

Research paper

Local breast density assessment using reacquired mammographic images

Eloy García[a], Oliver Diaz[a], Robert Martí[a], Yago Diez[b], Albert Gubern-Mérida[c], Melcior Sentís[d], Joan Martí[a], Arnau Oliver[a,*]

[a] Computer Vision and Robotics Institute, University of Girona, Spain
[b] Tokuyama Laboratory GSIS, Tohoku University, Sendai, Japan
[c] Radboud University Medical Center, Nijmegen, The Netherlands
[d] UDIAT – Centre Diagnòstic, Corporació Parc Taulí, Sabadell, Spain

ARTICLE INFO

Keywords:
Breast cancer
Breast density
Image analysis
Volpara™
Mammography

ABSTRACT

Purpose: The aim of this paper is to evaluate the spatial glandular volumetric tissue distribution as well as the density measures provided by Volpara™ using a dataset composed of repeated pairs of mammograms, where each pair was acquired in a short time frame and in a slightly changed position of the breast.

Materials and methods: We conducted a retrospective analysis of 99 pairs of repeatedly acquired full-field digital mammograms from 99 different patients. The commercial software Volpara™ Density Maps (Volpara Solutions, Wellington, New Zealand) is used to estimate both the global and the local glandular tissue distribution in each image. The global measures provided by Volpara™, such as breast volume, volume of glandular tissue, and volumetric breast density are compared between the two acquisitions. The evaluation of the local glandular information is performed using histogram similarity metrics, such as intersection and correlation, and local measures, such as statistics from the difference image and local gradient correlation measures.

Results: Global measures showed a high correlation (breast volume $R = 0.99$, volume of glandular tissue $R = 0.94$, and volumetric breast density $R = 0.96$) regardless the anode/filter material. Similarly, histogram intersection and correlation metric showed that, for each pair, the images share a high degree of information. Regarding the local distribution of glandular tissue, small changes in the angle of view do not yield significant differences in the glandular pattern, whilst changes in the breast thickness between both acquisition affect the spatial parenchymal distribution.

Conclusions: This study indicates that Volpara™ Density Maps is reliable in estimating the local glandular tissue distribution and can be used for its assessment and follow-up. Volpara™ Density Maps is robust to small variations of the acquisition angle and to the beam energy, although divergences arise due to different breast compression conditions.

1. Introduction

Each year in Europe, 500,000 new cases of breast cancer are diagnosed and 143,000 women die from this disease [1]. In order to reduce this mortality, early breast cancer detection is a pivotal step, since its treatment would be less aggressive and more effective [2]. X-ray mammography remains considered the gold standard imaging technique in early disease detection, and is widely used in national screening programmes [3,4]. The latest trends in breast cancer research, however, indicate a willingness to develop a more personalised screening [5].

Volumetric breast density (VBD), among other biomarkers such as diet [6] or physical activity [7], has shown a high correlation with the development of breast cancer and has been established as an important risk factor [8,9]. This has motivated the investigation of women stratification strategies in screening programmes based on breast density.[1] Furthermore, several software tools have been developed to estimate breast density from X-ray mammographic images. These include Volpara™ (Volpara Solutions; Wellington, New Zealand),[2] Quantra™ (Hologic; Danbury, Connecticut, USA)[3] and CumulusV (University of Toronto; Toronto, Canada) among others.

In addition to global measures such as the VBD, the local density

* Corresponding author at: Computer Vision and Robotics Institute, University of Girona, Campus Montilivi, Ed. P-IV, 17071 Girona, Spain.
E-mail address: arnau.oliver@udg.edu (A. Oliver).

[1] ASSURE project: http://assure-project.eu.
[2] http://volparasolutions.com/.
[3] http://www.hologic.com/.

http://dx.doi.org/10.1016/j.ejrad.2017.05.033
Received 11 April 2017; Received in revised form 19 May 2017; Accepted 23 May 2017

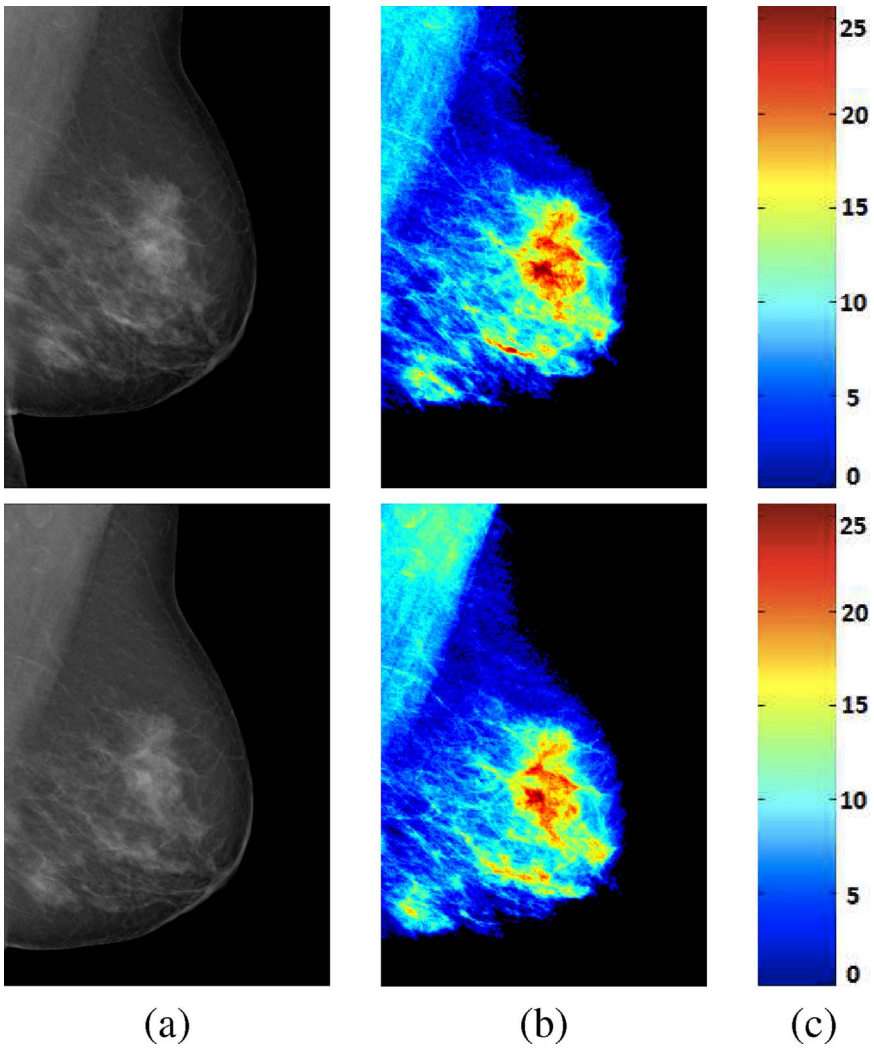

Fig. 1. (a) Mammograms and (b) the corresponding density maps (right). The colour scale in (c) shows the amount of glandular tissue in millimetres. (For interpretation of the references to colour in this figure legend, the reader is referred to the web version of this article.)

distribution and the parenchymal patterns can provide complementary information for risk assessment and disease development [10,11]. However, performing an automatic evaluation of the spatial distribution of the glandular tissue is a challenging task. On one hand, few algorithms provide pixel-wise information about the breast glandularity. On the other hand, several factors, such as the breast compression or temporal changes (aging, involution, hormonal interactions) [12], can modify the appearance of the mammogram as well as the automatic density measures.

The aim of this paper is to evaluate the repeatability of the glandular tissue measures provided by Volpara™ Density Maps (v.1.5.11). Volpara™ uses the physics-based model proposed by Highnam et al. [13] to extract pixel-wise information from the raw mammograms (i.e. "for processing"). Global density measures provided by Volpara™ have already been validated against magnetic resonance imaging (MRI) [14] and computed tomography (CT) images [15]. Furthermore, its reliability has also been investigated, comparing favourably versus a reference standard two-dimensional area-based method [16]. However, few attempts have been performed for evaluating the density maps (*DM*) obtained using this software. As is shown in Fig. 1, the density maps shows the distribution of the dense tissue in the breasts.

Here, we use repeated mammograms for quantitatively assessing the variation of the density maps. To our knowledge, this is the first study analysing the results of Volpara Density Maps using mammograms of the same breast acquired in few minutes of difference. Notice that, in this case, there is not a change in the glandularity of the breast, although several factors, such as different breast compression or different acquisition parameters, can modify the appearance and density measures of the breast.

2. Materials and methodology

The dataset was composed of 99 pairs of mammograms (198 FFDMs in total) from 99 patients, including 56 pairs of CC and 43 pairs of MLO projections. The dataset was acquired between 2008 and 2016 at the Radboud University Medical Center (Nijmegen, The Netherlands) and Hospital Universitari Parc Taulí (Sabadell, Spain). Women were between 30 and 76 years old, and the average age was 52.32 ± 13.61. Regarding the mammographic devices, a GE Senographe (GE Healthcare™; Chicago, USA) was used at the Radboud Medical Center while a Hologic Selenia Dimensions system (Hologic™; Massachusetts, USA) was used at Parc Taulí Hospital.

The FFDMs were acquired for screening purposes of high-risk women, i.e. high familiar or genetic risk in standard clinical settings (e.g. use of an anti-scatter grid and automatic exposure control) and considering the quality assumptions exposed in the European guidelines [17]. In this retrospective study, each image pair corresponded to mammograms acquired within a very short time interval (of few minutes). Mammograms were repeated due to obtaining a suspicious area that prompted the radiologists to slightly change the position of the breast. This is a common procedure in clinical practice, where the goal of the second acquisition is to re-analyse a possible finding that might be due to tissue superposition. This means that the second projection is on purpose a little bit rotated compared to the first. Hence, the patient

breast was released and re-compressed between the two acquisitions, modifying the spatial distribution of the glandular tissue in the projection. Therefore, the two images were in perfect conditions to compute, and compare, the glandularity of the breast obtained using Volpara™.

2.1. Glandular tissue estimation

To extract the glandular tissue from FFDM we use the FDA-approved software Volpara™ v.1.5.11 (Volpara Solutions, Wellington, New Zealand), which is based on a physics-based model. Its principles are described in the work of Highnam et al. [13], as an extension of the method proposed by van Engeland et al. [18].

Briefly, Volpara™ starts by looking for an entirely adipose area within the mammogram. The mean intensity value of this area (P_{fat}) is subsequently used as a reference to estimate the density map $DM(x, y)$, i.e. the thickness of the glandular tissue at each pixel of the mammogram, using the equation:

$$\mathrm{DM}(x, y) = \frac{\ln(P(x, y))/P_{\mathrm{fat}}}{\mu_{\mathrm{fat}} - \mu_{\mathrm{dense}}}, \quad (1)$$

where $P(x, y)$ corresponds to the grey level intensity at pixel (x, y) in the raw mammogram, which is proportional to the X-ray energy absorbed at the image receptor. Key acquisition parameters from the meta-data of the image (e.g. kVp, X-ray tube anode material, filter material, compressed breast thickness) are read from the DICOM header to use the appropriate X-ray linear attenuation coefficients (μ_{fat} and μ_{dense}). As van Engeland et al. [18] exposed, the effective attenuation coefficients, μ_{fat} and μ_{dense}, depend on the anode and filter material, tube voltage and tissue thickness, h_{fat} and h_{dense}. In the proposed algorithm, the breast is considered as composed of adipose and *interesting* (i.e. glandular) tissue [19]. Therefore, h_{fat} is directly computed while h_{dense} is computed as the difference between the breast thickness (H) and the adipose tissue thickness.

Integrating $DM(x, y)$ over the whole mammogram, Volpara™ computes the volume of glandular tissue (VGT). Furthermore, by taking into account the area of the projected breast on the mammogram and the recorded compressed breast thickness, Volpara™ also computes the breast volume (BV). Finally, the ratio between VGT and BV represents the volumetric breast density (VBD). Based on VBD estimated values, Volpara™ returns a number between 1 and 4, i.e. Volpara density grade (VDG), which is comparable to the BIRADS rating for global breast density [20].

2.2. Registration

Mammograms are two-dimensional projections of the breast, which is a three-dimensional body. Small variations in the patient positioning or in the breast compression result in a different localisation of the inner tissues in the mammogram. Hence, a direct subtraction of both images is not a feasible way to compute the similarity between them. In order to minimise these misalignments when comparing the local density maps, we perform a two-dimensional registration of both density maps. Besides, due to the own physics of the acquisition, the differences in the parenchyma localisation vary non-linearly in each part of the image, hence a deformable (or non-rigid) registration should be used to better minimise the misalignments.

Deformable registration algorithms allow to locally deform the mammograms. However, there is not a single registration method which can be considered as a gold-standard. Moreover, it is important to test approaches grounded in different basis [21]. In this work we used morphons [22] and B-Spline SyN [23]. Briefly, morphons [22] is a non-rigid registration method performed in three steps. Firstly, it estimates the local displacement using quadrature phase differences, which are invariant to image intensities and weak gradients, and are used as a measure of the local structures. Afterwards, the local displacement is estimated as a function of the local phase along each direction. Finally, the displacement is accumulated into a total deformation field and regularised, allowing to morph the source image into the target image. On the other hand, B-Spline SyN is the merge of two different families of deformable registration algorithms, the ones based in B-Spline and the ones based in diffeomorphic approaches. The B-Spline registration approach [24] uses a mesh of control points that are deformed using B-Spline interpolation looking for the maximisation of a similarity measure. In contrast, the SyN algorithm [25] is a symmetric image normalisation method that maximises the cross-correlation within the space of diffeomorphic maps, allowing to deal with both small and large deformation problems. The combination of both approaches allows to combine the salient characteristics particularly with respect to large deformations constrained by topological continuities of diffeomorphic registration approaches with the advantages of B-Spline based regularisation, including algorithmic simplicity, good performance, and guaranteed parametric continuity.

2.3. Evaluation

Global and local measures were used to evaluate the glandular estimation obtained by Volpara™. We compute and compare the volume of glandular tissue and global breast density in the two acquisitions. Furthermore, we also compare the similarity of each pair of DM by means of the histogram intersection and correlation. Histograms are computed using unitary bin size, i.e. each bin represents 1 mm glandular tissue thickness.

The histogram intersection [28] computes the similarity between the intensity (i.e. the glandular tissue thickness) distributions of the two images. The intersection value is normalised to obtain a result between 0 (no overlap) and 1 (identical distributions), and is defined as follows:

$$H(I_A, I_B) = \sum_i \min(h_{A,i}, h_{B,i}) \quad (2)$$

where $h_{A,i}$ and $h_{B,i}$ represent the value of the bin i in the histograms corresponding to the image A and B. On the other hand, the histogram correlation [29] of the two images computes the statistical similarity between the amount of glandular tissue computed by the automatic software.

To evaluate the structural similarity of the tissue distribution we computed the statistics of the difference image. Specifically, we used the mean, entropy, and standard deviation from the overlapping region within the difference image to compute the divergence of the local glandular tissue computed by Volpara™. However, even when intensity differences could be small after the registration step, it does not mean the glandular tissue distribution is the same in both density maps. For instance, the Demons algorithm [30] was found to produce very good results in terms of difference images [21]. This may lead us to think that it would also perform well in terms of local tissue measurements. However, the same study showed how the Demons method is prone to producing image artifacts due to unrealistic deformations that may affect the local tissue distribution.

In order to evaluate these artifacts and to get an objective measure of the glandular tissue deformation, further than a visual inspection, we use the gradient correlation to compare the distribution of the tissue. Gradient images are created from both density maps, convolving each image with a Sobel filter. The Sobel method uses the derivative approximation to find edges. In this work, we use the horizontal and vertical 3×3 gradient matrices. Each pixel of a gradient image represents the change in intensity of the same point in its density map in the corresponding direction, allowing to locally evaluate the similarity of both images. The Normalised Cross-Correlation is calculated between both horizontal gradient images and between both vertical gradient images. Gradient correlation summarises the similarity by computing the average of these correlation values.

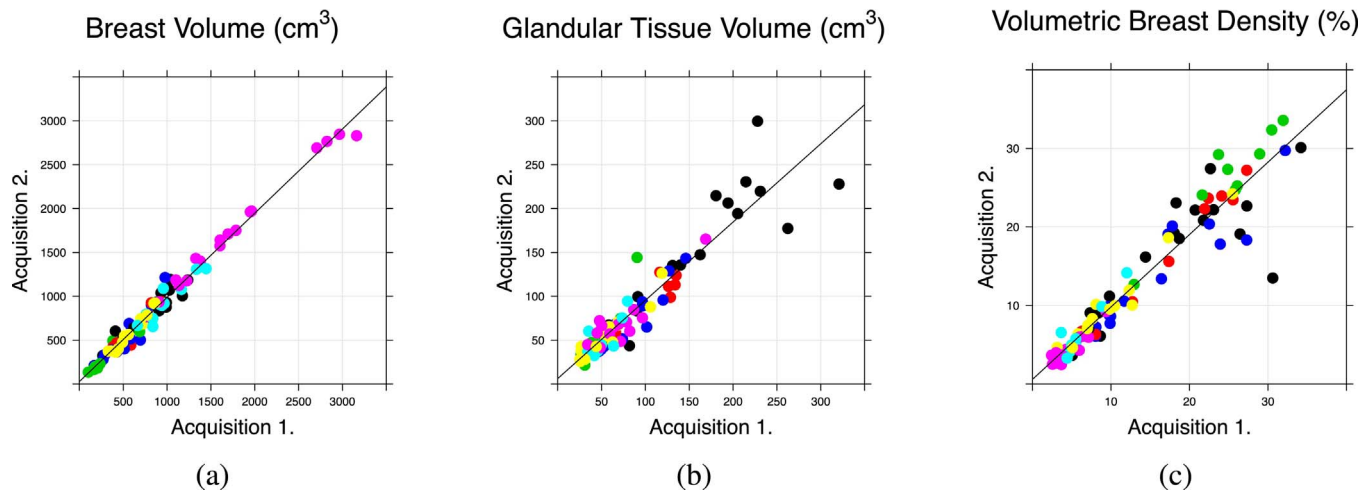

Fig. 2. Comparison of the global measures obtained by Volpara™ when analysing consecutive pairs of mammograms: (a) overall breast volume (R = 0.99 (0.98 − 0.99), slope m = 0.96), (b) glandular tissue volume (R = 0.94 (0.91 − 0.96), slope m = 0.89), and (c) volumetric breast density (R = 0.96 (0.94 − 0.97), slope m = 0.92). In each graph, coloured points show subsets found regarding the anode-filter relationship. The dataset obtained with the GE Senographe machine is split in black (Rh/Rh–Rh/Rh), red (Mo/Rh–Mo/Rh), green (Mo/Rh–Mo/Mo), and blue points (Mo/Rh–Rh/Rh), while the one of Hologic device in purple (W/Ag–W/Ag), yellow (W/Rh–W/Rh), and cyan (W/Ag–W/Rh). (For interpretation of the references to colour in this figure legend, the reader is referred to the web version of this article.)

2.4. Implementation details

The B-Spline SyN combination has been implemented using the Insight Toolkit libraries (ITK v.4.8.0) [26]. Morphons algorithm and the functions to estimate global and local features were implemented in MATLAB v.2013a (The MathWorks Inc., Natick, MA, USA). Finally, data analysis and statistical tests were carried out using the statistical software R (v.3.0.3) [27].

3. Results

3.1. Comparison of global Volpara™ results

We evaluate firstly the global density results obtained by Volpara™. Fig. 2 shows the dispersion plots of the obtained breast volume, glandular tissue volume, and volumetric breast density, where each point represents the values obtained in the two explorations (x-axis represents value obtained in the first acquired mammogram while the y-axis the value obtained in the second one). In all the cases, the Pearson's correlation coefficients are $R \geq 0.94$, while the slope of the linear models are $m \geq 0.89$. In particular, the glandular tissue volume (Fig. 2(b)) obtained correlation coefficient R = 0.94 (0.91 − 0.96) and slope m = 0.89.

Since Volpara™ uses a physics-based model, which computes the amount of glandular tissue using the effective linear attenuation coefficients of the glandular and adipose tissue, the algorithm may be affected by the own mammographic device design. The photon energy spectrum during the mammographic acquisition is related to the anode and filter material, as well as the filter thickness and the tube voltage. The filter and target of the GE Senographe device consist of rhodium (Rh) or molybdenum (Mo), while the target material in the Hologic Selenia system is tungsten (W) and the filter is composed of either Rh or silver (Ag).[4] Some other considerations belonging to each device, such as the distance source-to-detector,[5] may affect to the Volpara™ algorithm, for instance due to the Heel effect. However, we considered that the detectors were calibrated to avoid these inhomogeneities. We performed a detailed analysis considering the anode/filter categorisation, dividing the dataset into 7 categories, where the first 4 categories corresponds to the GE Senographe device while the last 3 provide the information of the Hologic system dataset. Table 1 summarises the information of the corresponding groups. The table shows the mean glandular volume along with the correlation and slope of the fitted regression line. Notice that the correlation was higher than R = 0.90 in all of cases, except for the W/Ag–W/Rh category, where R = 0.81. Furthermore, the slope of the linear models is smaller, $m < 0.90$, when the acquisitions were obtained with the same conditions while $m \geq 0.90$ in those cases acquired under a different combination of target/filter material.

Table 1
Subsets analysis that composes the dataset, divided with respect to the anode and filter material. Number of CC and MLO pairs, mean and std of the glandular tissue volume (cm^3), Pearson's correlation, and the slope of the linear model are shown.

Subset	N	Gland, cm^3	R	m
Rh/Rh–Rh/Rh	20	138.57 ± 82.04	0.91	0.87
Mo/Rh–Mo/Rh	9	91.59 ± 35.78	0.95	0.82
Mo/Rh–Mo/Mo	10	55.07 ± 27.07	0.93	0.99
Mo/Rh–Rh/Rh	18	71.62 ± 31.01	0.93	0.90
W/Ag–W/Ag	17	69.08 ± 28.80	0.91	0.82
W/Rh–W/Rh	14	54.46 ± 28.02	0.95	0.89
W/Ag–W/Rh	11	52.69 ± 18.17	0.81	0.97

In order to globally evaluate the density maps, we compared the histograms of the corresponding pair of density maps using the same categorisation. Fig. 3 shows the intersection and correlation of the histograms with respect to the anode/filter material. The comparison of the density maps shows a high correlation between the information contained in both of them, specially when using the Hologic device. On the other hand, notice also that the median of the boxplots corresponding to those cases acquired under the same combination of materials is higher than those corresponding to those acquired under a different combination, for both the histogram intersection and correlation. However, the results of the Student t-test do not show a statistical significant difference between them.

3.2. Comparison of Volpara™ DM

The local comparison between density maps is performed by means of the registration between them. The better the registration measure,

[4] The filter thickness for Mo and Rh in the GE Senographe device is 30 μm and 25 μm, respectively, while, in the Hologic system, the filter thickness corresponds to 50 μm for both Ag and Rh.

[5] The distance source-to-detector corresponds to 660 mm in the GE Senographe and 700 mm in the Hologic system.

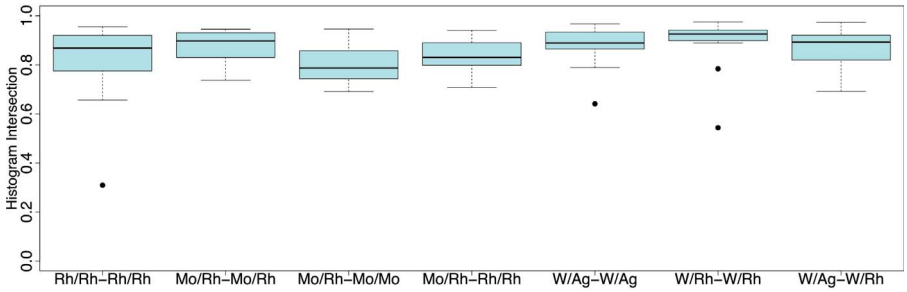

(a) Histogram Intersection.

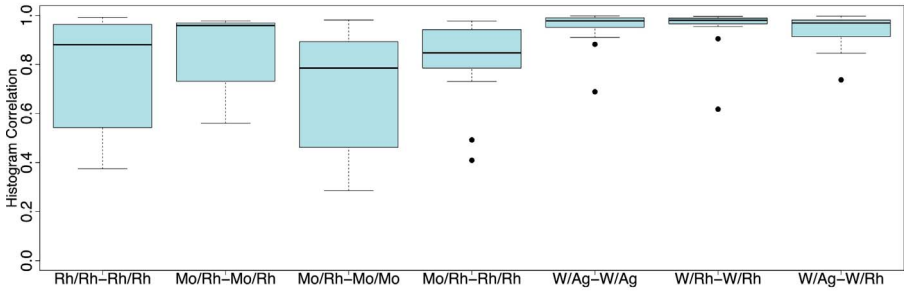

(b) Histogram Correlation.

Fig. 3. Histogram intersection (a) and histogram correlation (b) between density maps.

the higher the structural similarity between the density maps obtained by Volpara™. Specifically, a lower mean of the difference image (MDI) and a higher gradient correlation (GC) imply a better similarity between density maps. Registration methods produced a statistically significant improvement with respect the original position of the density maps (p-value $p < 0.001$). Also, the non-rigid registration methods used (morphons and B-Spline SyN) outperformed the registration obtained with an affine registration ($p < 0.001$).

For a deeper evaluation of the similarity of the density maps we evaluate how the anode/filter and the breast thickness affect the results. Regarding the pair anode/filter used, we divide again the dataset although we only show now two groups: when the pair anode/filter is the same in both projections (Rh/Rh–Rh/Rh, Mo/Rh–Mo/Rh, W/Ag–W/Ag and W/Rh–W/Rh) or when the anode/filter is different (Mo/Rh–Rh/Rh, Mo/Rh–Mo/Mo and W/Ag–W/Rh). Similar results were obtained for individual material cases. Fig. 4 shows the MDI and GC results before and after registration. Significant differences could not be observed between the two anode/filter groups. However, notice here the different behaviour of registration algorithms, where the combined B-Spline SyN outperforms morphons according to the intensity-based measure while the behaviour is the opposite according to the gradient-based measure.

In contrast with global volumetric measures, when computing the local density maps, the breast thickness may modify the density maps values. This is due to the fact that breast thickness varies along the breast, falling off in the periphery of the breast, and hence a different compression of the breast can produce a divergence in these regions. Moreover, small divergences in breast thickness may yield large variations in the glandular tissue thickness due to the fact that effective attenuation coefficients vary with respect to this thickness. To evaluate the performance of Volpara™ regarding breast compression, we divide the dataset according to the following groups: when the difference in both acquisitions is 0–1 mm (no difference), when the difference is 2–5 mm (small difference), when it is 6–10 mm (medium difference), and when the difference is larger than 10 mm (large difference, being 19 mm the maximum difference between both acquisitions). Fig. 5 shows the similarity of the obtained density maps in terms of MDI and GC for the four groups (increasing difference, from left to right). Notice that in this case, there is a relationship between breast thickness and MDI, specially when there is no registration between the density maps. The larger the different compression, the larger the mean difference, which indicates a larger difference in the local glandular tissue. Notice, however, that when using either morphons or B-Spline SyN registration, the final result is almost independent of the breast compression. A similar trend is observed in GC, although the use of morphons registration provided better results than using the B-Spline SyN combination.

Finally, we also analysed the effect of the angle of view and end point energy. No significant differences were found between the obtained density maps, although thirty pairs had differences in angle acquisition varying from 1 to 3 degrees between the two acquisitions. Regarding the end point energy of the spectrum, we found changes between 1 and 4 keV. Considering the correlation shown in Fig. 2, we conclude the kVp does not affect the final result of Volpara™ Density Maps.

4. Discussion

In this work, we evaluated the repeatability of the volumetric density measures and local glandular tissue density map provided by Volpara™ Density Maps using 99 pairs of mammograms acquired in a short time frame. Although the acquisition parameters may differ slightly between acquisitions, we can ensure that the glandular tissue information of the breast remains the same. Hence, we can test how robust is Volpara™ when evaluating the same information but acquired with different acquisition parameters.

We evaluate the global measures obtained by Volpara™, comparing the breast volume, volume of glandular tissue and volumetric breast density between the two acquisitions. Despite the different parameters of both acquisitions, the results show an important agreement. We also compare in a global way the information contained in the density maps using histogram similarity metrics, in particular the histogram intersection and correlation. Both metrics showed a high degree of similarity

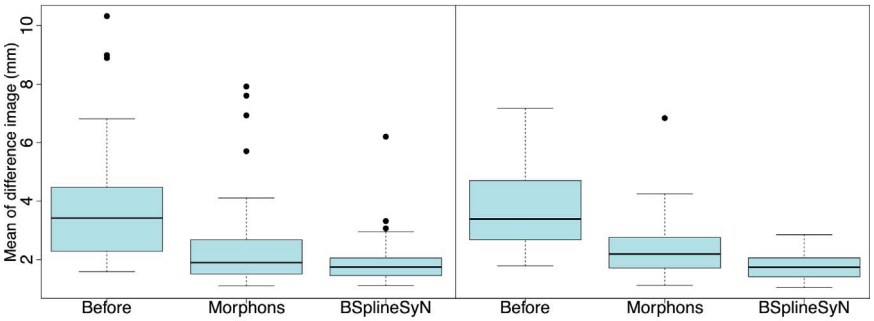

(a) Mean of Difference Image.

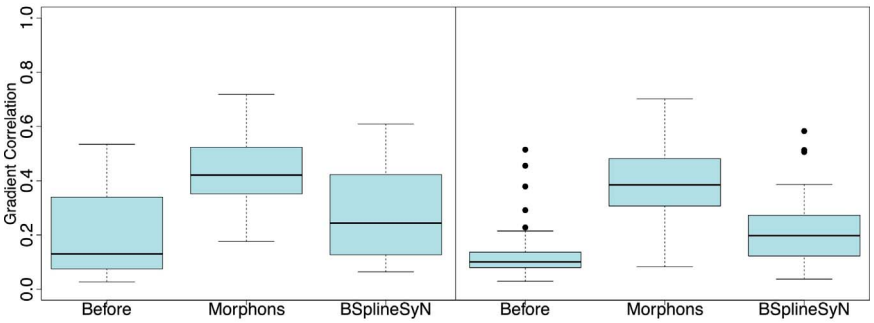

(b) Gradient Correlation.

Fig. 4. (a) Mean of difference image and (b) gradient correlation between density maps without registration and after morphons and B-Spline SyN registration, dividing the dataset regarding the coherence in the anode/filter material. The left box shows the results obtained when both density maps comes from images with acquired with same anode/filter composition whilst the right box shows the result when the anode or the filter changes between acquisitions.

between the information contained in the two density maps. While the histogram intersection was localised above 0.70 in all of the cases, the histogram correlation metric showed a different performance with respect to the mammographic device used, obtaining the Hologic Selenia Dimensions device a better performance. A visual evaluation of the mammograms showed that the differences in positioning, compression, and shape were neglectable in the cases showing the best results.

On the other hand, a direct comparison between the density maps obtained from the two acquisitions showed a high divergence, which is expected due to the different positioning and acquisition parameters. However, deformable registration algorithms allowed us to overcome this issue. The non-rigid registration algorithms used in this work, morphons and the B-Spline SyN, have shown a statistically significant improvement compared to no registration and also to affine registration. Specifically, B-Spline SyN obtained better results in intensity-based features evaluation, while morphons was the best in gradient-based measures. Qualitative results by means of visual inspection, showed that B-Spline SyN produced a higher number of artifacts in

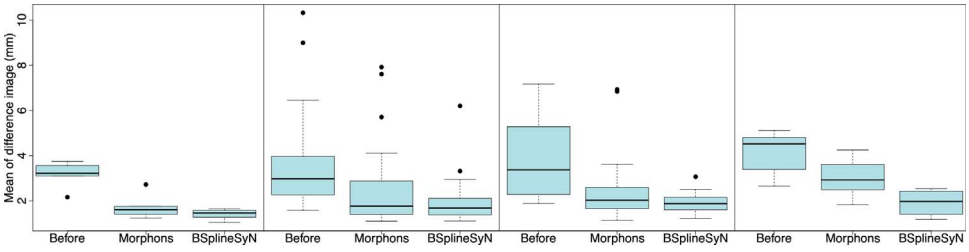

(a) Mean of Difference Image.

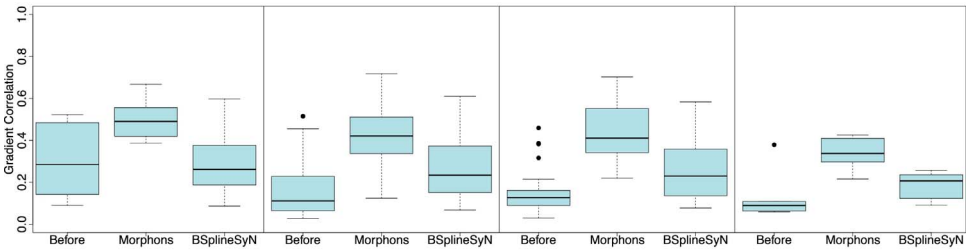

(b) Gradient Correlation.

Fig. 5. (a) Mean of difference image and (b) gradient correlation between images, dividing the dataset regarding the breast thickness difference. The first box (left) correspond with the reference level (0–1 mm). The rest of them are: small (2–5 mm, centre-left), medium (6–10 mm, centre-right) and large (10–19 mm, right) difference.

density maps images compared to morphons.

Differences due to acquisition parameters have been studied considering Pearson's correlation of the glandular tissue volume, similarity between the histogram of the density maps, mean of the absolute difference image and gradient correlation between corresponding density maps. Volpara™ has shown a high reliability in global measures, showing a Pearson's correlation coefficient of $R = 0.94$ in the glandular tissue volume. Regarding the local distribution of the glandular tissue, two factors may affect the behaviour of the Volpara™'s algorithm. On one hand, the mammographic device design – i.e. filter and target material – that define the photon energy spectrum traversing the breast. On the other hand, the breast thickness may affect the final result as a result of computing the effective linear attenuation. Our results show that Volpara™ is not affected by the change of the anode and filter material or the end point energy (i.e. kVp) between the first and second acquisition. However, breast thickness have a clear impact on the glandular tissue distribution. This was also suggested earlier by other authors [31] but using a simple acquisition model (monoenergetic beam and uniform breast thickness), not with clinical data as shown in this paper. Nevertheless, deformable registration algorithms helps to mitigate this effect as shown in Fig. 5.

Notice that a proper dataset to perform a repeatability test would consist on duplicate mammograms with totally identical acquisition conditions. However, obtaining such a dataset would require (i) ensuring that the patients positioning is exactly the same and (ii) patients to be subject to an extra dose of radiation purely for data quality purposes. In contrast, we obtained images retrospectively from a real clinical scenario, where mammograms were repeated due to the presence of suspicious findings. Repeated mammograms due to obtaining artifacts within the image or due to a bad breast placement resulting in misaligned or even in part of the breast outside of the mammogram where discarded for our study. Therefore, in the 99 pairs of mammograms used the patient breast was released and re-compressed between acquisitions and both images were in perfect conditions to be studied using the Volpara™ software. Prospectively acquiring such a dataset should be carefully studied as one would expose patients to an increased radiation dose, being potentially harmful for them. Other non-ionising modalities such as ultrasound or magnetic resonance imaging could be complementary used for similar screening purposes.

To conclude, this paper has evaluated the robustness of Volpara™ Density Maps in repeated mammograms. The main divergences between the density maps computed in both acquisitions are mainly due to the amount of breast compression. However, a posterior deformable registration between the density maps shows that discrepancies can be minimised.

Acknowledgements

This work was partially funded by the Ministry of Economy and Competitiveness of Spain grant under project reference DPI2015-68442-R and by Universitat de Girona by UdG grant MPCUdG2016/022. Eloy Garcıa holds a FPI grant BES-2013-065314. Oliver Diaz is funded by the SCARtool project (H2020-MSCA-IF-2014, reference 657875), a research funded by the European Union within the Marie Sklodowska-Curie Innovative Training Networks.

References

[1] International Agency for Research on Cancer, Globocan 2012, (2016) http://globocan.iarc.fr/Default.aspx.
[2] R. Jong, Breast cancer: the art and science of early detection with mammography, Am. J. Roentgenol. 187 (1) (2006) W142.
[3] L. Tabar, M.F. Yen, B. Vitak, H.H. Chen, R.A. Smith, S.W. Duffy, Mammography service screening and mortality in breast cancer patients: 20-year follow-up before and after introduction of screening, Lancet 361 (9367) (2003) 1405–1410.
[4] S.M. Moss, H. Cuckle, A. Evans, L. Johns, M. Waller, L. Bobrow, Effect of mammographic screening from age 40 years on breast cancer mortality at 10 years' follow-up: a randomised controlled trial, Lancet 368 (9552) (2006) 2053–2060.
[5] J.T. Schousboe, K. Kerlikowske, A. Loh, S.R. Cummings, Personalizing mammography by breast density and other risk factors for breast cancer: analysis of health benefits and cost-effectiveness, Ann. Intern. Med. 155 (1) (2011) 10–20.
[6] M. Tseng, C. Byrne, K.A. Evers, M.B. Daly, Dietary intake and breast density in high-risk women: a cross-sectional study, Breast Cancer Res. 9 (5) (2007) 1.
[7] M.L. Irwin, E.J. Aiello, A. McTiernan, L. Bernstein, F.D. Gilliland, R.N. Baumgartner, K.B. Baumgartner, R. Ballard-Barbash, Physical activity, body mass index, and mammographic density in postmenopausal breast cancer survivors, J. Clin. Oncol. 25 (9) (2007) 1061–1066.
[8] N. Boyd, L. Martin, M. Yaffe, S. Minkin, Mammographic density and breast cancer risk: current understanding and future prospects, Breast Cancer Res. 13 (6) (2011) 223.
[9] J.J. Heine, P. Malhotra, Mammographic tissue, breast cancer risk, serial image analysis, and digital mammography: Part 1. Tissue and related risk factors, Acad. Radiol. 9 (3) (2002) 298–316.
[10] E. Sala, R. Warren, J. McCann, S. Duffy, N. Day, R. Luben, Mammographic parenchymal patterns and mode of detection: implications for the breast screening programme, J. Med. Screen. 5 (4) (1998) 207–212.
[11] J.N. Wolfe, Risk for breast cancer development determined by mammographic parenchymal pattern, Cancer 37 (5) (1976) 2486–2492.
[12] J.J. Heine, P. Malhotra, Mammographic tissue, breast cancer risk, serial image analysis, and digital mammography: Part 2. Serial breast tissue change and related temporal influences, Acad. Radiol. 9 (3) (2002) 317–335.
[13] R. Highnam, M. Brady, M. Yaffe, N. Karssemeijer, J. Harvey, Robust Breast Composition Measurement-Volpara™, IWDM Digital Mammography 2010, Springer, 2010, pp. 342–349.
[14] A. Gubern-Mérida, M. Kallenberg, B. Platel, R. Mann, R. Martí, N. Karssemeijer, Volumetric breast density estimation from full-field digital mammograms: a validation study, PLOS ONE 9 (1) (2014) e85952.
[15] O. Alonzo-Proulx, N. Packard, J. Boone, A. Al-Mayah, K. Brock, S. Shen, M. Yaffe, Validation of a method for measuring the volumetric breast density from digital mammograms, Phys. Med. Biol. 55 (11) (2010) 3027.
[16] O. Alonzo-Proulx, G. Mawdsley, J. Patrie, M. Yaffe, J. Harvey, Reliability of automated breast density measurements, Radiology 275 (2) (2015) 366–376.
[17] EUREF European Guidelines for Quality Assurance in Breast Cancer Screening and Diagnosis, 4th ed., (2006).
[18] S.V. Engeland, P. Snoeren, H. Huisman, C. Boetes, N. Karssemeijer, Volumetric breast density estimation from full-field digital mammograms, IEEE Trans. Med. Imaging 25 (3) (2006) 273–282.
[19] R. Highnam, M. Brady, Mammographic Image Analysis, Springer Science & Business Media, 1999.
[20] C. Damases, P. Brennan, C. Mello-Thoms, M. McEntee, Mammographic breast density assessment using automated volumetric software and breast imaging reporting and data system (BIRADS) categorization by expert radiologist, Acad. Radiol. 23 (1) (2015) 70–77.
[21] Y. Diez, A. Oliver, X. Lladó, J. Freixenet, J. Martí, J.C. Vilanova, R. Martí, Revisiting intensity-based image registration applied to mammography, IEEE Trans. Inf. Technol. Biomed. 15 (5) (2011) 716–725.
[22] A. Wrangsjö, J. Pettersson, H. Knutsson, Non-rigid registration using morphons, Image Analysis, Springer, 2005, pp. 501–510.
[23] N.J. Tustison, B.B. Avants, Explicit B-spline regularization in diffeomorphic image registration, Front. Neuroinform. 7 (2013) 39.
[24] D. Rueckert, P. Aljabar, R. Heckemann, J. Hajnal, A. Hammers, Diffeomorphic registration using B-splines, Medical Image Computing and Computer-Assisted Intervention, MICCAI 2006, Springer, 2006, pp. 702–709.
[25] B. Avants, C. Epstein, M. Grossman, J. Gee, Symmetric diffeomorphic image registration with cross-correlation: evaluating automated labeling of elderly and neurodegenerative brain, Med. Image Anal. 12 (2008) 26–41.
[26] L. Ibanez, W. Schroeder, L. Ng, J. Cates, The ITK Software Guide, Kitware, Inc. and The Insight Software Consortium, 2003, http://www.itk.org/.
[27] R Core Team, R: A Language and Environment for Statistical Computing, R Foundation for Statistical Computing, Vienna, Austria, 2014http://www.R-project.org/.
[28] M.J. Swain, D.H. Ballard, Color indexing, Int. J. Comput. Vis. 7 (1991) 11–32.
[29] S.H. Cha, Comprehensive survey on distance/similarity measures between probability density functions, Int. J. Math. Models Methods Appl. Sci. 4 (1) (2007) 300–307.
[30] T. Vercauteren, X. Pennec, A. Perchant, N. Ayache, Diffeomorphic demons: efficient non-parametric image registration, NeuroImage 45 (2009) 61–62.
[31] L. Blot, R. Zwiggelaar, A volumetric approach to glandularity estimation in mammography: a feasibility study, Phys. Med. Biol. 50 (4) (2005) 695–708.

4

Multimodal breast parenchymal patterns correlation using a patient-specific biomechanical model

This chapter aims to compare the breast parenchymal distributions (i.e. density maps) obtained from FFDM and MRI. To achieve this goal, we have developed a fully automatic framework, which registers MRI volumes to X-ray mammograms using a subject-specific biomechanical model of the breast. The optimization step modifies the position, orientation and elastic parameters of the breast model to perform the alignment between the images. When the model reaches an optimal solution, the MRI glandular tissue is projected and compared to the one obtained from the corresponding mammograms. To reduce the loss of information during the ray-casting, we introduce a new approach that avoids resampling the MRI volume. In the results we focus our efforts on evaluating the agreement of the distributions of glandular tissue, the degree of structural similarity and the correlation between the real and synthetic density maps.

Title: Multimodal breast parenchymal patterns correlation using a patient-specific biomechanical model.
Authors: Eloy García, Yago Diez, Oliver Diaz, Xavier Lladó, Albert Gubern-Mérida, Robert Martí, Joan Martí, and Arnau Oliver.
Published in: IEEE Trans. on Medical Imaging, vol. PP, issue 99, pp 1-1, September 2017. JCR RNMMI IF: 3.942, Q1(17/127)
DOI: 10.1109/TMI.2017.2749685

Multimodal breast parenchymal patterns correlation using a patient-specific biomechanical model.

Eloy García, Yago Diez, Oliver Diaz, Xavier Lladó, Albert Gubern-Mérida,
Robert Martí, Joan Martí, Arnau Oliver

***Abstract*—In this paper we aim to produce a realistic 2D projection of the breast parenchymal distribution from a 3D breast magnetic resonance image (MRI). To evaluate the accuracy of our simulation, we compare our results with the local breast density (i.e. density map) obtained from the complementary full-field digital mammogram. To achieve this goal, we have developed a fully automatic framework which registers MRI volumes to X-ray mammograms using a subject-specific biomechanical model of the breast. The optimization step modifies the position, orientation and elastic parameters of the breast model to perform the alignment between the images. When the model reaches an optimal solution, the MRI glandular tissue is projected and compared to the one obtained from the corresponding mammograms. To reduce the loss of information during the ray-casting, we introduce a new approach that avoids resampling the MRI volume. In the results we focus our efforts on evaluating the agreement of the distributions of glandular tissue, the degree of structural similarity and the correlation between the real and synthetic density maps. Our approach obtained a high structural agreement regardless the glandularity of the breast, whilst the similarity of the glandular tissue distributions and correlation between both images increase in denser breasts. Furthermore, the synthetic images show continuity with respect to large structures in the density maps.**

***Index Terms*—Breast Cancer, Parenchymal patterns, Cross-modality, Subject-specific biomechanical models.**

I. Introduction

Breast cancer is the most common cancer in women. Each year in Europe, $500,000$ new cases of breast cancer are diagnosed and $143,000$ women die for this disease [1]. Early detection increases the likelihood of overcoming the disease, motivating the implementation of screening programs. X-ray mammography is considered the gold standard imaging technique since it allows detection of abnormalities even before external symptoms (i.e. lumps) appear. Volumetric breast density (VBD), among other biomarkers such as diet [2] or physical activity [3], has shown a high correlation with the development of breast cancer and has been established as an important risk factor [4]. Usually, VBD is determined by means of subjective visual measurements from the mammograms, and categorized using the BI-RADS (Breast Imaging Reporting and Data Systems) standard [5]. Several methods, such as feature-based [6], [7], area-based approaches [8], [9] or physic-based models [10], [11], have been proposed to obtain an objective VBD value. However, most of them do not provide quantitative information about the local glandular tissue distribution, which provides complementary information for risk assessment and disease development [12].

In contrast to the methods mentioned above, the physics-based model proposed by Highnam et al. [13], available under commercial license as Volpara^{TM} Density Maps (Volpara Solutions[1]; Wellington, New Zealand), is able to provide the local (pixel-wise) information of the glandular tissue thickness within the mammogram. Furthermore, Volpara^{TM} also computes the total volume of the glandular tissue, obtained by integrating the information obtained from the local density maps over the entire mammogram, and the overall breast volume, obtained using the area of the mammogram and the recorded breast thickness. VBD measures computed by Volpara^{TM} has been validated against computer tomography (CT) [14] and magnetic resonance imaging (MRI) [15]. However, evaluating the correlation of the parenchymal patterns (i.e. local breast density) is a challenging task due to the different information provided by different modalities and also to the breast compression performed during the mammographic acquisition.

Biomechanical models of the breast provide a physical basis to simulate realistic deformations. The breast compression performed during the mammographic acquisition has been studied as an independent problem from a mechanical point of view [16] and as an important part of the multimodal (MRI to X-ray mammography) registration problem. The first attempt to perform the registration between MRI and mammography including a physically realistic compression was performed by Ruiter et al. [17]. The registration consisted in simulating the mammographic compression, while the shape of the deformed model and the circumference of the mammogram were used to estimate the 3D shape of the breast. This approach was later extended by Hopp and Ruiter [18], including the rotation of the breast about the anterior-posterior axis. Similarly, Lee et al. [19], proposed the application of a rigid registration approach *a posteriori*. Solves-Llorens et al. [20] used a B-spline registration, while García et al. [21] extended the previous methods using the Demons algorithm [22]. However, these approaches compressed the breast only once while the real and synthetic images were aligned using a 2D-2D registration algorithm. Moreover, these methods do not consider the real geometry of the problem. The patient positioning, angle of incidence and distance from the breast to the X-ray beam

E. García, O. Diaz, X. Lladó, R. Martí, J. Martí and A. Oliver. Institute of Computer Vision and Robotics, University of Girona. Corresponding author: E. García, Ed. P-IV, Campus Montilivi, University of Girona, 17071 Girona (Spain).

Y. Diez, Tokuyama Laboratory GSIS, Tohoku University, Japan

A. Gubern-Mérida, Radboud University Medical Center, Nijmegen, The Netherlands

[1]http://volparasolutions.com/

source vary the projected tissue distribution. In that case, 3D-2D registration methods perform better the requirements of simulating the physics of the transformation. Hopp et al. [23] introduced an intensity-based registration approach which consisted in optimizing a number of parameters, such as position and orientation of the model, to adapt the registration process to the patient-specific conditions. Similarly, Mertzanidou et al. [24], included the elastic parameters as well as the amount of compression in the optimization while the model is allowed to rotate in the anterior-posterior and superior-inferior axis.

The aim of this paper is to produce a realistic 2D projection of the breast parenchymal distribution from 3D MRI. To evaluate the accuracy of our simulation, our results are compared to the local breast density map obtained from full-field digital mammograms (FFDM). The roots of this work are found in [21], [25]. With respect to these papers, a new methodology is introduced here, using a 3D-2D intensity-based registration algorithm, as well as a new approach to avoid resampling the MRI volume. Furthermore, conversely to [25], the evaluation is performed considering not only the histogram intensity distribution but also local measures such as the structural similarity of the real and synthetic images. To our knowledge, no other work has been published focusing on evaluating the quality of the image synthesis as well as the correlation between the information provided by the two modalities. Local breast density can provide additional information regarding areas where tumors can be hidden (breast masking risk) or for improved breast cancer risk estimation [26]. Local breast density evaluation opens a new window to clinically represent the amount of breast tissue in a pixel-basis and even, to further evaluate VBD methods such as Volpara by comparing their maps with MRI. Furthermore, the evaluation of the quality of the images may be used to improve multimodal image registration using intensity-based approaches. To achieve this goal, we have developed a fully automatic framework, which consists in building a biomechanical model to register the MRI volume and the density maps obtained from the mammogram. A biomechanical model, built from T1-weighted MR images, is used to carry out the registration between both image modalities, mimicking the mammographic acquisition. Furthermore, to avoid the loss of information after compressing the model, we propose to use a spatial data structure, such as a uniform grid, since this method allows indexing the elements of the compressed biomechanical model in a fast and efficient way. During the ray-casting process, the sampled points along the ray are simultaneously localized in the uncompressed model and the MRI, computing the barycentric coordinates within the elements traversed by the ray. Therefore, the necessary information to synthesize the final image is obtained without modifying the initial MRI volume.

II. Methodology

Inspired by the previous proposed methods to register MRI and X-ray mammograms [23], [24], we have developed a fully automatic 3D-2D intensity-based framework to register MRI volumes and Volpara^{TM} density maps. The mammographic compression is reproduced using a biomechanical model, while this model is allowed to modify its position, orientation and elastic parameters until it reaches an optimal solution. Mutual information is used to compare the synthesized density map and that provided by Volpara^{TM} during the registration. The complete approach used is summarized in Figure 1.

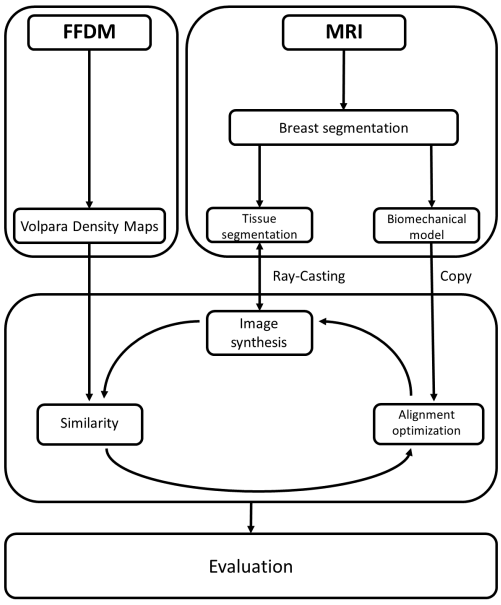

Fig. 1. Scheme of the registration process. Notice that we are using the dense tissue to guide the overall process.

Previous works on synthesizing the mammographic image from other types of data, such as breast phantoms or other image modalities, used a simulation-based approach requiring information related to the acquisition parameters (input energy spectrum), the materials and geometry (compression paddle, anti-scatter grid, detector performance) and other physical phenomena (scattered radiation, focal spot blurring) [27]. In contrast, our approach does not need such image acquisition parameters since it is based on the density maps produced by Volpara^{TM}, i.e. our approach only uses the glandular tissue of the breast.

The following sections provide a detailed description of the registration process from the MRI volume to the synthetic density map.

A. Volpara^{TM} Density Maps

To extract the glandular tissue from FFDM we use the FDA-approved software Volpara^{TM} v.1.5.11. [13]. Briefly, Volpara^{TM} starts by looking for an entirely adipose area within the mammogram. The mean intensity value of this area (P_{fat}) is subsequently used as a reference to estimate the density map $DM(x, y)$, i.e. the thickness of the glandular tissue at each pixel of the mammogram, using the equation:

$$DM(x,y) = \frac{ln(P(x,y))/P_{fat}}{\mu_{fat} - \mu_{dense}}, \quad (1)$$

where $P(x, y)$ corresponds to the gray level intensity at pixel (x, y) in the raw mammogram, which is proportional

to the X-ray energy absorbed at the image receptor. Key acquisition parameters from the meta-data of the image are read from the DICOM header to use the appropriate effective linear attenuation coefficients (μ_{fat} and μ_{dense}). These values depend on the anode and filter material, tube voltage and tissue thickness, h_{fat} and h_{dense}.

B. MRI to Volpara Density Maps registration

1) Geometry extraction: Patient-specific biomechanical models require of an accurate geometrical description of the breast. In this case, the models are built from pre-contrast T1-weighted MR images. Image inhomogeneities and signal intensity variations of the MRI volumes are corrected using the N4 bias field correction algorithm [28]. To separate the breast from the body, the sternum point is automatically localized [29] since it is always visible in centered axial slices of MRI volumes. The utility of the sternum point is twofold. On one hand, it is used as an important landmark in the rigid registration performed during the internal organs segmentation. On the other hand, the sternum point allows locating a coronal plane 2 cm posterior to this position. The structures posterior to this plane are removed, delimiting the depth of the tail of Spence within the biomechanical model, which will be visible in the projections. In the density maps, the pectoral muscle presented in the medio lateral oblique (MLO) projections is removed using the algorithm proposed by Kwok et al. [30] and, usually, a part of the tail of Spence, overlapping the pectoral muscle, is also removed. The first row of Figure 2 shows an example of the mammogram and its corresponding density map with and without the pectoral muscle.

A probabilistic atlas approach, which contains spatial information of the pectoral muscle, lungs, heart, thorax and breast tissue, is used in the MRI volumes to exclude the body from the breast, while the background of the image is segmented using a region growing algorithm. The breasts are separated each other using the box-shape volume of interest in which the sternum has been localized [29]. For each breast independently, the upper and lower boundaries are identified by detecting the superior and inferior points with maximum curvature of the central sagittal slice of the breast.

Once the breast volume is defined, the breast mask is used to carry out two different tasks. First, it is used to isolate the breast and, therefore, the internal tissues. A morphological dilation filter is performed on the background segmentation to remove skin voxels within the mask. Internal tissues of the breast are segmented using an Expectation-Maximization (EM) algorithm that defines a Gaussian-mixture model with Markov random fields (MRF) regularization to provide spatial consistency to the Gaussian model [31]. The inclusion of spatial information allows reducing the number of misclassified voxels [25]. A distinctive feature of this approach is that we consider partial volumes, using the likelihood of belonging to the glandular tissue class and obtaining a 3D density probability map of the whole MRI volume, as shown in the second row of Figure 2. Second, the breast mask is resampled to isotropic voxels of 3.5 mm length to reduce the number of triangular elements on the surface mesh. The surface mesh, as well as the glandular tissue surface, are extracted using the marching cubes algorithm [32]. Nodes belonging to the breast-body interface are automatically selected, using morphological filters and logical operations, and are fitted to a linear surface [24]. To improve the surface mesh quality, local topological operations, such as the elimination of short edges and small triangles, are performed. Furthermore, low- and high-neighborhood nodes are fixed or removed. Finally, the mesh is smoothed using a Lagrangian smoothing process [33]. Due to the resampling process as well as the mesh smoothing, small divergences are expected in the breast shape. However, these variations are localized in the skin region and they do not have a big impact in the glandular tissue projection. Furthermore, the compression of the breast is optimized during the registration (Section II-B3) to compensate errors yielded during the geometry extraction. The volume mesh is extracted using the open-source package TetGen[2] [34]. Since we are essentially working on images, a maximum volume criterion is used to generate the tetrahedral elements. This criterion is related to the voxel volume in the image by a ratio of 10 to 20. Therefore, the number of elements varies from $50,000$ to $500,000$ depending on the breast volume. This number is large enough to minimize the numerical error during the finite element simulation [35].

2) Finite Element Analysis: During mammographic acquisition, the breast is highly compressed. This large deformation of the breast must be simulated using a dynamic approach. This process consists of performing the compression of the model using a large number of small steps. During this work, each compression is divided into $20,000$ small stepss to preserve the stability of the finite element (FE) analysis within the interval of the elastic parameters (see Section II-B3), based on previous experiments [36].

Some considerations, physiological and practical, need to be taken into account for a suitable simulation. For instance, during the mammographic acquisition, the radiographer places the patient's breast on the support, trying to cover the maximum possible breast area to visualize all possible lesions. Then, the breast is compressed. The importance of the manual interaction of the radiographer has not been previously evaluated. Therefore, we assume that the breast is stretched out enough during the MRI acquisition, due to the patient positioning and by the effect of gravity, defining this as the reference state (an idealized assumption) suitable for our simulation.

The mechanical behavior -i.e. stress-strain relationship- of the breast is defined assuming a non-linear behavior [37], using a nearly incompressible, homogeneous and isotropic hyperelastic Neo-Hookean material model for each tissue, assuming both glandular and adipose tissues. The constitutive elastic values used, Young's modulus and Poisson's ratio, are described in section II-B3. Skin and gravity are not considered due to the small effect that they have in the simulation [24].

Regarding the boundary conditions of the biomechanical model, from an anatomical point of view, the breast is not rigidly fixed to the body. They are joint by means of connective tissue, allowing the breast to slightly slide along the thorax.

[2]http://wias-berlin.de/software/tetgen/

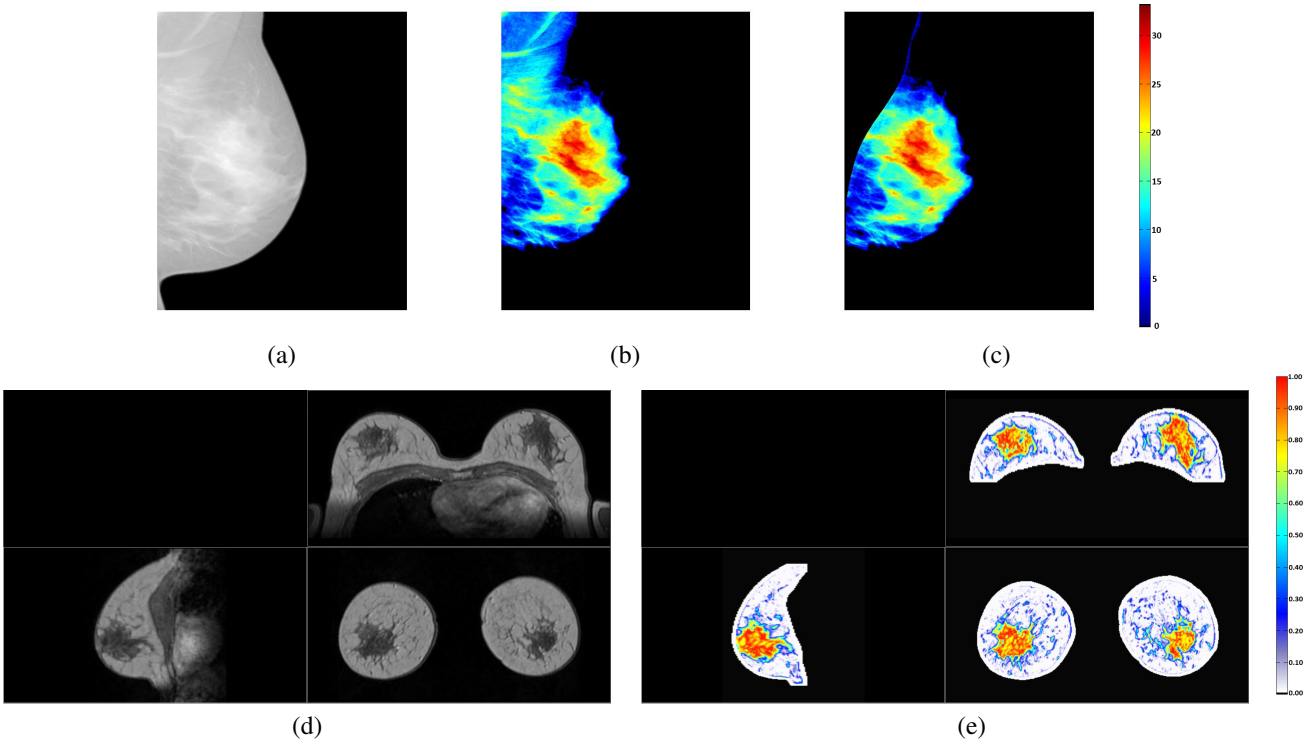

Fig. 2. The first row shows (a) the mammogram and its corresponding density map (b) with and (c) without pectoral muscle. The colors represent the thickness of glandular tissue in millimeters (attached bar). The second row shows (d) the MRI and (e) the corresponding probabilistic segmentation of the glandular tissue. As in the mammographic density map, the blue color represents a low likelihood of belonging to the glandular tissue class while the highest probability is displayed in red. The white area represents the breast mask (attached bar).

Therefore, nodes belonging to the breast-body interface are allowed to slide in the parallel direction to the displacement of the paddles [24]. Furthermore, the compression paddles are explicitly defined using the parametric equation of the plane. As the pectoral muscle and internal organs have been removed, the paddle position with respect to the thorax is not considered and, therefore, the whole breast model is compressed. The contact between the biomechanical model and paddles is defined using a frictionless contact model.

In this work, the FE analysis is performed using NiftySim^{TM} [38] (University College London[3]). NiftySim^{TM} solves the Total Lagrangian Explicit Dynamic (TLED) FE formulation proposed by Miller et al. [39] for soft-tissue simulations.

3) Optimization and mechanical properties: The elastic parameters, as well as the position and the orientation of the breast model, are optimized using the Simulated Annealing algorithm [40]. The optimization consists in finding the maximum agreement between the real and synthetic density maps, using Mutual Information (MI). In this work we assume the implementation proposed by Mattes et al. [41]. The defined parameters to optimize the alignment are:

- Position: translation of the model along a plane parallel to the mammogram.
- Orientation: the model is allowed to rotate around its principal axes, describing this movement by means of Euler angles, using the notation Roll-Pitch-Yaw (RPY).
- Elastic parameters: in this case, the Young's modulus and Poisson's ratio of both adipose and glandular tissues.
- Amount of compression: the breast thickness.

Eventually, uncompressed and compressed models of the breast are available. The former relates the physical space of the MRI volume while the compressed model is localized above the space defined by the mammogram. The main reason to allow optimizing the compression is to compensate errors yielded during the geometry extraction. Hence, the search space of the breast thickness is delimited to variations with respect to the recorded value in the mammogram DICOM header (between 0.75 and 1.25 times this value), which is defined as the starting value during the optimization.

The mechanical properties of living tissues depend of different factors, such as the age of the woman or the menstrual cycle, among other factors. To initialize the elastic parameters of the biomechanical model we use the measures obtained by Wellman [42]. Therefore, the starting values of Young's modulus are $E_{fat} = 4.46\ kPa$ for adipose tissue and $E_{gland} = 15.1\ kPa$ (3.39 times E_{fat}) for glandular tissue at Strain$= 0.0\%$. The search space of these parameters is defined as follows: E_{fat} is ranged between $1\ KPa$ and $10\ KPa$, meanwhile E_{gland} is determined by optimizing the ratio between both values, ranged from 1 to 10 times E_{fat}. The Poisson's ratio is initialized with value $\nu = 0.495$ and is allowed to vary between 0.45 and 0.499, being the same for both adipose and glandular tissues during the optimization.

[3]https://sourceforge.net/projects/niftysim/

Finally, the initial position of the biomechanical model is determined by locating the breast mask centroid on the breast centroid in the mammogram. Furthermore, when MLO projections are simulated, the pectoral muscle is also used as a reference to situate the model, computing the angle between the pectoral muscle segmentation and the edge of the mammogram. The search space of the position is determined by the size of the mammogram. Moreover, the model orientation is initialized using the DICOM tags header. For the left (right) breast, the model rotates counter-clockwise (clockwise) from the primary angle recorded, allowing the use of the axis-oriented bounding box of the model to situate the compression plates. During the optimization, Euler angles are limited to small variations ($[-15, 15]$ degrees) with respect to the reference state. The simulated annealing algorithm stops after 50 simulations without improvement from the last maximum MI value.

4) Glandular tissue projection: Once the biomechanical model is compressed, mimicking the mammographic acquisition, internal tissues of the breast are projected into a 2D space using a perspective ray-tracing algorithm to simulate the X-ray beam. Computing the amount of glandular tissue is performed integrating the values of the probabilistic segmentation along the corresponding ray, using a Newton-Cotes approach [43]. Formally, this method is expressed as follows:

$$\int_a^b f(x)\ dx \approx \frac{b-a}{N} \sum_{i=0}^{i=N-1} f(x_i) = h \sum_{i=0}^{i=N-1} f(x_i) \qquad (2)$$

where a is the initial point, corresponding to the X-ray beam source point, and b is the final point, corresponding to the detector. The source point is situated in the center of the corresponding side of the mammogram, while the bottom plane of the biomechanical model corresponds to the physical position where the synthetic image is created. The distance between the point source and the image receptor corresponds to the distance source-to-detector recorded in the mammogram DICOM header. h represents the step length and the position x_i of the point i belonging to the ray is computed using the parametric equation of the line. A line clipping algorithm, based on the work developed by Siddon [44], is used to reduce the computational cost using the portion of the line within the bounding box of the compressed model. Finally, N is the number of points along the ray and $f(x_i)$ represents the likelihood of belonging to the glandular tissue class at the point x_i.

Usually, the original MRI is deformed using the deformation field computed from the biomechanical model [17]. However, to our knowledge, there is not a criterion to establish an optimal resolution of the compressed breast image to preserve the information of the MRI. Since the mechanical model is composed of two different tissues, the internal behavior is region dependent. Therefore, highly compressed regions may require a different sampling approach than the rest of the model, to synthesize a 3D compressed image. Furthermore, varying the relative Young's modulus of the constituent tissues of the breast can have a significant impact of the 3D deformation [45]. To avoid resampling the 3D volume, we propose using spatial data structures, such as the uniform grid. Specifically, we adapt the work introduced by Lagae et al. [46] to index the elements of the biomechanical model. Hence, computing the barycentric coordinates within the elements traversed by the ray, the position of the sampled points along the ray can be simultaneously localized in the compressed model and the MRI. Notice that computing the barycentric coordinates is not an interpolation but a transformation from the world system of reference $[x, y, z]$ to the internal system of reference of the model, represented by $[E, b] = [E, b_1, b_2, b_3, b_4]$ where E is the index of the element and $b = [b_1, b_2, b_3, b_4]$ the barycentric coordinates. Each point in the physical space is represented by only one vector $[E, b]$ and vice versa.

To localize a given path within the MRI volume, for each sampled point along the ray's path, the corresponding voxel in the grid is computed from its physical position. For each element belonging to the voxel, the barycentric coordinates are computed. If the point is inside the element, the barycentric coordinates are used to localize the position in the uncompressed model. Thus, all points belonging to one ray in the compressed model are moved to the uncompressed model, obtaining a curve in the MR segmentation. Trilinear interpolation is used to compute the glandular tissue value $f(x_i)$ at the corresponding point in the initial MRI and this value is applied to evaluate the integral expression. Notice that we are comparing just the amount of glandular tissue computed by Volpara^{TM} and that value obtained by our methodology. Therefore, only geometrical considerations are extracted from the DICOM header while other tags, such as kVp, filter and anode material, are not needed to obtain the synthetic image.

C. Density maps comparison

To compare the synthetic density map and that provided by Volpara^{TM}, we focus on evaluating the distribution of the amount of glandular tissue, the degree of shape similarity and the correlation between both images. To achieve this goal, we use three different metrics from different fields: Kullback-Leibler Divegence (KLD) from information theory, Structural Similarity Index (SSIM) from the visual perception field and the Normalized Cross-Correlation (NCC) between two images from statistics. These measures provide us different insight on the similarity of the local information of both density maps. On one hand, the KLD aims to evaluate the similarity between the information contained in both the real and synthetic density maps while, on the other hand, SSIM and NCC provide not only information about the glandular tissue thickness in a localized area but also about the structure and parenchymal distribution in the images. The following sections provide a detailed description of the metrics.

1) Kullback-Leibler Divergence: The Kullback-Leibler divergence [47] is a measure of the difference between two probability distributions. Usually, the true distribution, P, represents the distribution of experimental data or empirical results, meanwhile, the simulated distribution, Q, represents a mathematical description or approximation. Therefore, the KLD is the amount of lost information when Q is used to

approximate the P distribution. In this work, P corresponds to the histogram of the density map computed by Volpara^{TM} while Q represents the distribution obtained in the synthetic map. Formally, the KLD is defined as follows:

$$KLD\ (P \mid Q) = \sum_i P_i\ \log \frac{P_i}{Q_i} \tag{3}$$

considering that:

- if $Q_i = 0$, then $P_i = 0$;
- if $P_i = 0$, then, $KLD(P_i \mid Q_i) = 0$

Although the Kullback-Leibler divergence can be used to calculate a distance between two distributions, it is not considered as a metric *per se* because it is not symmetric ($KLD(A|B) \neq KLD(B|A)$), requires defining one of the under-evaluation distributions as a reference, and, hence, it does not obey the triangle inequality ($KLD(A|C) \leq KLD(A|B)+KLD(B|C)$). The KLD is always non-negative as result of Gibbs' inequality [48], and $KLD = 0$ only if the two distributions are the same ($P = Q$). Therefore, the lower the KLD, the higher the agreement between the two distributions, i.e. the breast density histograms.

2) Structural Similarity: The Structural Similarity index [49], widely used in the visual perception area as a quality metric for compressed or modified images, is a measure of the similarity of two images. The structural information is related to the idea that pixels have a strong inter-dependence when they are close to each other. These dependencies provide information about the structure of the objects. Local measures are computed using sliding windows, usually delimited by a Gaussian filter. Hence, being x and y two different windows, statistical features such as luminance (l), contrast (c) and the structural term (s), are computed. Using these terms, the $SSIM(x, y)$ index is computed as follows:

$$SSIM(x, y) = [l(x, y)]^{\alpha} \cdot [c(x, y)]^{\beta} \cdot [s(x, y)]^{\gamma} \tag{4}$$

where,

$$l(x, y) = \frac{2\mu_x\mu_y + c_1}{\mu_x^2 + \mu_y^2 + c_1} \tag{5}$$

$$c(x, y) = \frac{2\sigma_x\sigma_y + c_2}{\sigma_x^2 + \sigma_y^2 + c_2} \tag{6}$$

$$s(x, y) = \frac{\sigma_{xy} + c_3}{\sigma_x\sigma_y + c_3} \tag{7}$$

μ_x and μ_y are the local means of intensity thickness of each window, σ_x and σ_y the local standard deviations and σ_{xy} represents the covariance of the two images. $c_1 = (\kappa_1 L)^2$ and $c_2 = (\kappa_2 L)^2$ are used to stabilize the division with a weak denominator ($\mu_x^2+\mu_y^2 \approx 0$ and $\sigma_x^2+\sigma_y^2 \approx 0$). The terms κ_1 and κ_2 are small constants ($\kappa_1 = 0.01$ and $\kappa_2 = 0.03$ by default) while L represents the dynamic range of the images (for instance, 255 in 8-bits images). In the case of $\alpha = \beta = \gamma = 1$ and $c_3 = c_2/2$ (default values), the overall index is:

$$SSIM(x, y) = \frac{(2\mu_x\mu_y + c_1)(2\sigma_{xy} + c_2)}{(\mu_x^2 + \mu_y^2 + c_1)(\sigma_x^2 + \sigma_y^2 + c_2)} \tag{8}$$

SSIM is ranged between -1 and 1, and $SSIM = 1$ just when both images are identical. Eventually, this algorithm provides a structural similarity map, an example is shown in Figure 3. Notice that the black background obtains always a high SSIM. However, to provide a fair comparison in the results, the average SSIM value is computed considering just the joint region where both the real and synthetic glandular tissue are located, excluding the background of the images.

3) Normalized Cross-Correlation: The Normalized Cross-Correlation [50] is a standard statistical measure used to calculate whether two datasets are linearly related, and represents the 2D version of the Pearson's correlation coefficient. NCC is defined as:

$$NCC = \frac{\sum_{(i,j)}(I_1(i,j) - \bar{I_1})(I_2(i,j) - \bar{I_2})}{\sqrt{\sum_{(i,j)}(I_1(i,j) - \bar{I_1})^2}\sqrt{\sum_{(i,j)}(I_2(i,j) - \bar{I_2})^2}} \tag{9}$$

where $I_1(i, j)$ and $I_2(i, j)$ represent the intensity value (i.e. thickness of glandular tissue) of the pixel (i, j) and $\bar{I_1}$ and $\bar{I_2}$ are the mean intensity values of the images I_1 and I_2, respectively.

D. Implementation Details

Our registration framework was developed in C++, using the Insight Toolkit (ITK v.4.8.0) and the Visualization Toolkit (VTK v.6.1.0) Libraries. Statistics from each pair of images were computed in MATLAB^{TM} (v. R2013b), while data analysis was developed in RStudio (R v.3.0.3). The FE analysis was carried out using the GPU capabilities of NiftySim^{TM}. The time spent by the compression simulation is related to the number of elements composing the model. One single compression spends between 30 seconds, when the model is composed of a small number of elements, and 2 minutes, those with a high number of elements, using 128 threads (default value for NiftySim^{TM}). The ray-casting approach is also carried out using a CUDA implementation, generating an image in less than 1 second using the same number of threads. Therefore, the total computation time for the registration process was between 2 and 5 hours on a workstation Intel Core i7-3770 3.40 GHz, RAM 32 Gb, 64 bits equipped with a GPU NVIDIA GeForce GTX 770 (2 Gb).

III. Experimental results

A. Database

The database used for comparing the density maps was acquired at the Radboud University Medical Centre (Nijmegen, The Netherlands) between April 2005 and March 2011, and contains 50 pre-contrast T1-weighted MR images and 178 mammograms from 42 women. These images corresponded to healthy patients and were acquired for screening purposes. A detailed analysis of the database is shown in Table I, where we divide it according to the BI-RADS categorization (we assume a correlation between the glandular patterns and BI-RADS rating [12]) and the mammographic view (because of geometrical considerations). The patients were aged between 29 and 76 years old (mean: 42.28 ± 8.72).

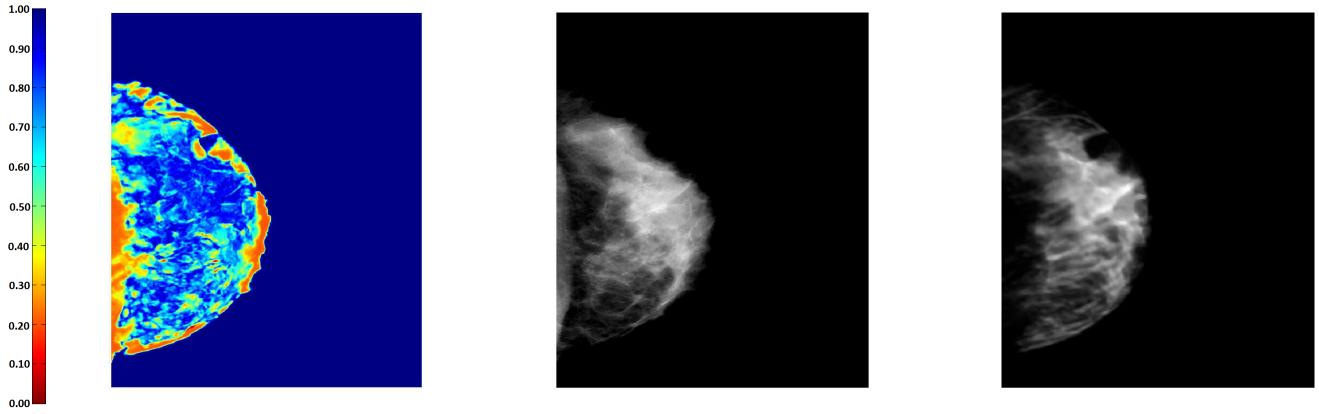

Fig. 3. Structural similarity map (a) between both the real (b) and estimated (c) density map. Blue color represents a high similarity, $SSIM = 1$, while red shows lower similarity degree.

TABLE I
SUBSETS ANALYSIS THE IMAGES COMPOSING THE DATASET, DIVIDED CONSIDERING THE MAMMOGRAPHIC VIEW (CC AND MLO) AND THE BI-RADS CATEGORIZATION.

	BR1	BR2	BR3	BR4
CC	10	11	41	31
MLO	10	9	37	29

The MRI scanner used was a 1.5 Tesla Siemens scanner (Magnetom Vision, Magnetom Avanto and Magnetom Trio) with dedicated breast coil (CP Breast Array, Siemens, Erlangen). MRI volumes had a size of $[512 \times 256 \times 120]$ voxels and $[0.664 \times 0.664 \times 1.300]$ mm^3 a voxel. Regarding the mammographic device, the images were acquired by a GE Senographe, according to the standard clinical settings. Both studies were acquired the same day. Mammograms were composed of $[2294 \times 1914]$ pixels, with $[0.094 \times 0.094]$ mm^2 a pixel. However, the final resolution corresponds to that of the density map. The images provided by Volpara^{TM} had a size of $[765 \times 638]$, obtaining a pixel size (by resampling the original mammography) equal to $[0.282 \times 0.282]$ mm^2 approximately. Our framework uses this information of the density map to simulate the projection.

Besides the main dataset, two other datasets were used in this work. The first one was used to evaluate the overall registration framework and included 10 different cases, each containing 1 MRI volume and 1 mammographic study, composed of both CC and MLO projections (Section III-B2). The second one is used to provide a reference level when comparing locally the density maps, and is composed by 21 pairs of duplicate mammograms from 21 different patients, acquired at Radboud University Medical Center between 2008 and 2010 for screening purposes. Each pair corresponded to mammograms acquired within a very short time interval, few minutes (Section III-C).

B. Evaluation of the framework

1) Volumetric comparison: The aim of this section is to evaluate the probabilistic segmentation, by computing the correlation between the amount of glandular tissue obtained by Volpara^{TM} and that obtained by our MRI density segmentation approach that considers partial volumes, to confirm that the two image modalities contain the same information -i.e. a similar volume of glandular tissue-. Figure 4 compares the amount of glandular tissue computed from both FFDM and MRI. The Pearson's correlation (R) value is 0.95 $(0.93-0.96)$, better than the one reported by Gubern-Mérida et al. [15] ($R = 0.85$) using a binary -glandular vs. adipose tissue- MRI segmentation. The slope of the linear model is $m = 1.16$.

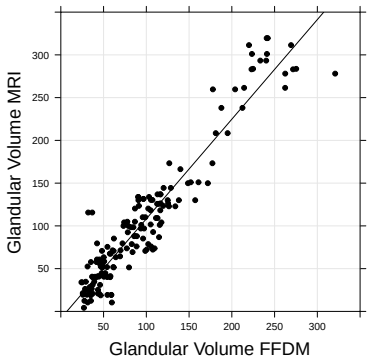

Fig. 4. Comparison of glandular tissue volume, in cm^3, obtained from FFDM, by means of the commercial software Volpara^{TM}, and MRI, using the EM and MRF regularization algorithms.

2) Evaluation of the registration: The evaluation of the registration framework was performed using the target registration error (TRE) measure. To achieve this goal, we used a specific dataset containing lesions that were visible in both modalities, hence the TRE was computed as the Euclidean distance between the centroid of the lesion in the mammogram and the projection of the centroid of the same lesion within the MRI. Regarding the current work, we just aim to provide the reader a reference level of the position of the real and projected parenchymal distribution. Using our registration approach, the mean TRE was 9.90 ± 3.72 mm for CC and 8.04 ± 4.68 mm for MLO projections [51] which is inferior to the values reported

in [23], [24]. Notice that even when the number of cases is in range with most of the previous work, the result may vary using a larger dataset. Ruiter et al. [17] and Solves-Llorens et al. [20] obtained a more accurate TRE but without considering a realistic 3D-2D geometry of the mammographic acquisition.

C. Density maps comparison

Once the the registration framework has been validated, we compared the density maps obtained from the MRI projection and the X-ray mammograms. In order to obtain a reference value we used a dataset, composed by repeated mammograms, where each image pair corresponds to mammograms acquired within a very short time interval. Modifying slightly the position of the breast is a standard approach to confirm or reject the finding of suspicious areas. The two mammograms are similar but the distribution of the glandular tissue slightly varies. Since there is not a physiological change in the tissue between the two acquisitions, these images allow us to obtain a reference value in which the glandular tissue distribution is only affected by the breast compression [52]. For each mammogram, the corresponding density map was extracted using Volpara^{TM} and the two images from the same pair were registered using a rigid approach guided by MI, similarly to our multimodal registration algorithm. The optimization followed a gradient descent approach, while linear interpolation was performed for the pixel interpolation. This registration is needed due to the different patient positioning. For each pair of images, an expert researcher defined the source and target mammograms. Specifically, the image that better met the requirements exposed in the European image quality protocol [53] was defined as the target image. Notice that the results may vary considering the opposite assumption. Nevertheless, we just aim to provide the reader a baseline result regarding the comparison between a density map with either another density map (monomodal registration) or a synthetic density map (multimodal registration). Although we cannot consider the values obtained from this dataset as a proper ground truth, they are useful to report an initial reference level. Therefore, the closer the result of the simulation to this reference level, the more the realistic the image synthesis.

Figure 5 shows the Kullback-Leibler divergence between the histogram thickness of the compared images. The first boxplot corresponds to the monomodal registration (i.e. the comparison between repeated mammograms), while the other four represents the multimodal registration of Volpara^{TM} density maps and the synthetically obtained from the MRI, separated by BI-RADS categories. Each box spans from the first to the third quartile (interquartile range, IQR) and is divided by the median. The whiskers above and below show the locations of the lower and upper 1.5 IQR. Dots represent outliers in the distribution. In general, there is a high agreement between the histograms of the glandular tissue thickness. The best value corresponds to denser breasts, BI-RADS 4, with a value of 0.14 ± 0.10, while images belonging to patients with fatty breasts, BI-RADS 1, show poor results in CC-, 0.44 ± 0.29, but a good performance in MLO-projection, 0.21 ± 0.25. For MLO, the worst performance was observed in BI-RADS 2 images,

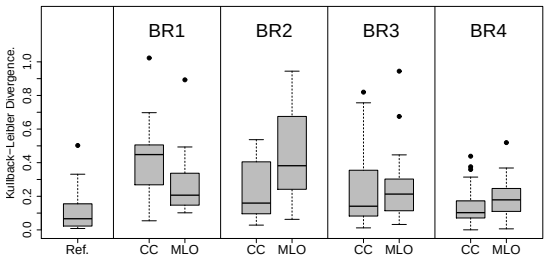

Fig. 5. Kullback-Leibler Divergence analysis. The first boxplot shows the KLD values corresponding to repeated mammograms while the rest show the results of the multimodal registration, divided according to the BI-RADS (BR) density categorization. Notice that the lower the KLD value, the higher the agreement between images.

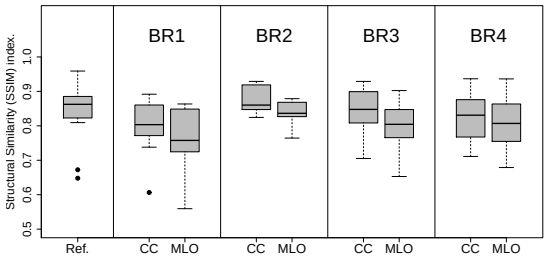

Fig. 6. Analysis of the Structural Similarity Index. The first boxplot shows the SSIM index values corresponding to repeated mammograms while the rest show the results of the multimodal registration, divided according to the BI-RADS (BR) density categorization. Notice that the larger the SSIM index, the higher the agreement between images.

0.45 ± 0.33. We evaluate the significance of the results with respect to the reference, i.e. duplicate mammograms dataset, using the Student's t-test. Only the two worst cases, the CC-projection from BI-RADS 1 and the MLO projection from BI-RADS 2 show a statistical significant difference ($p < 0.01$).

Figure 6 shows the SSIM analysis of the FFDM and MRI density maps. To compute the values, we defined the Gaussian filter with width $w = 5$ pixels, and standard deviation $\sigma = 1.5$. The dynamic range was defined as $L = 55$, since the maximum glandular tissue thickness computed by Volpara^{TM} is 55 mm. The rest of SSIM values were defined as default. Notice that a different behavior is shown using this measure. In all cases the mean is within the interval $[0.76, 0.88]$, reflecting a medium/high agreement. The Student's t-test only shows a significant difference ($p < 0.005$) between the values of the reference and those of the MLO projection in BI-RADS 3.

Finally, Figure 7 shows the correlation between the density maps. The figure shows a similar behavior than the KLD measure, obtaining better results in the densest breasts than in the fatty ones. Regarding the differences with respect to the reference level, all projections in the BI-RADS 1 ($p < 0.001$), 2 and 3 ($p < 0.005$) show a statistical significant difference. Moreover, there is a significant difference ($p < 0.001$) between the results obtained from BI-RADS 1 and the rest of cases. Similarly, images obtained from patients with BI-RADS 4,

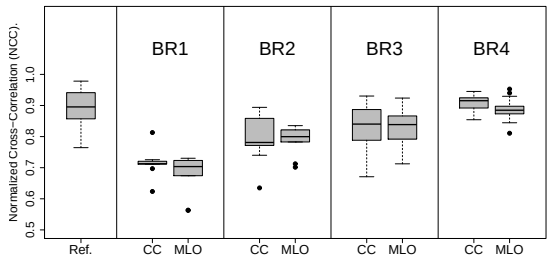

Fig. 7. Normalized Cross-Correlation analysis. The first boxplot shows the NCC values corresponding to repeated mammograms while the rest show the results of the multimodal registration, divided according to the BI-RADS (BR) density categorization. Notice that the higher the NCC, the higher the agreement between images.

have also significant differences ($p < 0.001$) with respect to those obtained from patients belonging to BI-RADS 2 and 3.

D. Visual assessment

After performing the quantitative evaluation of the two images, we carried out a qualitative visual analysis of the obtained density maps. Figure 8 shows (a) the checkerboard of the density maps obtained using (b) VolparaTM and (c) synthetically from the corresponding MRI. The checkerboard corresponds to a mosaic composed using the real and synthetic density maps and it allows the evaluation of the density correspondence, the continuity of the glandular structures, as well as the smoothness in the tissue of both density maps at the border of each square. The more similar the images, the less visible the checkerboard. The patch size was $[60 \times 60]$ pixels ($[16.92 \times 16.92]\ mm^2$), approximately twice the TRE, in order to observe possible discontinuities of the tissue. Notice that an incorrect windowing could either mitigate or exaggerate the differences between the checkerboard patches from the two images.

During this evaluation we observed that the synthetic images show smooth tissue structures. The registration places the model in a suitable position and the glandular tissue is projected in the same (or close) position to the density map structures. Therefore, the densest areas show continuity with respect to the structures in the corresponding density map. Furthermore, those images belonging to BI-RADS 2 and 3 yield a better performance, showing a higher visual similarity than those corresponding to BI-RADS 1 and 4. In BI-RADS 1 patients, the images show a high contrast between the densest areas and those with small amount of glandular tissue. On the other hand, images belonging to the BI-RADS 4 show a poor contrast between the internal structures of the breast.

IV. Discussion

The aim of this paper is to produce a realistic 2D projection of the breast parenchymal distribution from a 3D breast MRI and to compare the obtained result using the local density map extracted from the corresponding FFDM. To achieve this goal, this paper describes a fully automatic registration framework from the MRI volume to the density maps, as well as a new method to avoid resampling the 3D MRI volume. Conversely to previous work, a patient specific modeling is achieved, based on the following novel aspects: i) an anatomical landmark (the sternum point) is used to separate the body from the breast; ii) an improved mesh is extracted, considering the MRI voxel size, to avoid numerical errors during the simulation; iii) a novel ray casting algorithm is proposed, using the glandular tissue value directly from the MRI images; and iv) a constraint free model, the model does not assume any geometrical constraints and all necessary information is obtained from the mammogram DICOM header. Other considerations, such as the automatic segmentation of pectoral muscle in both MRI and mammography, the free orientation of the model and the search space, defined to optimize the simulated annealing search, also add up to the novelty of our framework.

Using our approach, the results show that the information (thickness of glandular tissue) obtained from the two image modalities and compared using the Kullblack-Leibler divergence present a high agreement between them. Furthermore, the structural similarity index provides a statistical comparison between the structures situated in the same area in both images. The obtained results show also a high agreement between both images. These metrics are not common in medical image analysis. However, we consider that they are suitable in this study because of the multimodal nature of this work and the divergence between the pixel size of both image modalities. KLD was previously used to guide the multimodal registration approaches [54] while SSIM is one of the most important and most used index in digital image quality. Synthesizing a medical image from other type of data, in this case another image modality but also from phantoms, must yield a realistic simulation that can be comparable to the real image. Therefore, we use KLD to compare the degree of agreement between the information provided by both image modalities. However, because of the difference between the pixel size of both image modalities, we consider that an area-based approach is better than comparing pixel-wise intensities. This analysis is performed using the SSIM, which involves a sliding Gaussian window, to compare the structural information.

The analysis of NCC values shows divergences considering the breast glandularity. The high correlation between intensity values implies a high agreement between the local breast density computed from the the two image modalities, considering the neighborhood of pixels, the structural analysis is similar. However, NCC contains pixel-wise spatial considerations. Beyond this point, gradient-based features, such as Gradient Difference or Gradient Correlation [55] can provide more detailed information about glandular tissue patterns. Results obtained during this study show small values in gradient correlation (ranged from 0.04 ± 0.01 belonging to CC-projections in the BI-RADS 1, to 0.13 ± 0.03 belonging to CC-projections in BI-RADS 4) and high gradient difference values (ranged from 0.71 ± 0.09 belonging to CC-projections in BI-RADS 4 and 0.78 ± 0.02 belonging to MLO-projections in the BI-RADS 1, using relative values).

The visual assessment shows a high agreement in general,

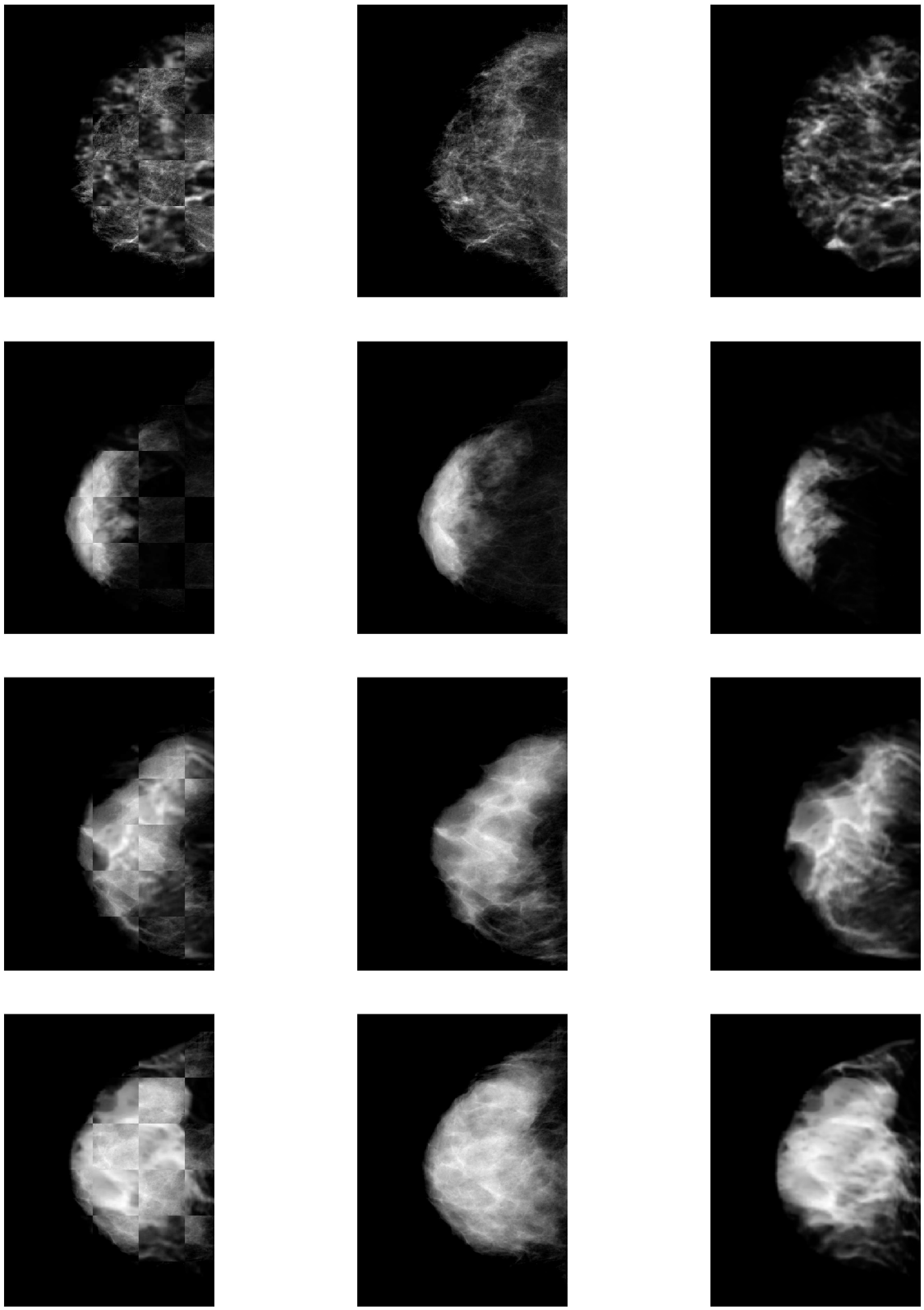

(a) (b) (c)

Fig. 8. (a) Checkerboard mosaic composed of (b) the Volpara^{TM} and (c) the synthetically obtained from MRI images density maps. Each row corresponds to an increasing BI-RADS category, from BI-RADS 1 to 4.

although a different behavior is shown depending on the density grade. Considering the image resolutions of the MRI volumes and Volpara^{TM}, exposed in Section III, the ray-casting sampling produced aliasing errors and, therefore, the smooth structures that have been observed. This error is clearly visible when one of the tissues, glandular or adipose, prevails over the other. However, when there are several defined areas, the larger structures show a continuity with those presented in the original density map. We have concluded that the source of divergences may be:

- The final values of glandular tissue in the synthetic density maps are strongly dependent of the MRI segmentation. Therefore, either the model (probabilistic segmentation) of the glandular tissue does not perfectly fit the real values for each voxel or the trilinear interpolation does not provide an accurate sub-pixel value.
- Differences in resolution and pixel size between both image modalities prevent obtaining more accurate information. Similarly, the internal structures of the breast, such as Cooper's ligaments, blood vessels, nerves or lymph nodes, that are visible in the mammograms but not (or left undetected) in the MRI.
- Considering the TRE obtained in the registration, the scattering patterns corresponding to the BI-RADS 1 and 2 can make difficult to situate the glandular tissue of the synthetic image in the same position of that in the real density map.

Regarding the glandular tissue segmentation, we have localized several source of problems. Images belonging to BI-RADS 1 and 2 are more susceptible of being affected by segmentation issues, such as skin voxels and the presence of the infra-mammary fold and pectoral muscle within the region of the biomechanical model. Images belonging to BI-RADS 3 and 4 are susceptible to the presence not only of the pectoral muscle but also of the axillary tail. While in the mammograms, the pectoral muscle and a part of the axillary tail are removed [30], in MRI, a plane 2 cm behind the sternum point is defined to separate the body from the breast, delimiting the depth of the axillary tail which is visible in the projections. Therefore, for same cases, in the synthetic image this structure is larger than in the mammograms.

Moreover, the biomechanical model extraction, using the marching cubes algorithm, is not a perfect process. Some of the issues introduced in section II-B1 are not perfectly fixed in our implementation. For instance, sharp edges in the biomechanical model affect the finite element analysis and, therefore, the optimization process. When these -from the segmentation and mesh- issues are presented within the model, they can vary the final solution of the synthetic image and, even, the final result of the registration, providing the differences between the statistics form CC and MLO mammograms (CC-projections are more susceptible to segmentations issues, such as the presence of the inframammary fold, while in MLO-projections, the presence of the axillary tail yield worst results) and the outliers presented in the distributions shown in Figures 5-7.

Comparing the glandular tissue obtained from the MRI image with other image modalities may improve the synthesis of parenchymal distribution. For instance, digital breast tomosynthesis (DBT) provides images of the compressed breast that can be projected obtaining 2D pseudo-mammograms. While, so far, this technology is not fully integrated in screening programs, it is gaining relevance in breast disease detection. In future work, we will focus on performing the multimodal MRI-DBT registration. The synthesis and evaluation of the parenchymal pattern distribution between the two image modalities may not only contribute to the MRI-mammography registration, but also increase the accuracy of the biomechanical models, providing detailed information of the internal tissue of the compressed breast.

V. Conclusions.

In this paper, we have compared the parenchymal patterns obtained from full-field digital mammograms and those obtained from magnetic resonance images. This goal was achieved using a fully-automatic framework to register MRI and density maps. Moreover, a fast approach to avoid resampling the MRI volume and reduce the lost of information has been proposed. Based on the experimental evaluation, we conclude that the parenchymal patterns observed from the two modalities share structural information, although some sources of divergences have been identified during our study.

VI. Acknowledgement

This research has been partially supported from the University of Girona (MPC UdG 2016/022 grant), the European Union within the Marie Sklodowska-Curie Innovative Training Networks (SCARtool project H2020-MSCA-IF-2014, ref. 657875) and the Ministry of Economy and Competitiveness of Spain, under project SMARTER (DPI2015-68442-R) and the FPI grant BES-2013-065314.

References

[1] I. A. for Research on Cancer, "Globocan 2012," http://globocan.iarc.fr/Default.aspx, 2016.

[2] M. Tseng, C. Byrne, K. A. Evers, and M. B. Daly, "Dietary intake and breast density in high-risk women: a cross-sectional study," *Breast Cancer Research*, vol. 9, no. 5, p. 1, 2007.

[3] M. L. Irwin, E. J. Aiello, A. McTiernan, L. Bernstein, F. D. Gilliland, R. N. Baumgartner, K. B. Baumgartner, and R. Ballard-Barbash, "Physical activity, body mass index, and mammographic density in postmenopausal breast cancer survivors," *Journal of Clinical Oncology*, vol. 25, no. 9, pp. 1061–1066, 2007.

[4] N. Boyd, L. Martin, M. Yaffe, and S. Minkin, "Mammographic density and breast cancer risk: current understanding and future prospects," *Breast Cancer Res.*, vol. 13, no. 6, p. 223, 2011.

[5] C. D 'Orsi, E. Sickles, E. Mendelson, E. Morris, and et al., *Breast Imaging Reporting and Data System ACR BI-RADS^{TM} Atlas*. American College of Radiology, 2013.

[6] M. G. Kallenberg, M. Lokate, C. H. van Gils, and N. Karssemeijer, "Automatic breast density segmentation: an integration of different approaches," *Physics in Medicine and Biology*, vol. 56, p. 2715, 2011.

[7] A. Oliver, J. Freixenet, R. Marti, J. Pont, E. Pérez, E. R. Denton, and R. Zwiggelaar, "A novel breast tissue density classification methodology," *IEEE Transactions on Information Technology in Biomedicine*, vol. 12, no. 1, pp. 55–65, 2008.

[8] J. W. Byng, N. Boyd, E. Fishell, R. Jong, and M. J. Yaffe, "The quantitative analysis of mammographic densities," *Physics in Medicine and Biology*, vol. 39, no. 10, p. 1629, 1994.

[9] A. Oliver, M. Tortajada, X. Lladó, J. Freixenet, S. Ganau, L. Tortajada, M. Vilagran, M. Sentís, and R. Martí, "Breast density analysis using an automatic density segmentation algorithm," *Journal of Digital Imaging*, vol. 28, no. 5, pp. 604–612, 2015.

[10] S. van Engeland, P. R. Snoeren, H. Huisman, C. Boetes, and N. Karssemeijer, "Volumetric breast density estimation from full-field digital mammograms," *IEEE Transactions on Medical Imaging*, vol. 25, no. 3, pp. 273–282, 2006.

[11] J. A. Shepherd, K. M. Kerlikowske, R. Smith-Bindman, H. K. Genant, and S. R. Cummings, "Measurement of breast density with dual X-ray absorptiometry: Feasibility 1," *Radiology*, vol. 223, pp. 554–557, 2002.

[12] J. N. Wolfe, "Risk for breast cancer development determined by mammographic parenchymal pattern," *Cancer*, vol. 37, pp. 2486–2492, 1976.

[13] R. Highnam, M. Brady, M. J. Yaffe, N. Karssemeijer, and J. Harvey, "Robust breast composition measurement - Volpara^{TM}," *Lecture Notes in Computer Science (IWDM 2010)*, vol. 6136, pp. 342–349, 2010.

[14] O. Alonzo-Proulx, N. Packard, J. M. Boone, A. Al-Mayah, K. Brock, S. Shen, and M. Yaffe, "Validation of a method for measuring the volumetric breast density from digital mammograms," *Physics in Medicine and Biology*, vol. 55, no. 11, p. 3027, 2010.

[15] A. Gubern-Mérida, M. Kallenberg, B. Platel, R. Mann, R. Martí, and N. Karssemeijer, "Volumetric breast density estimation from full-field digital mammograms: A validation study," *PLoS One*, p. e85952, 2014.

[16] J. Chung, V. Rajagopal, P. Nielsen, and M. Nash, "Modeling mammographic compression of the breast," in *Proceeding MICCAI 2008*, vol. 5242, 2008, pp. 758–765.

[17] N. Ruiter, R. Stotzka, T. O. Mller, H. Gemmeke, J. R. Reichenbach, and W. A. Kaiser, "Model-based registration of X-ray mammograms and MR images of the female breast," *IEEE Transactions on Nuclear Science*, vol. 53, no. 1, pp. 204–211, 2006.

[18] T. Hopp and N. Ruitter, "2D/3D registration for localization of mammographycally depicted lesions in breast MRI," *Lecture Notes in Computer Science*, vol. 7361, pp. 627–634, 2012.

[19] A. Lee, V. Rajagopal, T. B. Gamage, A. Doyle, P. Nielsen, and M. Nash, "Breast lesion co-localisation between X-ray and MR images using finite element modelling," *Medical Image Analysis*, vol. 17, pp. 1256–1264, 2013.

[20] J. A. Solves-Llorens, M. Rupérez, and C. Monserrat, "A complete software application for automatic registration of X-ray mammography and magnetic resonance images," *Medical Physics*, vol. 41, no. 8, 2014.

[21] E. García, A. Oliver, Y. Diez, O. Diaz, J. Georgii, A. Gubern-Mérida, J. Martí, and R. Martí, "Comparing regional breast density using full-field digital mammograms and magnetic resonance imaging: A preliminary study." in *Workshop MICCAI-BIA*, 2015, pp. 33–41.

[22] T. Vercauteren, X. Pennec, A. Perchant, and N. Ayache, "Diffeomorphic demons: Efficient non-parametric image registration," *NeuroImage*, vol. 45, no. 1, pp. S61–S72, 2009.

[23] T. Hopp, M. Dietzel, M. Baltzer, W. Kaiser, H. Gemmeke, and N. Ruiter, "Automatic multimodal 2D/3D breast image registration using biomechanical FEM models and intensity-based optimization," *Medical Image Analysis, 17*, pp. 209–218, 2013.

[24] T. Mertzanidou, J.Hipwell, S. Johnsen, L. Han, B.Einben, Z. Taylor, S. Ourselin, H. Huisman, R. Mann, U.Bick, N. Kaissermeijer, and D. J. Hawkes, "MRI to X-ray mammography intensity-based registration with simultaneous optimisation of pose and biomechanical transformation parameters," *Medical Image Analysis*, vol. 18, no. 4, pp. 674–683, 2014.

[25] E. García, A. Oliver, Y. Diez, O. Diaz, A. Gubern-Mérida, X. Lladó, and J. Martí, *Comparison of Four Breast Tissue Segmentation Algorithms for Multi-modal MRI to X-ray Mammography Registration*. Springer International Publishing, 2016, pp. 493–500.

[26] R. R. Winkel, M. Nielsen, K. Petersen, M. Lillholm, M. B. Nielsen, E. Lynge, W. Y. Uldall, and I. Vejborg, "Mammographic density and structural features can individually and jointly contribute to breast cancer risk assessment in mammography screening: a case–control study," *BMC cancer*, vol. 16, no. 1, p. 414, 2016.

[27] P. Elangovan, L. M. Warren, A. Mackenzie, A. Rashidnasab, O. Diaz, D. R. Dance, K. C. Young, H. Bosmans, C. J. Strudley, and K. Wells, "Development and validation of a modelling framework for simulating 2D-mammography and breast tomosynthesis images," *Physics in Medicine and Biology*, vol. 59, no. 15, p. 4275, 2014.

[28] N. Tustison, B. Avants, P. Cook, Y. Zheng, A. Egan, P. Yushkevich, and J.Gee, "N4ITK: Improved N3 bias correction," *IEEE Trans. Medical Imaging*, vol. 29, no. 6, pp. 1310–1320, 2010.

[29] A. Gubern-Mérida, M. Kallenberg, R. M. Mann, R. Marti, and N. Karssemeijer, "Breast segmentation and density estimation in breast MRI: a fully automatic framework," *IEEE journal of biomedical and health informatics*, vol. 19, no. 1, pp. 349–357, 2015.

[30] S. M. Kwok, R. Chandrasekhar, Y. Attikiouzel, and M. T. Rickard, "Automatic pectoral muscle segmentation on mediolateral oblique view mammograms," *IEEE Transactions on Medical Imaging*, vol. 23, no. 9, pp. 1129–1140, 2004.

[31] K. Van Leemput, F. Maes, D. Vandermeulen, and P. Suetens, "Automated model-based tissue classification of MR images of the brain," *IEEE Transactions on Medical Imaging*, vol. 18, no. 10, pp. 897–908, 1999.

[32] W. Lorensen and H. Cline, "Marching cubes: A high resolution 3D surfaces construction algorithm," *ACM Computer Graphics*, vol. 21, no. 4, pp. 163–169, 1987.

[33] L. R. Herrmann, "Laplacian-isoparametric grid generation scheme," *Journal of the Engineering Mechanics Division*, vol. 102, no. 5, pp. 749–907, 1976.

[34] H. Si, "TetGen. A Delaunay-based quality tetrahedral mesh generator," *ACM Trans. Math. Software*, vol. 41, no. 2, p. 11, 2015.

[35] A. del Palomar, B. Calvo, J. Herrero, J. López, and M. Doblaré, "A finite element model to accurately predict real deformations of the breast," *Medical Engineering and Physics*, vol. 30, no. 9, pp. 1089–1097, 2008.

[36] K.-J. Bathe, *Finite element procedures, 2nd edition*. Klaus-Jurgen Bathe, 2014.

[37] Y. Fung, *Biomechanics: Mechanical Properties of Living Tissues, 2nd ed.* Springer, 1993.

[38] S. Johnsen, Z. A. Taylor, M. Clarkson, J. Hipwell, M. Modat, B. Eiben, L. Han, Y. Hu, T. Mertzanidou, D. J. Hawkes, and S. Ourselin, "NiftySim: A GPU-based nonlinear finite element package for simulation of soft tissue biomechanics," *J. Computer Assisted Radiology and Surgery*, 2014.

[39] K. Miller, G. Joldes, D. Lance, and A. Wittek, "Total lagrangian explicit dynamics finite element algorithm for computing soft tissue deformation," *Communications in numerical methods in engineering*, vol. 23, no. 2, pp. 121–134, 2007.

[40] S. Kirkpatrick, M. P. Vecchi *et al.*, "Optimization by simmulated annealing," *Science*, vol. 220, no. 4598, pp. 671–680, 1983.

[41] D. Mattes, D. R. Haynor, H. Vesselle, T. K. Lewellyn, and W. Eubank, "Nonrigid multimodality image registration," in *Medical Imaging 2001*. International Society for Optics and Photonics, 2001, pp. 1609–1620.

[42] P. Wellman, "Tactile imaging," Ph.D. dissertation, Harvard University's Division of Engineering and Applied Sciences, 1999.

[43] J. Stoer and R. Bulirsch, *Introduction to numerical analysis*. Springer Science & Business Media, 2013, vol. 12.

[44] R. Siddon, "Fast calculation of the exact radiological path for a three-dimensional CT array," *Medical Physics*, vol. 12, pp. 252–255, 1985.

[45] C. M. Hsu, M. L. Palmeri, W. P. Segars, A. I. Veress, and J. T. Dobbins, "An analysis of the mechanical parameters used for finite element compression of a high-resolution 3d breast phantom," *Medical Physics*, vol. 38, no. 10, pp. 5756–5770, 2011.

[46] A. Lagae and P. Dutré, "Compact, fast and robust grids for ray tracing," *Computer Graphics Forum*, vol. 27, no. 4, pp. 1235–1244, 2008.

[47] S. Kullback and R. A. Leibler, "On information and sufficiency," *The annals of mathematical statistics*, vol. 22, no. 1, pp. 79–86, 1951.

[48] D. J. MacKay, *Information theory, inference and learning algorithms*. Cambridge university press, 2003.

[49] Z. Wang, A. C. Bovik, H. R. Sheikh, and E. P. Simoncelli, "Image quality assessment: From error visibility to structural similarity," *IEEE Transactions on Image Processing*, vol. 13, no. 4, pp. 600–612, 2004.

[50] J. Lewis, "Fast normalized cross-correlation," in *Vision interface*, vol. 10, 1995, pp. 120–123.

[51] E. García, A. Oliver, Y. Diez, O. Diaz, R. Martí, and J. Martí, "Mapping 3D breast lesions for full-field digital mammograms using subject-specific finite element models." in *Proceedings SPIE Medical Imaging*, 2017, p. 1013504.

[52] E. García, O. Diaz, R. Martí, Y. Diez, A. Gubern-Mérida, M. Sentís, J. Martí, and A. Oliver, "Local breast density assessment using reacquired mammographic images," *European Journal of Radiology*, pp. 121–127, 2017.

[53] N. Perry, M. Broeders, C. de Wolf, S. Törnberg, R. Holland, and L. von Karsa, Eds., *European guidelines for quality assurance in breast cancer screening and diagnosis (4th ed.)*. European Commission, 2006.

[54] H.-M. Chan, A. C. Chung, S. C. Yu, A. Norbash, and W. Wells, "Multi-modal image registration by minimizing kullback-leibler distance between expected and observed joint class histograms," in *Proceedings IEEE CVPR 2003*, vol. 2, 2003, pp. II–570.

[55] G. P. Penney, J. Weese, J. A. Little, P. Desmedt, D. L. Hill *et al.*, "A comparison of similarity measures for use in 2D-3D medical image registration," *IEEE Transactions on Medical Imaging*, vol. 17, no. 4, pp. 586–595, 1998.

5

Mapping 3D breast lesions using subject-specific finite element models

This chapter introduces a fast method to localize the 3D position of the lesion within the MRI, using both CC and MLO mammographic projections. Suspicious lesions in the MRI volume can be projected into the 2D mammographic space, however, most registration algorithms do not provide the reverse information, avoiding to obtain the 3D geometrical information from the lesions localized in the mammograms. The overall process consist of indexing the tetrahedral elements of the biomechanical model using a uniform grid. For each marked lesion in the FFDM, the X-ray path from source to the marker is calculated. Barycentric coordinates are computed in the tetrahedrons traversed by the ray. The list of elements and coordinates allows to localize two curves within the MRI and the closest point between both curves is taken as the 3D position of the lesion.

Title: Mapping 3D breast lesions from full-field digital mammograms using subject-specific finite element models.
Authors: Eloy García, Arnau Oliver, Oliver Diaz, Yago Diez, Albert Gubern-Mérida, Robert Martí and Joan Martí.
Published in: SPIE Conference on Medical Imaging, Proc. SPIE 10135, pp 1013504O1-1013504O8. Orlando, Florida. February 2017.
DOI: 10.1117/12.2255957

Mapping 3D breast lesions from full-field digital mammograms using subject-specific finite element models.

E. García[a], A. Oliver[a], O. Diaz[a], Y. Diez[b], A. Gubern-Mérida[c], R. Martí[a], and J. Martí[a]

[a]Institute of Computer Vision and Robotics, University of Girona, Spain
[b]Tokuyama Laboratory GSIS, Tohoku University, Japan
[c]Radboud University Medical Center, Nijmegen, The Netherlands

ABSTRACT

Patient-specific finite element (FE) models of the breast have received increasing attention due to the potential capability of fusing images from different modalities. During the Magnetic Resonance Imaging (MRI) to X-ray mammography registration procedure, the FE model is compressed mimicking the mammographic acquisition. Subsequently, suspicious lesions in the MRI volume can be projected into the 2D mammographic space. However, most registration algorithms do not provide the reverse information, avoiding to obtain the 3D geometrical information from the lesions localized in the mammograms. In this work we introduce a fast method to localize the 3D position of the lesion within the MRI, using both cranio-caudal (CC) and medio-lateral oblique (MLO) mammographic projections, indexing the tetrahedral elements of the biomechanical model by means of an uniform grid. For each marked lesion in the Full-Field Digital Mammogram (FFDM), the X-ray path from source to the marker is calculated. Barycentric coordinates are computed in the tetrahedrons traversed by the ray. The list of elements and coordinates allows to localize two curves within the MRI and the closest point between both curves is taken as the 3D position of the lesion. The registration errors obtained in the mammographic space are 9.89 ± 3.72 mm in CC- and 8.04 ± 4.68 mm in MLO-projection and the error in the 3D MRI space is equal to 10.29 ± 3.99 mm. Regarding the uniform grid, it is computed spending between 0.1 and 0.7 seconds. The average time spent to compute the 3D location of a lesion is about 8 ms.

Keywords: Breast MRI, Full-Field digital Mammography, Multi-modal registration, Finite Element modelling

1. INTRODUCTION

Magnetic resonance imaging (MRI) and X-ray mammography are two image modalities used to diagnose breast diseases in women. X-ray mammograms are considered the gold-standard in early breast disease detection. However, the 2D-projection makes locating suspicious lesions within the uncompressed breast difficult. In contrast, MRI provides this information at the cost of having less image resolution. Therefore, both modalities provide complementary information and, hence, the combination of these modalities is crucial to increase both the early diagnosis and biopsy procedures. During past decades, the efforts have been focused on establishing spatial correlation between both modalities. Subject-specific 3D finite element (FE) modeling of the breast has received increasing attention. To correlate MRI and mammographic images, the overall process consists in mimicking the mammographic acquisition, compressing the FE model and simulating the X-ray beam. The model is allowed to translate and rotate, while the elastic parameters can be modified in order to reach an accurate correspondence.

Most of the registration methods are limited to providing the distance of projected lesions from MRI with respect to the lesion within the mammogram. But they do not provide 3D geometrical information of the suspicious lesion within the MRI when they are located in the mammograms. Some exceptions can be found in the literature that consist in complex or computationally expensive approaches. Qiu et al.[1,2] use a 3D FE model to register temporal mammograms. The process consists in compressing the mechanical model and aligning it with the correspondent mammographic view (cranio-caudal (CC) or medio-lateral oblique (MLO)). A back-projection ray-cast is applied and the elements traversed by the X-ray's path are labeled. The compressed model is restored to the reference state and the straight line becomes a 3D curve in the initial model. When both CC and MLO projections are available, the 3D lesion is localized finding the minimum distance between both 3D curves. Hopp et al.[3] describe a similar approach to localize lesions within MR images using a patient-specific

Medical Imaging 2017: Image-Guided Procedures, Robotic Interventions, and Modeling, edited by Robert J. Webster III, Baowei Fei, Proc. of SPIE Vol. 10135, 1013504 · © 2017 SPIE
CCC code: 1605-7422/17/$18 · doi: 10.1117/12.2255957

model. Mertzanidou et al.[4] use a complex transformation to correlate the uncompressed and the compressed model. This transformation is performed during the ray-casting step and consists in undoing the transformation considering the rigid (translation and rotation) and non-rigid transformation (interpolating displacements within the FE model) to which the model is subjected. Solves-Llorens et al.[5] use the tetrahedrons which compose the model to localize lesions before and after compression, as well as between the MRI and mammograms. This method avoids decompressing the model and carrying out complex transformations. However, it may result slow depending on the number of elements composing the FE model.

Data structures are used in computer graphics to accelerate ray-casting and visualization. These structures use surface meshes composed of triangular elements, although some of them can be adapted to any other kind of elements, such as tetrahedral elements. In this work we use one of these structures to accelerate the localization of the ray from the compressed model to the MRI volume. Specifically, we use an uniform grid, adapting the work introduced by Lagae et al.,[6] to index the elements of the biomechanical model. Hence, the position of the sampled points along the ray can be simultaneously localized in the compressed model and the MRI, by means of computing the barycentric coordinates within the elements traversed by the ray. When both CC- and MLO-curves have been localized in the MRI, the search space of the intersection is reduced using a set of rules, and we obtained an accurate and fast navigation between both image modalities.

The rest of this document is organized as follows: Section 2 introduces the methodology used. We present the registration approach, the uniform grid construction and, finally, the fast 2D-3D correspondence method. Section 3 presents the results regarding the registration and the grid construction. We conclude the paper with discussion and conclusions.

2. MATERIAL AND METHODS

The dataset was composed of 10 cases from 10 different patients. Each case contains 1 MRI volume and 1 mammographic study, using full-field digital mammograms (FFDM), composed of both CC and MLO projections. Patients aged between 37 and 63 (48.8 ± 9.59). Images were acquired at the Radboud University Medical Center (Nijmegen, The Netherlands) between July 2008, and May 2011. The MRI scanner used was a 1.5 Tesla Siemens scanner (Magnetom Vision, Magnetom Avanto and Magnetom Trio) with dedicated breast coil (CP Breast Array, Siemens, Erlangen). MRI volumes had a size of $[512 \times 256 \times 120]$ voxels and $[0.664 \times 0.664 \times 1.300]$ mm^3 per voxel. Regarding the mammographic device, the images were acquired by either a GE Senographe 2000D or GE Senographe DS, according to the standard clinical settings. Mammograms were composed of $[2294 \times 1914]$ pixels, with $[0.094 \times 0.094]$ mm^2 per pixel. Both MRI and mammographic studies were acquired in the same day. The lesions were labeled by an expert medical image researcher.

This work was performed on a workstation Intel Core i7-3770 3.40 GHz, RAM 32 Gb, 64 bits equipped with a GPU NVIDIA GeForce GTX 770 (2 Gb).

2.1 MRI-FFDM registration

To obtain the FE model, MRI volumes are segmented by means of a probabilistic atlas approach, using a methodology similar to the one proposed by Gubern-Mérida et al.[7] The internal tissues of the breast are segmented using an expectation-maximization algorithm, while the breast mask images are resampled to obtain isotropic voxels. Afterwards, two different meshes are constructed by means of the standard Marching Cubes algorithm,[8] corresponding to the breast surface and glandular tissue. We use the open-source package TetGen[9] to build tetrahedral meshes, with the number of elements determined using a maximum volume criterion which is related to the MRI voxel volume. The stress-strain relationship of the biomechanical model is approximated by a nearly incompressible, isotropic and hyperelastic neo-Hookean model for each tissue (glandular and adipose), using the corresponding Young's modulus measured by Wellman.[10]The breast-body interface is fitted to a linear surface and nodes belonging to this surface are allowed to slide in the parallel direction of the compression paddle displacement.[11]

Once the biomechanical model has been built, it is duplicated in order to get both the uncompressed and the compressed models. For obtaining the latter, the necessary information to reproduce the acquisition (breast thickness, projection angle, source-to-detector distance or maximum tube voltage) is extracted from the DICOM

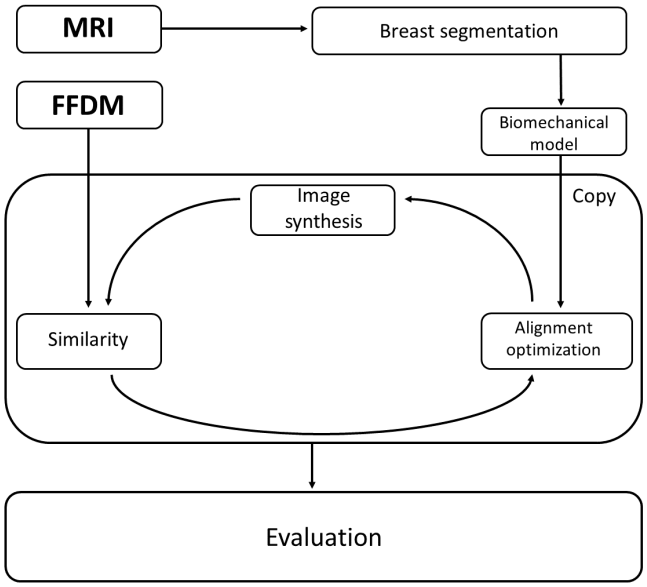

Figure 1. The registration approach. Beginning from the MRI, the breast is segmented and the biomomechanical model is built. This model is used to correlate the information of the MRI volume and FFDM mammograms. The final step is to evaluate the accuracy of this correlation.

header of the corresponding FFDM. The ray-casting is accelerated by a GPU implementation. The simulated annealing algorithm[12] is used to optimize the location and material parameters of the model.[4] The optimization process consists in finding the maximum Normalized Cross-Correlation between the actual and synthetic mammogram. Therefore, the parameters to optimize are:

- Position: translation of the model along a plane parallel to the mammogram.
- Orientation: the model is allowed to rotate around its principal axes.
- Elastic parameters: in this case, the Young's modulus of both adipose and glandular tissues.
- Compression: the breast thickness.

Eventually, uncompressed and compressed models of the breast are available. The former relates the physical space of the MRI volume while the compressed model is localized above the space defined by the mammogram. Figure 1 summarizes the registration process.

During this work, the FE analysis was performed using NiftySim^{TM} v.2.3.1[13] (University College London*). NiftySim^{TM} solves the Total Lagrangian Explicit Dynamic (TLED) FE formulation proposed by Miller et al.[14] for soft-tissue simulations.

2.2 Fast correspondence

Usually, to evaluate the accuracy of the algorithm, a target registration error (TRE) approach is performed using the lesions presented in both modalities. The 2D TRE is computed as the Euclidean distance between the centroid of the lesion localized in the MRI, projected in the mammography, and the centroid of the lesion in the mammogram. Figure 2 shows an example of both the real lesion in a mammogram and the projected one from the MRI volume.

Nevertheless, as we expose in section 1, the 3D TRE requires of complex approaches that, usually, include the decompression of the breast model. In our approach, we build a data structure to index the elements of the

*https://sourceforge.net/projects/niftysim/

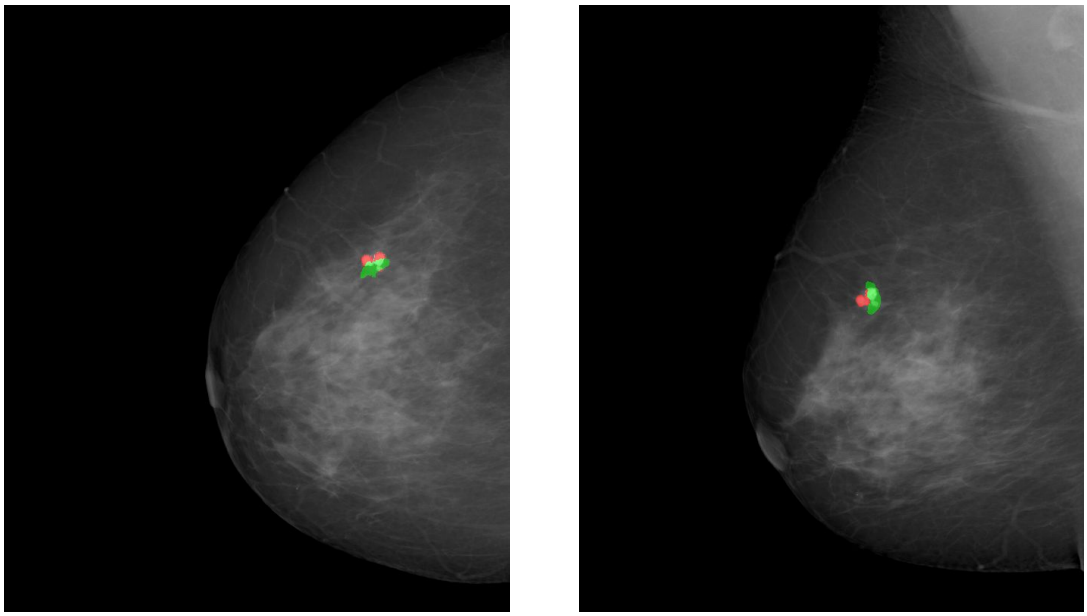

Figure 2. CC and MLO mammograms of the same patient. The red area corresponds to the suspicious regions in the mammograms, while the green area represents the location of the MRI lesion, once the registration has been performed.

model. The ray traversing the compressed model is localized automatically in the uncompressed model, at the same time. Using both, the ray traversing the CC- and that traversing the MLO- model, in the MRI volume, the intersection is computed by using a set of rules to reduce the search space among the points. The following sections explain the construction of the grid and the search space reduction.

2.2.1 Uniform grid construction algorithm

When the biomechanical breast model reaches the optimal position with respect to the mammogram, an uniform grid is used to store the element indexes of the compressed breast. The overall process to build this grid consists in:

- First, the bounding box of the compressed breast model is computed. The origin, size and spacing of the grid are established to initialize the grid around the model.
- The Axis-Aligned Bounding Boxes (AABB) of all elements in the compressed breast model are calculated.
- The uniform grid obtained is composed of three arrays:
  - The first array corresponds to the number of events, number of AABB, overlapping each voxel in the grid.
  - The second array computes the accumulative sum of all previous events of the first array.
  - The third array corresponds to the element list. This array is initialized with length equal to the total sum of events indexed in the first array. The corresponding element number is allocated using the sum of events before the voxel plus the corresponding position of the event in the voxel.

The time complexity of this algorithm is linear in the number of elements.

2.2.2 2D-3D correspondence

To provide the location of the breast lesion within the MRI volume from FFDM, the lesion has to be visible and specified in both CC and MLO projections. Once the lesion is localized in the mammograms, the projection from the X-ray source to the lesion is defined. The ray is described by the parametric equation of the straight line. Sampling the ray is carried out incrementing the parametric value.

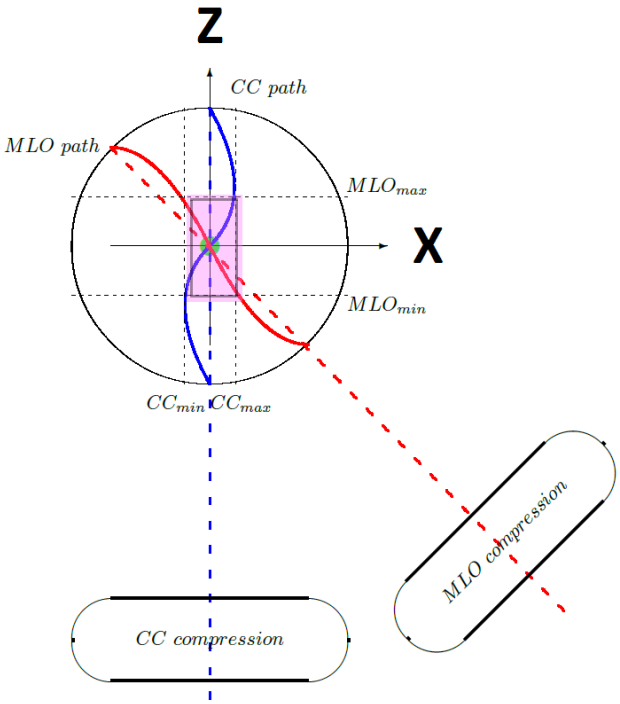

Figure 3. Both CC- and MLO- paths are represented by the blue and red curves, respectively, from their respective compressed models. The purple region represents the reduced search space where the 3D lesion (green dot) is localized.

To localize a given path within the MRI volume, for each sampled point along the ray's path, the corresponding voxel in the grid is computed from its physical position. For each element belonging to the voxel, the barycentric coordinates are computed. If the point is inside the element, the barycentric coordinates are used to localize the position in the uncompressed model. Thus, all points belonging to one ray in the compressed model are moved to the uncompressed model, obtaining a curve in the MR image.

Using both CC- and MLO- curves, we localize the suspicious lesion within the image using the minimum distance between both curves. However, we also speed-up the procedure by reducing the search space as follows:

- First, both curves are projected in the anterior-posterior (Y) direction.
- The minimum (CC_{min}) and maximum (CC_{max}) of the CC-ray in the medial-lateral (X) direction are computed in order to reduce the search space.
- Points belonging to the MLO-ray outside of the interval [CC_{min}, CC_{max}] are not considered.
- The maximum (MLO_{max}) and minimum (MLO_{min}) in the inferior-superior (Z) direction are computed, using the valid points of the MLO-ray. The points belonging to the CC-ray outside of the interval are excluded.

Thus, the search space is reduced between [CC_{min}, CC_{max}] in the X direction and [MLO_{min}, MLO_{max}] in the Z direction. The Euclidean distances between the points belonging to the CC-ray and the MLO-ray within both intervals are computed, and the center of mass of the two points with the smallest distance is considered the 3D center of the lesion. Figure 3 represents the anterior-posterior projection of the breast, traversed by the CC- (blue) and the MLO- (red) rays.

Table 1. Number of points and elements composing each model, as well as mean number of elements per voxel in the grid, $mean_{CC}$ and $mean_{MLO}$, and time of construction, t_{CC} and t_{MLO}, in seconds, for both CC- and MLO-projections.

	#points	#elements	$mean_{CC}$	t_{CC}	$mean_{MLO}$	t_{MLO}
Case 1.	10,458	61,559	13.91	0.354	11.12	0.252
Case 2.	8,811	49,895	11.92	0.156	10.43	0.087
Case 3.	14,701	78,098	11.83	0.215	13.22	0.340
Case 4.	13,467	79,796	14.36	0.256	10.52	0.190
Case 5.	17,979	98,574	12.67	0.303	10.52	0.373
Case 6.	43,556	260,444	17.24	0.613	16.11	0.647
Case 7.	9,056	52,242	12.86	0.108	11.55	0.066
Case 8.	10,977	57,555	14.96	0.213	12.82	0.271
Case 9.	5,908	32,245	14.18	0.068	11.46	0.078
Case 10.	7,525	41,880	13.24	0.420	12.00	0.169

Table 2. Number of points composing each ray and final number of points to be checked after the search space reduction. Furthermore, we include the minimum separation between both rays, in millimeters, and time of computing the intersection, in seconds.

	Ray_{CC}	Ray_{MLO}	Separation (mm)	Time (s)
Case 1.	13/ 798	19/ 753	8.16	0.008
Case 2.	37/ 609	68/ 786	2.93	0.014
Case 3.	15/ 738	21/ 810	9.06	0.011
Case 4.	16/ 741	28/ 936	0.75	0.005
Case 5.	45/ 942	84/1302	6.93	0.016
Case 6.	23/1023	40/ 957	0.35	0.005
Case 7.	13/ 477	29/ 444	0.91	0.004
Case 8.	57/ 678	82/ 714	1.85	0.006
Case 9.	2/ 468	6/ 606	0.56	0.004
Case 10.	17/ 768	29/ 708	2.70	0.005
mean	23.8/ 727.2	40.6/ 801.6	3.42 ± 3.35	0.008 ± 0.005

3. EXPERIMENTAL RESULTS

Biomechanical models are built from precontrast T1-weighted MRI. The number of elements composing the breast model depends on the MRI voxel volume and the total volume of the breast and, therefore, is different for each model. In our data set, the number of points composing each model range between 5,908 and 43,556, while the number of elements vary from 32,245 to 260,444. Once the registration is performed, the uniform grid is built around the compressed breast model to store the element indexes. The accuracy of the grid depends on internal factors, such as the grid resolution or the voxel size, and external factors, such as the number of elements composing the model as well as the amount of compression. Based on previous experiments, we use a 2-mm length voxel to define the grid. Origin and size are determined by the axis-oriented bounding box of the compressed model. Table 1 shows the statistical analysis of our dataset, points and elements composing each model, mean number of elements per voxel in the grid and the time of grid construction, in seconds.

We use the backprojection from the centroid of the lesion localized within the mammogram to simulate each ray traversing the corresponding compressed model, but we only consider those points that are inside of the model. Hence, the length of each ray depends on the thickness of the biomechanical model, once it was compressed. During this study, the maximum number of points along a ray was 1,302 points, while the minimum was 444. As is usual, checking the distance point-by-point, the number of combinations varies between 200,000 (case 7) and 1,250,000 (case 5) in our data set. Using our approach for search space reduction, the number of points to be checked is drastically reduced. The best result is obtained in the case 9, where the number of combinations in the final search space is 12 (6×2 points) from 283,608 (468×606 points) possible combinations at the beginning. The mean value for the search space reduction is 1,378 from 611,783 combinations in our dataset. Therefore, the search space is reduced 1/600 approximately. Table 2 shows more detailed information about the space reduction, considering each projection independently.

Table 3. Detailed information of the target registration error, in millimeters, in 2D and 3D.

	c1	c2	c3	c4	c5	c6	c7	c8	c9	c10	mean	std
CC	7.50	11.37	17.11	5.14	11.52	6.03	8.20	7.10	12.31	7.05	9.89	3.72
MLO	17.65	8.63	14.16	7.21	4.31	4.48	4.04	5.66	9.98	4.25	8.04	4.68
MRI	11.06	15.93	13.64	7.51	9.671	3.30	8.35	10.11	7.50	7.45	10.29	3.99

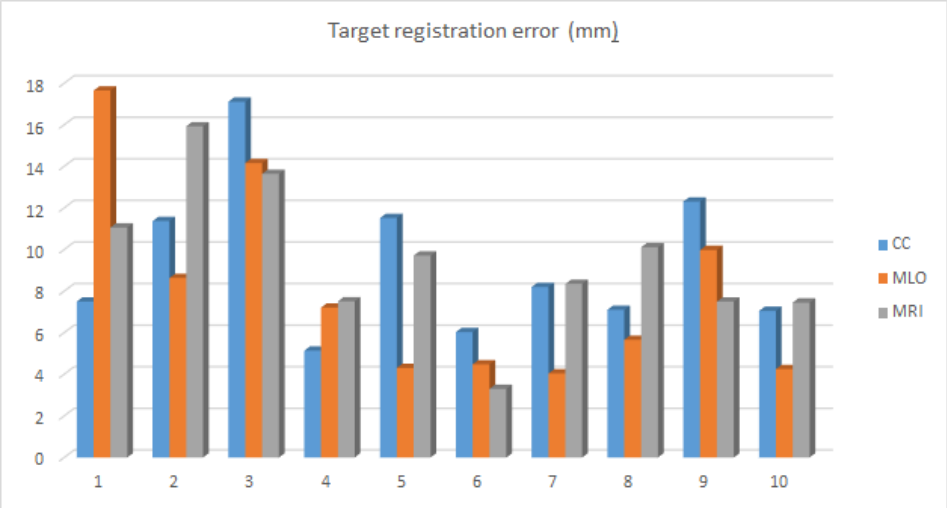

Figure 4. Target registration errors, in millimeters, obtained using our registration algorithm.

Finally, the MRI-mammography registration spends between 2 and 5 hours and the error evaluation is performed as exposed in section 2.2.2. The final TRE results are presented numerically in table 3 and graphically in figure 4. The best result in 2D is about 5 mm and 3 mm in 3D. Mean error values correspond to $9.89 \pm 3.72\ mm$ in CC-, $8.04 \pm 4.68\ mm$ in MLO-projection and $10.29 \pm 3.99\ mm$ in the MRI volume.

4. DISCUSSION AND CONCLUSIONS

In this work we introduced a fast approach to localize lesions between MRI and X-ray mammograms using a finite element model combined with a uniform grid to correlate both modalities. This method allows to localize small lesions like microcalcifications and masses in the 3D MRI when they are located in both CC and MLO mammographic views. Regarding the data structure, the uniform grid provides an accurate method to index the elements. Its main advantage compared to other data structures, such as octrees or kd-trees, is that it is easier to implement and faster to build than the others. Furthermore, due to the breast is compressed between parallel paddles, the grid is almost fulfilled and tracing the ray through the grid requests less computational requirements. The errors reported in our study are 9.89 mm in CC and 8.04 mm in MLO, in line with those reported by Mertzanidou et al.,[4] and 10.29 mm in the 3D volume, smaller than Hopp et al.[3] . The time spent to compute the 3D location of the lesion, once the mammograms and the MRI are registered, is about 8 ms, allowing its use in real time applications.

Once the registration is performed, several clinical applications can be developed. For instances, we can use the biomechanical model to obtain the registration between CC and MLO views (ipsilateral registration), which can be very useful for correlation the different breast structures. Moreover, this step can help int he computation of multimodal features for CAD algorithms of the fast tracking of the needle biopsy between modalities. Furthermore, assuming that there is not a significant change of the breast tissues between two time points, we could use he same biomechanical model to correlate temporal mammogram, helping the radiologist to evaluate the temporal evolution of susceptible areas.

5. ACKNOWLEDGEMENT

This research has been partially supported from the University of Girona (MPC UdG 2016/022 grant), the European Union within the Marie Sklodowska-Curie Innovative Training Networks (SCARtool project H2020-MSCA-IF-2014, reference 657875) and the Ministry of Economy, Industry and Competitiveness of Spain, under project SMARTER (DPI2015-68442-R) and the FPI grant BES-2013-065314.

REFERENCES

[1] Qiu, Y., Sun, X., Manohar, V., and Goldgof, D., "Towards registration of temporal mammograms by Finite Element simulation of MR Breast volumes," *Proc. SPIE Med. Imag.* **1**, 69182F–69182F, International Society for Optics and Photonics (2008).

[2] Qiu, Y., Goldgof, D., Li, L., Sarkar, S., Zhang, Y., and Anton, S., "Correspondence recovery in 2-view mammography," *IEEE Biomed. Imag.: Nano to Macro* **1**, 197–200, IEEE (2004).

[3] Hopp, T. and Ruitter, N., "2D/3D registration for localization of mammographycally depicted lesions in breast MRI," *IWDM 2012* **7361**, 627–634 (2012).

[4] Mertzanidou, T., Hipwell, J., Johnsen, S., Han, L., Eiben, B., Taylor, Z., Ourselin, S., Huisman, H., Mann, R., Bick, U., et al., "MRI to X-ray Mammography intensity-based registration with simultaneous optimisation of pose and biomechanical transformation parameters," *Med. Imag. Analysis* **18**(4), 674–683 (2014).

[5] Solves-Llorens, J. A., Rupérez, M., Monserrat, C., Feliu, E., García, M., and Lloret, M., "A complete software application for automatic registration of X-ray mammography and magnetic resonance images," *Med. Phys.* **41**(8), 081903 (2014).

[6] Lagae, A. and Dutré, P., "Compact, fast and robust grids for ray tracing," *Comp. Graphics* **27**(4), 1235–1244, Wiley Online Library (2008).

[7] Gubern-Mérida, A., Kallenberg, M., Platel, B., Mann, R., Martí, R., and Karssemeijer, N., "Volumetric breast density estimation from full-field digital mammograms: A validation study," *PLoS One* **9**(1), e85952 (2014).

[8] Lorensen, W. and Cline, H., "Marching Cubes: A high resolution 3D surfaces construction algorithm," *ACM Comp. Graphics* **21**(4), 163–169 (1987).

[9] Si, H., "TetGen. A Delaunay-based quality tetrahedral mesh generator," *ACM Trans. Math. Software* **41**(2), 1–36 (2015).

[10] Wellman, P., *Tactile imaging*, PhD thesis, Cambridge, MA: Harvard University's Division of Engineering and Applied Sciences (1999).

[11] Han, L., Hipwell, J., Tanner, C., Taylor, Z., Mertzanidou, T., Cardoso, J., Ourselin, S., and Hawkes, D., "Development of patient-specific biomechanical models for predicting large breast deformation," *Phys. Med. and Bio.* **57**(2), 455–472 (2012).

[12] Kirkpatrick, S., Gelatt, C. J., and Vecchi, M., "Optimization by simulated annealing," *Science* **220**(4598), 671–680 (1983).

[13] Johnsen, S., Taylor, Z. A., Clarkson, M., Hipwell, J., Modat, M., Eiben, B., Han, L., Hu, Y., Mertzanidou, T., Hawkes, D. J., and Ourselin, S., "NiftySim: A GPU-based nonlinear finite element package for simulation of soft tissue biomechanics," *J. Comp. Assisted Radiology and Surgery* **10**(7), 1077–95 (2014).

[14] Miller, K., Joldes, G., Lance, D., and Wittek, A., "Total lagrangian explicit dynamics finite element algorithm for computing soft tissue deformation," *Comm. Num. Meth. Eng.* **23**(2), 121–134 (2007).

6

Breast MRI and X-ray mammography registration using gradient values

This chapter introduces two gradient-based registration approaches for breast MRI and X-ray mammography, comparing the result with a traditional intensity-based algorithm. During the intensity-based optimization, the MRI volume is transformed to a pseudo-CT image using the tissue segmentation. Therefore, digitally reconstructed radiographies (DRR) can be obtained by a direct intensity projection. Furthermore, in the gradient-based approaches, the intensity gradients of the glandular tissue are projected from the 3D MRI volume to the 2D mammographic space.

Title: Breast MRI and X-ray mammography registration using gradient values.
Authors: Eloy García, Yago Diez, Oliver Diaz, Xavier Lladó, Albert Gubern-Mérida, Robert Martí, Joan Martí, and Arnau Oliver.
Submitted to: Medical Image Analysis - Under Review.

Eloy García, Yago Diez, Oliver Diaz, Xavier Lladó, Albert Gubern-Mérida, Robert Martí, Joan Martí, and Arnau Oliver. “Breast MRI and X-ray mammography registration using gradient values”. Manuscript submitted for publication.

Abstract

Breast magnetic resonance imaging (MRI) and X-ray mammography are two image modalities widely used for early detection and diagnosis of breast diseases in women. The combination of these modalities, traditionally done using intensity-based registration algorithms, leads to a more accurate diagnosis and treatment. In this work, we present the first attempt to use the intensity gradients to co-localize lesions and susceptible areas between the breast MRI and X-ray mammography images. A patient-specific biomechanical model of the breast, extracted from the MRI image, is used to mimic the mammographic acquisition. The intensity gradients of the glandular tissue are projected from the 3D MRI volume to the 2D mammographic space, and two di erent gradient-based metrics are tested to lead the registration, the normalized cross-correlation of the scalar gradient values and the gradient correlation of the vectorial gradients. We compare these two approaches with a traditional intensity-based algorithm, where the MRI volume is transformed to a pseudo-CT image using the partial volume effect obtained by the tissue segmentation. This allows to obtain the digitally reconstructed radiographies by a direct intensity projection. The best results are obtained using the scalar gradient approach along with a transversal isotropic material model, obtaining a target registration error (TRE), in millimeters, of 5:65 2:76 for CC- and of 7:83 3:04 for MLO-mammograms, while, in the 3D MRI, the TRE is 7:33 3:62. We also evaluate the effect of the glandularity of the breast as well as the landmark position on the TRE, obtaining moderated correlation values (0:65 and 0:77 respectively), concluding that these aspects need to be considered to increase the accuracy in further approaches.

Key words

Breast cancer, Multimodal registration, X-ray mammography, MRI

7 Results and discussion

The aim of this thesis was to correlate the information -i.e. tissues, lesion position and intensity gradients- contained in both breast MRI and X-ray mammography, in order to establishing an accurate correspondence between the two modalities. To achieve this purpose, several multimodal registration algorithms, based on patient-specific biomechanical models, were proposed as well as multiple similarity metrics in order to evaluate the accuracy of our methodology, due to the multimodal nature of the problem. This thesis was divided into two big parts. The first part was focused on evaluating the similarity between the information contained in both breast MRI and X-ray mammography, specifically the glandular tissue distribution obtained from the two image modalities. The second part introduces several algorithms to establishing spatial correspondence of lesions and susceptible areas.

This chapter resumes the results and discussion of our work. Thus, following section summarize the methodology and results obtained for each chapter in this thesis, analyzing the main contribution of each one.

7.1 Literature review

Breast cancer is the most common cancer in women worldwide. While several image modalities are used to carry out the breast disease detection, the combination of multiple image modalities leads to a more accurate diagnosis and treatment. Chapter 2 introduces a step-by-step review in registration between breast MRI and X-ray mammography, focusing our attention in those methodologies that involves patient-specific finite element models.

Specifically, this chapter provided a wide perspective from the biomechanical model construction, including the MRI segmentation, surface and volume mesh extraction as well as several methods to quantify the accuracy and quality of the FE model, to the physics underlying the mechanical deformation, and elastic and hyperelastic parameters reported in the literature. Furthermore, software options and some technical and clinical aspects are introduced with the aim to bridge the gap between the engineering and the clinical knowledge. This wide perspective makes the work suitable not only for expert researchers but also for graduate students and clinicians.

Chapter 2 begins with a brief exposition of some technical challenges that are inherent to the nature of the problem. The physics underlying each modality, MRI and mammography,

are different, providing complementary information about the internal tissues of the breast. Similarly, the image acquisition differs due to the patient positioning and the movement restriction applied during the acquisition in each modality. Considering these limitations, the use of a patient-specific finite element model has been proposed in this and other fields, in order to reproduce the image acquisition of one of the modalities. In this case, a biomechanical model is extracted from the MRI volume and it is used to mimic the mammographic acquisition, being compressed. Later, the internal tissues of the breast are projected, obtaining a synthetic mammogram. The final image is compared to the original mammogram in order to establish a suitable position of the 3D model with respect to the 2D image.

The motivation to simulate breast biomechanics corresponds to the need to obtain physically realistic deformation in both the surface and the internal surface of the breast. A reliable biomechanical model is essential to predict the deformation of the internal tissues and movement of suspicious lesions in the breast during image procedures. Furthermore, to describe a precise physical behaviour, a realistic biomechanical model of the breast requires accurate knowledge about internal an external factors. The extraction of the biomechanical model involves:

- The geometry extraction. The breast volume is delimited by means of segmenting the MRI image. Using the segmentation, the FE meshes are built.
- Material description. The elastic or hyperelastic parameters need to be addressed, in order to define a suitable material behaviour.
- Force definitions. Loading forces and boundary conditions define the deformation of the model during the FE analysis.

Regarding the segmentation step, during the geometry extraction, we exposed some algorithms previously used in this task, with special emphasis in those used in the multimodal MRI-mammography registration. These methods include automatic pectoral muscle [13] and whole breast segmentation algorithms [41] as well as glandular tissue segmentation by means of clustering- [39] and intensity-based algorithms [23] and those that preserve the spatial information [28]. Moreover, some methods to perform the quantitative evaluation, such as the Dice overlap coefficient and Jaccard similarity coefficient, are included in the exposition.

On the other hand, in the section regarding the mesh generation, we focused our attention in the extraction of, first, the surface and, later, the volume mesh. The surface extraction can be performed using high-order polynomials to parameterize the breast surface [23] or by means of isosurface extraction algorithms [27]. Furthermore, the most common procedures to encode the volume spatial information are exposed, summarizing type and number of elements as well as the tissue modeled for each case. In this case, the accuracy of the biomechanical model is performed by, for instance, the root mean square in the case of surface meshes and the aspect ratio of volumetric elements, in the case of volume meshes.

Later, we exposed a brief introduction of the physics underling the mechanical deformation with special emphasis to the non-linear formulation of the elasticity theory [25]. Furthermore, available empirical data of the elastic and hyperelastic parameters were exposed, considering the most accepted studies as well as those that have been tested in the FE mechanical simulation. The section concludes with the exposition of loading forces and boundary conditions to obtain an unloaded reference state, to perform the breast compression simulation and a brief overview of the commercial and open-source FE packages that have been tested in the registration between MRI and X-ray mammography.

Finally, the basis of the image registration (projection of the internal tissues, mammographic simulation and the model transformation) are exposed. The registration methods introduced in the paper are focused on external landmarks such as breast contour or dice overlap coefficient, and intensity-based methods.

7.2 Local breast density in reacquired mammograms

The aim of Chapter 3 was to evaluate the repeatability of the glandular tissue measures provided by the commercial software Volpara^{TM} using reacquired mammographic images. In particular, the dataset was composed of 99 pairs of repeatedly acquired FFDM (198 images) obtained from 99 different patients. Each image pair corresponded to mammograms acquired within a very short time interval (few minutes). The images were obtained from a real clinical scenario, where mammograms were repeated due to the presence of suspicious findings. The dataset was acquired between 2008 and 2016 at the Radboud University Medical Center (Nijmegen, The Netherlands) and UDIAT Centre Diagnostic (Barcelona, Spain) using a GE Senographe machine and a Hologic Selenia Dimension system respectively. To extract the glandular tissue, we used the FDA-approved software Volpara^{TM} (v.1.5.11).

Global and local measures were used to evaluate the glandular estimation obtained by Volpara^{TM}. On one hand, the global measures provided by the software, breast volume (BV), volume of glandular tissue (VGT) and volumetric breast density (VBD), were compared between the two acquisitions. These values showed a high correlation - breast volume $R = 0.99$, volume of glandular tissue $R = 0.94$ and volumetric breast density $R = 0.96$ - regardless the acquisition parameters and mammographic device.

On the other hand, local measures from the Volpara^{TM} Density maps was evaluated in order to compare the shared information, using histogram similarity metrics, such as the histogram intersection and histogram correlation. These metrics showed that, for each pair of density maps, the images shared a high degree of information. The histogram intersection was within the interval 0.6 and 1 for every cases, while the histogram correlation was between 0.4 and 1, showing a better performance using the Hologic Selenia Dimension system during the mammographic acquisition.

Furthermore, the structural similarity of the tissue distribution were evaluated. The reproduction of exact image acquisition conditions during repeated mammograms is not possible in practice, due to small variations in patient positioning, differences in breast compression or, even different image acquisition parameters that are selected by an automatic exposure control software. In order to minimize these misalignments, we performed a two-dimensional registration step. In particular, we tested B-spline deformations, morphons, SyN and the combination B-spline SyN.

To evaluate the structural similarity of the tissue distribution, we computed the statistics of the difference image (mean, entropy and standard deviation from the overlapping region) and the gradient correlation between the fixed and registered image. Gradient measures may be used to extract spatial information from density maps. Moreover, factors of influence in Volpara^{TM} Density Maps, such as the amount of breast compression, anode/filter materials, end point energy of the spectrum, and changes in the angle of view, were analyzed. While the behavior of Volpara^{TM} was stable in most of cases, changes in the breast thickness between two acquisitions affect the spatial parenchymal distribution. In particular, the larger the breast thickness difference, the larger the mean difference, which indicates a larger difference in the local glandular tissue distribution. A similar trend was observed in the gradient correlation, obtained smaller values when the breast thickness difference increase.

This study indicates that Volpara^{TM} Density maps is reliable in estimating glandular tissue distribution while the structural similarity of the parenchymal distribution is related to patient positioning and breast compression.

7.3 Multimodal parenchymal patterns correlation

Considering the results exposed in the previous chapter, Chapter 4 analyze the parenchymal patterns correlation from MRI and mammography. The aim of this work was to produce a realistic 2D breast parenchymal distribution from a 3D MRI, which is comparable to Volpara^{TM} density maps. We developed a fully-automatic framework to register the two image modalities. The mammographic compression is reproduced using a subject-specific biomechanical model extracted from the MRI volume. Then, the registration was performed optimizing the position, orientation and elastic parameters of the model until it reached an optimal solution. The mutual information metric was used to compare the synthesized density map and that provided by Volpara^{TM}.

Regarding previous work in MRI to X-ray mammography registration, in this chapter, we provided an anatomical landmark, as is the sternum point, to separate the breast from the body. Moreover, a fully automatic whole breast and glandular tissue segmentation algorithms were used. Nodes, on the biomechanical model, belonging to the breast-body interface were automatically selected, using morphological filters and logical operations. The number of tetrahedral elements was related to the voxel volume in the MRI image to minimize the numerical error during the FE simulation. Furthermore, we proposed a new approach to avoid resampling the MRI volume and to reduce the loss of information during the ray-casting.

After the registration, both the uncompressed and compressed models of the breast are available. The former relates the physical space of the MRI volume while the compressed model is localized above the space defined by the density map. To perform the ray-casting, a uniform grid is used to index the elements of the compressed FE model. Hence, computing the barycentric coordinates within the elements traversed by the ray, the position of the sampled points along the ray can be simultaneously localized in the compressed and the uncompressed model -i.e. the MRI-. The glandular tissue is integrated using a Newton-Cotes approach and a line clipping algorithm is used in order to reduce the computational cost.

Similar to the previous chapter, the information extracted from the two image modalities and the structural similarities were evaluated. Considering the multimodal nature of the problem and the difference in the image resolution, we needed to propose a suitable methodology of evaluation. In this case, the shared information was compared using the Kullback-Leibler divergence (KLD) while the structural analysis was performed using the Structural Similarity (SSIM) index and the Normalized Cross-Correlation (NCC).

The first dataset used for the evaluation of the framework consisted of 50 pre-contrast T1 MRI volumes and 178 density maps from 42 women, acquired at the Radboud University Medical center between April 2005 and March 2011. Both MRI and mammographic studies were acquired the same day. To provide a fair comparison we used a second dataset composed by 21 pairs of reacquired mammograms, similar to the chapter 3. Furthermore, the multimodal dataset was divided considering the BI-RADS rating and the corresponding CC- or MLO-projection.

The results show that the information -i.e. thickness of glandular tissue- obtained from

the two image modalities, and compared using the KLD, presents a high agreement between them. The best value corresponds to denser breast, BI-RADS 4, with a value of 0.14 ± 0.10 while images belonging to patients with fatty breast, BI-RADS 1, show poor results (0.44 ± 0.29). Furthermore, the SSIM provide a statistical comparison between the structures situated in the same area in both images. The obtained results show also a high agreement between the two images, within the interval 0.76 and 0.88. Finally, the analysis of NCC values shows divergences considering the breast glandularity, obtaining better results in the densest breasts than in the fatty ones. The main divergence with respect to the previous structural analysis corresponds to the NCC which relates piwel-wise spatial consideration instead of the area-based analysis provided by the SSIM.

To conclude the evaluation, we performed a visual analysis using a checkerboard pattering image. This approach allows the evaluation at the border of each square of the density correspondence, the continuity of the glandular structures, as well as the smoothness in the tissue of both density maps. The visual assessment shows a different behaviour depending on the density grade. Densest areas show continuity with respect to the structures in the corresponding density maps but also it shows smooth tissue structures. Those images belonging to BI-RADS 2 and 3 yield a better performance, showing a higher visual similarity than those corresponding to BI-RADS 1 and 4.

7.4 Mapping 3D breast lesions

In the previous Chapter 4, we proposed a new methodology to carry out a ray tracing, transposing the ray from the compressed to the uncompressed biomechanical model, without deforming the original MRI. In order to co-localize the 3D position of the breast lesions from 2D mammograms, previous approaches proposed undoing the model deformation to obtain the ray path within the original breast MRI. Modifying our ray tracing algorithm we obtained a fast and efficient approach which avoids undoing the FE breast compression.

Thus, Chapter 5 introduced a new algorithm to compute the 3D location, within MRI images, of a lesion or a susceptible area from the corresponding FFDMs. Using a patient-specific biomechanical model, the two image modalities, MRI and mammography were registered. In this case, the approach requires the registration of the MRI with both CC- and MLO-projections. As is exposed in Chapter 4, the barycentric coordinates of the tetrahedral elements can be used to compute the ray path from the compressed to the uncompressed biomechanical model. Thus, when the two lesions are marked in the mammograms, the X-ray path from source to the marker is calculated. The list of elements and coordinates allows to localize two curves within the MRI and the closest point between both curves is taken as the 3D position of the lesion.

The main contribution of this chapter corresponds to propose an efficient algorithm to reduce the search space on the minimum distance between both CC- and MLO-curves, reducing the computational cost. Our approach consist in:

- First, both curves are projected in the anterior-posterior direction.
- The minimum (CC_{min}) and maximum (CC_{max}) of the CC-ray in the medial-lateral direction are computed in order to reduce the search space.
- Points belonging to the MLO-ray outside of the interval $[CC_{min},\ CC_{max}]$ are not considered.

- The maximum (MLO_{max}) and minimum (MLO_{min}) in the inferior-superior (Z) direction are computed, using the valid points of the MLO-ray. The points belonging to the CC-ray outside of the interval are excluded.

Thus, the search space is reduced between $[CC_{min},\ CC_{max}]$ in the X direction and $[MLO_{min},\ MLO_{max}]$ in the Z direction. The Euclidean distances between the points belonging to the CC-ray and the MLO-ray within both intervals are computed, and the center of mass of the two closest points with the smallest distance is considered the 3D center of the lesion.

We tested our algorithm using a dataset composed of 10 cases. Each case was composed of 1 MRI volume and 1 mammographic study (1 CC- and 1 MLO-projection). Notice that only one breast per patient contains a landmark -i.e. lesion or metallic clip-. Eventually, we computed the time of construction of the uniform grid (around $t = 0.4\ s$), number of element per voxel in the grid (in average, 14 element per voxel), initial number of points composing each ray (around 750) and final number of points to be checked after the search space reduction (30 points, in average), as well as the minimum separation between both rays (3.42 mm, in average) and time of computing the intersection ($t = 0.008\ s$) using the CPU. Finally, the target registration error was computed in 2D and 3D. The errors reported in our study were $9.89 \pm 3.72\ mm$ in CC and $8.04 \pm 4.68\ mm$ in MLO, in line with those reported by Mertzanidou et al. [27], and 10.29 mm in the 3D volume, smaller than Hopp et al. [18].

Our methodology allows to localize small lesion like microcalcifications and masses in the 3D MRI when they are located in both CC and MLO mammographic views. Furthermore, the search space, to compute the two closest points between the rays, is reduced 1/600, approximately, when it is compared to a traditional point-by-point approach. The time spent to compute the 3D location of the lesion, once the mammograms and the MRI are registered, is about 8 ms, allowing its use in real time applications, suitable in the clinical practice.

7.5 Gradient-based MRI to mammography registration

In Chapter 2, the categorization, defined by Markelj et al. [26], is exposed as a reference. In that paper, 3D/2D registration algorithms are divided into feature-, intensity- and gradient-based methods, according to the nature of the registration. In previous works about registration between breast MRI and X-ray mammography, feature- and intensity-based registration approaches were proposed. Nevertheless, as we exposed in the chapter, the use of gradient-based methods need to be analyzed. The aim of Chapter 6 was to introduce two gradient-based registration algorithms, inspired by the work of Mertzanidou et al. [27] and Wein et al. [43] and compare them with a traditional intensity-based approach.

Similar to the previous approaches, a biomechanical model was extracted from the MRI. In this case, only one singe material model was considered, comparing the results obtained by an isotropic and an anisotropic material models. The mechanical model extraction and the transformation was similar to that proposed previously. The main contribution corresponded to use the intensity gradient information in order to perform the registration. Furthermore, we compared the results of our proposed approach with a traditional intensity-based registration algorithm.

Regarding the intensity-based algorithm, in Chapter 4 we prove that the information obtained from the mammography and the MRI, using a probabilistic segmentation, is clearly

comparable. Therefore, in this case, we began transforming the MRI volume to a pseudo-CT image using the partial voxel effect obtained by means of an Expectation Maximization algorithm and using the weighted average of the Hounsfield scale. In order to perform a fully case-specific approach, the energy spectrum was computed considering the corresponding anode material.

Two gradient-based registration algorithms were proposed. First, the gradient modulus are accumulated along each ray, during the ray-casting and compared to the norm of the intensity gradients belonging to the corresponding mammogram using NCC. Second, The gradients are accumulated along each ray, considering each direction independently and the resulting vector and the intensity gradients obtained from the mammograms are compared using a gradient correlation metric.

A set of 10 cases, using a target registration error approach, was used to evaluate the accuracy of the proposed methods. First, isotropic vs. anisotropic material models were evaluated. A priori, the anisotropic models shows a better performance, reducing the TRE obtained using the isotropic biomechanical models. The gradient-based approach, using scalar gradient values, and the traditional intensity-based approach reduced their errors from 7.03 mm and 9.02 mm to 5.65 mm and 7.90 mm respectively for CC-projections, while for MLO-projections the errors were reduced from 9.67 mm and 12.96 mm to 7.83 mm and 9.96 mm respectively. This improvement was not found using vectorial gradient values. Similarly, these results showed that the gradient based approach obtained a better performance than the traditional intensity-based algorithm.

Eventually, we focused our attention in the correlation between the TRE and some factors as the breast glandularity or the landmark position. In the first case, there was not a clear correlation between the TRE and the breast density. In the second case, we found a medium correlation with respect to the distance between the landmark and the pectoral muscle. Furthermore, we proposed a methodology to localize the landmark within the breast using cylindrical coordinates. The axis of the system of reference are the pectoral muscle, approximated by a straight line, and a line in the perpendicular direction to this axis, which traverse the nipple. Thus, we can evaluate the landmark position with respect to the deviation of the principal direction (the axis perpendicular to the pectoral muscle, traversing the nipple). In this case, using the absolute value of angle, we obtained a medium correlation for CC and MLO projections.

The main limitation of this work is the number of cases which avoid us to extract a more accurate conclusion about the correlation values. Notice that this values may be different using a larger dataset. On the other hand, one of the contributions of this work is that we have reduced the spending time by the registration. The fastest registration was performed in 30 minutes and the average is about 1 hour, half the minimum time exposed in chapter 4. We consider that improving the initial position of the biomechanical model and modifying the optimization algorithm, even accelerating the process using the GPU, these approaches may be suitable in the clinical practice.

8

Conclusion and future work

To conclude this thesis, we back to the initial chapter to expose again the objectives and summarize the main contributions of this work. Afterwards, future work is given.

8.1 Conclusions

- To review the literature. Chapter 2 exposed a deep revision of the literature, focused on the registration methods based on patient-specific finite element models. A comprehensive analysis of the steps, geometry extraction, including image segmentation and mesh construction, physical modelling and multimodal registration as well as methods to quantify the accuracy and quality of the reported approaches, was performed in the paper. At the same time, we analyzed and review the state-of-the-art software and characteristics that make it suitable to face each step. With respect to other reviews, such as those presented by Babarenda et al. [9] and Hipwell et al. [15], our survey was more focused on these specific tasks, skipping other problems, such as prone-to-supine registration or multimodal 3D-3D registration. We believe that issues such as an accurate synthetic mammogram generation and the resolution of the biomechanical model, as well as obtaining a suitable geometry extraction, were overlooked in those other works. Moreover, none of the other works introduced the available software options, requirements or advantages of each tool, to yield a highly accurate solution of these problems. Finally, we also included the technical aspects needed to validate these registration methods using a clinical dataset as well as several medical applications, helping to bridge the gap between engineering and clinical performance.

  This review was published in *Medical Physics* in January, 2018.

- To analyze the reliability of automatic density measures using FFDM. Chapter 3 aimed to evaluate the spatial glandular tissue distribution as well as the automatic density measures provided by the commercial software Volpara^{TM} Density Maps using a dataset composed of repeatedly acquired full-field digital mammograms, where each pair was acquired in a short time frame. This chapter showed the reliability of both global and local density measures provided by Volpara^{TM}. While global measures are stable independently regardless the mammographic machine, parameters, such as the breast thickness, modify the spatial distribution of the glandular tissue. Nevertheless, deformable registration algorithms helps to mitigate this effect. This experiment provide a baseline result to evaluate the next question.

This analysis was published in *European Journal of Radiology* in May, 2017.

- To analyze the correlation of the glandular tissue between MRI and mammography. Chapter 4 analyzed the breast parenchymal distributions (i.e. density maps) obtained from FFDM and MRI. We developed a fully automatic framework which registers MRI volumes to X-ray mammograms using a subject-specific finite element model of the breast. Furthermore, we proposed a new approach to avoid resampling the MRI volume and a methodology to evaluate the problem, considering the particular multimodal nature of the images. In particular, we focused our efforts on evaluating the agreement of the distributions of glandular tissue, using the Kullback-Leibler divergence, the degree of structural similarity, using the Structural Similarity index, and the correlation between the real and synthetic density maps, by means of the Normalized Cross-Correlation. Our analysis showed a high agreement between the information obtained from the two image modalities as well as a high area-based structural similarity. However, one should be cautious when pixel-wise metrics are considered. Visual assessments showed smooth structures in the projection of the glandular tissue distribution obtained from MRI but the largest structures show continuity with those presented in the density maps.

  This work was accepted for publication in *IEEE Transactions on Medical Imaging* in August, 2017.

- To propose new methods to co-locate susceptible areas o lesions. This object is divided into the Chapters 5 and 6. Chapter 5 introduced a fast method to localize the 3D position of the lesion within the MRI, using both CC and MLO mammographic projections. The overall process consist of indexing the tetrahedral elements of the compressed biomechanical model using an uniform grid. For each marked lesion in the FFDM, the X-ray path from source to the marker is calculated. Barycentric coordinates are computed in the tetrahedrons traversed by the ray and the list of elements and coordinates allows to localize two curves within the MRI. The center of mass between the two closest point from each curve is taken as the 3D position of the lesion. The main contribution of this work is to introduce a fast and efficient algorithm to reduce the search space of the closest points, reducing the computational time and allowing real time applications in the clinical practice.

  This work was accepted in *SPIE Medical Imaging 2017: Image-Guided Procedures, Robotic interventions and Modelling.*

  Furthermore, Chapter 6 introduced two gradient-based registration approaches for breast MRI and X-ray mammography, comparing the result with a traditional intensity-based algorithm. During the intensity-based optimization, the MRI volume is transformed to a pseudo-CT image using the breast tissue segmentations. Thus, digitally reconstructed radiographies (DRR) can be obtained by a direct intensity projection. Furthermore, in the gradient-based approaches, the intensity gradients of the glandular tissue are projected from the 3D MRI volume to the 2D mammographic space. On the one hand, the scalar gradient values were considered to perform the registration, using the normalize cross-correlation metric, while, on the other hand, each direction was independently considered, performing the registration using a gradient correlation metric. The proposed gradient-based algorithm, using the scalar gradient values, improved the results obtained by the traditional intensity-based methodology.

  This work was submitted to *Medical Image Analysis* in November, 2017.

8.2 Future work

During this work, several limitations were found due to the software or hardware capabilities. These are not hard limits and their performance can be improved. In this work, we exposed some of these limitations and, based on them, we propose some future work lines.

8.2.1 MRI multi-acquisition segmentation

As we exposed in this thesis, the information contained in the T1-weighted MRI images and X-ray mammography is not the same due to the physics underlying and the image resolution. Small structures, such as vessels and ligaments, cannot be presented in the MRI volume. For instance, the problem of the shared information is shown in Chapter 4. Images belonging to BI-RADS 1 and 2 obtains a poor performance with respect to those obtained from BI-RADS 3 and 4 images, in all the statistics. Combining the segmentation obtained from multiple acquisitions, such as T1, T2 and T2* protocols as well as pre- and post-contrast images, may increase the similarity between the real and synthetic images.

8.2.2 Improving the biomechanical model

The aim of this thesis was to correlate the information between two image modalities, using a finite element biomechanical model. Although the biomechanical model is just a tool to perform the connexion between the two modalities, improving the characteristic of the model, as well as the FE analysis, may improve the registration. Similarly to the previous proposed task, the simulation of vessels, ligaments and any other structure presented in the breast could modify the model behavior and, therefore, the TRE obtained during the registration, specifically when the 3D position of the lesion is computed. Internal tissues of the breast deform differently depending on the material model and the internal structures that could be used during the FE simulation. Similarly, in Chapter 2, we introduced the available experimental data [22,37,44] but we focused our attention in the Wellmans measures because they are one of the most accepted analysis. However, the use of different material models and other elastic or hyperelastic parameters changes the behavior of the model and may vary the final result. Thus, comparing the models proposed in the literature and analyzing the elastic parameters obtained during the optimization may improve the mechanical behavior of the breast model.

8.2.3 Speed-up the framework

During this work, we have studied and proposed efficient algorithms to correlate the information between MRI and mammography. Using the GPU capabilities, the registration can be performed in a short time frame (less than one hour). However, the internal organ segmentation is based on a probabilistic atlas approach which requires to perform an image registration between the image in study and labeled images.

New segmentation and meshing algorithms can be tested in order to accelerate the biomechanical modelling process, avoiding the loss of accuracy. Furthermore, the initial position and the optimization algorithm may reduce the computational time and, even, improve the registration. For instance, we have tested that initializing the model 3 *cm* behind the centroid of the mammogram reduces the spending time. However, we can go one step beyond

using anatomical landmarks in the two modalities, such as the pectoral muscle or the nipple. Thus, the initial position of the model should be better and, therefore, the time may be reduced. Furthermore, other optimization algorithms such as differential evolution, particle swarm optimization or Markov chain Monte Carlo methods, may improve and accelerate the framework.

Eventually, using an efficient implementation, in a fully dedicated machine, may also reduce the computational time. Part of the spending time during the registration is waisted in the interface between the FE solver and our framework. Improving the communication between these two softwares could yield a computational time suitable in the clinical practice.

8.2.4 Using high-order registration metrics

In Chapter 6 we proposed using intensity gradient information to lead the registration. This approach opens the door to introduce new registration metrics or combining multiple metrics in order to improve the accuracy of the registration algorithms. For instance, Pluim et al. [35] combined mutual information and gradient information to perform the multimodal (MRI, CT and PET) registration of 3D images. These two metrics may be easily combined in our 3D-2D framework to lead the image registration. Similarly, several similarity measures have been proposed and could be adapted to our purpose.

8.2.5 Clinical application

As we exposed in the previous section, we consider that the algorithm can be accelerated in order to reduce the spending time to an assumable time in the clinical performance. In addition with the algorithm proposed in Chapter 5, the registration algorithm could be tested in the clinical practice. Several clinical applications, such as lesion follow-up, mammographic guided biopsy and ipsilateral registration as well as helping to radiologist to improve the diagnosis, need to be evaluated. Notice that in Chapter 2, we exposed that "*several works demonstrate that a multimodal combination leads to a more accurate diagnosis and treatment of the breast diseases from a medical point of view. However, the lack of commercial tools to correlate the different image modalities, such as MRI and mammography, avoids analyzing the clinical benefits of combining these modalities and how it affects the clinical decision*". Once the framework reach a suitable computational time, it should be tested in the clinical practice, not only as a tool in the clinical performance but also the benefits, regarding the diagnosis, follow-up and treatment of breast lesions, of fusing the information contained in MRI and mammograms.

Bibliography

[1] F. Azar, D. Metaxas, and M. Schnall. A finite element model of the breast for prediction mechanical deformations during biopsy procedures. *Mathematical Methods in Biomedical Image Analysis, Proceedings. IEEE Workshop*, pages 38–45, 2000.

[2] U. Bick and F. Diekmann, editors. *Digital Mammography.*, chapter Basic Physics of Digital Mammography., pages 1–11. Springer, 2010.

[3] BreastCancer.org, 2016. http://www.breastcancer.org/symptoms/testing/types.

[4] R. Damadian. Tumor detection by nuclear magnetic resonance. *Science (New York, NY)*, 171(3976):1151–1153, 1971.

[5] S. I. de Sénologie. Senologic International Society. History. about sis., 2014.

[6] M. Ferrant, S. Wardfield, A. Nabavi, F. Jolesz, and R. Kikinis. Registration of 3D intraoperative MR images of the brain using a finite element biomechanical model. *Proceding in Medical Image Computing and Computer-Assited Interverntion, Berlin, in Lecture Notes in Computer Science*, 1935:19–28, 2000.

[7] I. A. for Research on Cancer. Globocan 2012. http://globocan.iarc.fr/Default.aspx, 2016.

[8] B. Fuerst, T. Mansi, F. Carnis, M. Salzle, J. Zhang, J. Declerck, T. Boettger, J. Bayouth, N. Navab, and A. Kamen. Patient-specific biomechanical model for the prediction of lung motion from 4-D CT images. *IEEE Transactions on Medical Imaging*, 34(2):599–607, 2015.

[9] T. B. Gamage, V. Rajagopal, P. Nielsen, and M. Nash. Patient-specific modeling of breast biomechanics with applications to breast cancer detection and treatment. In *Patient-Specific Modeling in Tomorrow's Medicine*, pages 379–412. Springer-Verlag Berlin Heidelberg, 2011.

[10] A. Gefen, editor. *Patient-Specific Modeling in Tomorrow's Medicine*. Springer Berlin Heidelberg, 2011.

[11] J. Georgii, M. Eder, K. Bürger, S. Klotz, F. Ferstl, L. Kovacs, and R. Westermann. A computational tool for preoperative breast augmentation planning in aesthetic plastic surgery. *IEEE Journal of Biomedical and Health Informatics*, 14(3):907–919, 2014.

[12] R. H. Gold, L. W. Bassett, and B. E. Widoff. Highlights from the history of mammography. *Radiographics*, 10(6):1111–1131, 1990.

[13] A. Gubern-Mérida, M. Kallenberg, R. M. Mann, R. Marti, and N. Karssemeijer. Breast segmentation and density estimation in breast MRI: A fully automatic framework. *IEEE Journal of biomedical and health informatics*, 19(1):349–357, 2015.

[14] R. Hendrick, editor. *Breast MRI. Fundamentals and Technical Aspects.* Springer, 2008.

[15] J. H. Hipwell, V. Vavourakis, L. Han, T. Mertzanidou, B. Eiben, and D. J. Hawkes. A review of biomechanically informed breast image registration. *Physics in Medicine and Biology*, 61(2):R1, 2016.

[16] P. Hogg, J. Kelly, and C. Mercer, editors. *Digital Mammography: A Holistic Approach.* Springer, 2015.

[17] T. Hopp, B. Neupane, and N. Ruiter. Automated multimodal computer aided detection based on a 3D-2D image registration. In *International Workshop on Digital Mammography - IWDM'16*, pages 383–309. Springer, 2016.

[18] T. Hopp and N. Ruitter. 2D/3D registration for localization of mammographycally depicted lesions in breast MRI. *Lecture Notes in Computer Science*, 7361:627–634, 2012.

[19] T. Hu and J. Desai. A biomechanical model of the liver for reality-based haptic feedback. *In Medical Image Computing and Computer-Assisted Intervention-MICCAI*, pages 75–82, 2003.

[20] R. Jong. Breast cancer: The art and science of early detection with mammography. *American Journal of Roentgenology*, 187(1):W142–W142, 2006.

[21] J. M. Kalaf. Mammography: a history of success and scientific enthusiasm. *Radiologia Brasileira*, 47(4):VII–VIII, 2014.

[22] T. Krouskop, T. Wheeler, F. Kallel, B. Garra, and T. Hall. The elastic moduli of breast and prostate tissues under compression. *Ultrasound Imaging*, 20:151–159, 1998.

[23] A. Lee, V. Rajagopal, T. B. Gamage, A. Doyle, P. Nielsen, and M. Nash. Breast lesion co-localisation between X-Ray and MR Images using finite element modelling. *Medical Image Analysis, 17*, pages 1256–1264, 2013.

[24] S. Malur, S. Wurdinger, A. Moritz, W. Michels, and A. Schneider. Comparison of written reports of mammography, sonography and magnetic resonance mammography for preoperative evaluation of breast lesions, with special emphasis on magnetic resonance mammography. *Breast Cancer Research*, 3(1):55–60, 2001.

[25] L. Malvern. *Introduction to the Mechanics of a Continous Medium*, pages 282–290. Prentice-Hall, New Jersey, 1969.

[26] P. Markelj, D. Tomaževič, B. Likar, and F. Pernuš. A review of 3d/2d registration methods for image-guided interventions. *Medical Image Analysis*, 16(3):642–661, 2012.

[27] T. Mertzanidou, J. Hipwell, S. Johnsen, L. Han, B. Einben, Z. Taylor, S. Ourselin, H. Huisman, R. Mann, U. Bick, N. Kaissermeijer, and D. J. Hawkes. MRI to X-ray mammography intensity-based registration with simultaneous optimisation of pose and biomechanical transformation parameters. *Medical Image Analysis*, 18(4):674–683, 2014.

[28] T. Mertzanidou, J. Hipwell, C. Tanner, and D. Hawkes. An intensity-based approach to X-ray mammoraphy: MRI registration. In *SPIE Medical Imaging*, pages 76232Z–76232Z, 2010.

[29] A. B. Miller, C. Wall, C. J. Baines, P. Sun, T. To, and S. A. Narod. Twenty five year follow-up for breast cancer incidence and mortality of the canadian national breast screening study: randomised screening trial. *British Medical Journal*, 348, 2014.

[30] K. Miller and P. Nielsen. *Computational Biomechanics for Medicine*. Springer Science and Business Media, 2010.

[31] A. Mohamed, C. Davatzikos, and R. Taylor. A combined statistical and biomechanical model for estimation of intra-operative prostate deformation. *In Medical Image Computing and Computer-Assisted Intervention MICCAI*, pages 452–460, 2002.

[32] S. M. Moss, H. Cuckle, A. Evans, L. Johns, M. Waller, L. Bobrow, et al. Effect of mammographic screening from age 40 years on breast cancer mortality at 10 years' follow-up: a randomised controlled trial. *The Lancet*, 368(9552):2053–2060, 2006.

[33] Y. Payan. *Soft Tissue Biomechanical Modeling for Computer Assisted Surgery*. Springer Science and Business Media, 2012.

[34] N. Perry, M. Broeders, C. de Wolf, S. Törnberg, R. Holland, and L. von Karsa, editors. *European guidelines for quality assurance in breast cancer screening and diagnosis (4th ed.)*. European Commission, Office for Official Publications of the European Union, 2006.

[35] J. P. Pluim, J. A. Maintz, and M. A. Viergever. Image registration by maximization of combined mutual information and gradient information. In *International Conference on Medical Image Computing and Computer-Assisted Intervention*, pages 452–461. Springer, 2000.

[36] Y. Qiu, X. Sun, V. Manohar, and D. Goldgof. Towards registration of temporal mammograms by finite element simulation of MR breast volumes. In *Medical Imaging*, pages 69182F–69182F. International Society for Optics and Photonics, 2008.

[37] A. Samani, J. Bishop, M. Yaffe, and D. Plewes. Biomechanical 3-D finite element modelling of the human breast using MRI data. *IEEE Transactions on Medical Imaging*, 20:271–279, 2001.

[38] M. Sermesant, C. Forest, X. Pennec, and H. D. N. Ayache. Deformable biomechanical models: Application to 4D cardiac image analysis. *Medical Image Analysis*, 7(4):475–488, 2003.

[39] J. A. Solves-Llorens, M. Rupérez, C. Monserrat, E. Feliu, M. García, and M. Lloret. Segmentation of the breast skin and its influence in the simulation of the breast compression during an X-ray mammography. *The Scientific World Journal*, 2012.

[40] L. Tabar, M.-F. Yen, B. Vitak, H.-H. T. Chen, R. A. Smith, and S. W. Duffy. Mammography service screening and mortality in breast cancer patients: 20-year follow-up before and after introduction of screening. *The Lancet*, 361(9367):1405–1410, 2003.

[41] L. Wang, B. Platel, T. Ivanovskaya, M. Harz, and H. K. Hahn. Fully automatic breast segmentation in 3d breast mri. In *Biomedical Imaging (ISBI), 2012 9th IEEE International Symposium on*, pages 1024–1027. IEEE, 2012.

[42] S. Warren. A roentgenologic study of the breast. *The American Journal of Roentgenology and Radium Therapy*, 24:113–124, 1930.

[43] W. Wein, B. Röper, and N. Navab. 2D/3D registration based on volume gradients. In *Medical Imaging*, pages 144–150. International Society for Optics and Photonics, 2005.

[44] P. Wellman. *Tactile Imaging*. PhD thesis, Cambridge, MA: Harvard University's Division of Engineering and Applied Sciences, 1999.